SURFACE COAL FIRE DETECTION USING VIIRS AND LANDSAT 8 OLI DATA

RAKTIM GHOSH

March, 2019

SUPERVISORS:

Mr. Prasun Kumar Gupta
Dr. Valentyn Tolpekin
Dr. S. K. Srivastav

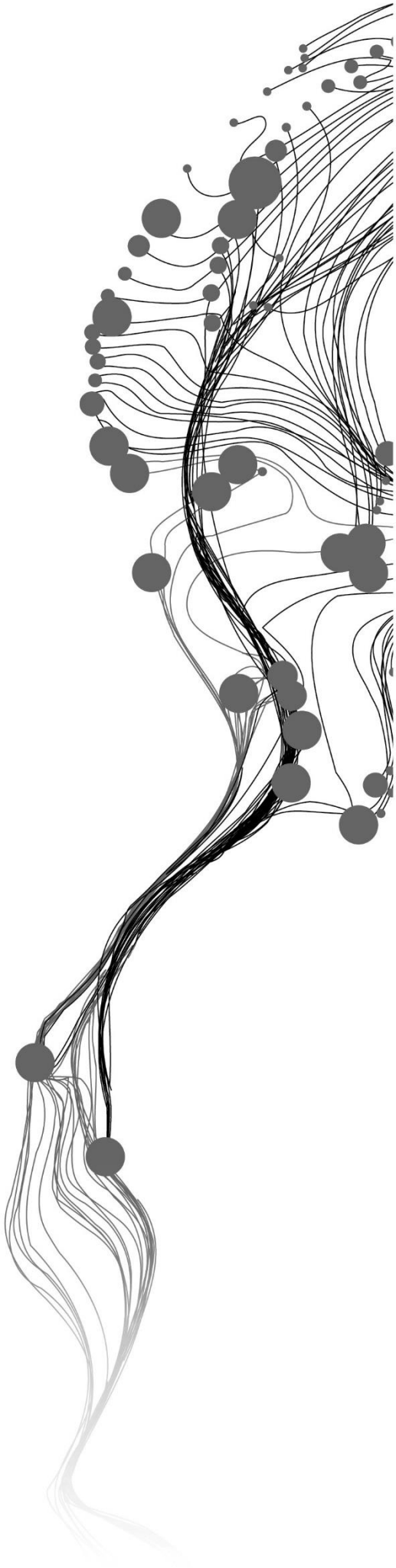

SURFACE COAL FIRE DETECTION USING VIIRS AND LANDSAT 8 OLI DATA

RAKTIM GHOSH
Enschede, The Netherlands, March, 2019

Thesis submitted to the Faculty of Geo-Information Science and Earth Observation of the University of Twente in partial fulfilment of the requirements for the degree of Master of Science in Geo-information Science and Earth Observation.
Specialization: Geoinformatics

SUPERVISORS:
Mr. Prasun Kumar Gupta
Dr. Valentyn Tolpekin
Dr. S. K. Srivastav

THESIS ASSESSMENT BOARD:
Prof. Dr. Ir. A. Stein (Chair, ITC Professor)
Dr. R. D. Garg (External Examiner, IIT Roorkee)

ABSTRACT

Coal fire has been a major concern for the coal industries, environmental departments, and other national agencies in India. The vulnerability associated with the coal fire is inextricably linked with environmental impacts. Systematic monitoring is of paramount importance concerning the impacts of habitats living within the close proximity of the coal fire-affected regions. Remote sensing provides a cost-effective solution in detecting and monitoring the coal fire-affected areas. In this study, the potential of channel-specific surface reflectance of Landsat-8 OLI and VIIRS data have been explored in detecting and delineating the regions affected by surface coal fires. The core objective of this research is to formulate a methodology by blending Landsat-8 and VIIRS data with a view to generating a high-resolution and high-frequency synthetic coal fire products.

The Jharia coalfield, India has been chosen as a study area for the current research. It is majorly affected by surface and sub-surface coal fires in India and a significant amount of potential coal resources have been depleted. In detecting the coal fire, the reflectance-based active fire detection method was incorporated to check its fidelity in delineating surface coal fire affected pixels. After observing the underestimation caused by the existing active fire detection method, a normalised reflectance-based active fire detection method was established and the fidelity of this algorithm was tested for other actual Landsat scenes over the similar region in Jharia coalfield. On the other hand, in view of generating the high-frequency and high-resolution synthetic coal fire products, the current study explored several spatiotemporal fusion methods within the framework of weight function based techniques to blend the high spatial resolution Landsat-8 data with the high temporal resolution VIIRS data within the similar spectral domains broadly matches with each other. The fire responsive spectral channels lying within the domain of NIR and SWIR regions were employed for spatiotemporal fusion methods. Consequently, the methods named STARFM and ESTARFM were explicitly implemented in this research.

The performance of these spatiotemporal fusion methods was evaluated qualitatively and quantitatively using several assessment metrics. With a view to improving the accuracies further, the modified STARFM and the modified ESTARFM methods were established. In order to generate a high-resolution and high-frequency synthetic coal fire products, this study executed a novel reflectance-based active fire detection method on synthetically predicted Landsat like images derived from the spatiotemporal fusion methods. Also, the accuracy assessments of the synthetic coal fire products were carried out by assessment metrics linked with the corresponding confusion matrix. Moreover, a coal fire product quality index (CFPQI) was designed to designate the overall quality of the synthetic product. It was observed that the modified ESTARFM outperformed all other fusion in terms of spatiotemporal fusion methods as well as for the synthetic coal fire products generated from it.

In light of the above discussions, this study built an overall framework for generating the high-frequency and high-resolution synthetic coal fire products which could be used for systematic mapping and monitoring of the regions affected by surface coal fire. Interestingly, the established novel coal fire detection method was successful in resolving the underestimation caused by the existing active fire detection method. In future studies, the fidelity of the novel coal fire detection techniques could be tested for other coal fire-affected regions such as in China, Australia and the USA. Also, a fusion-based neural network could be designed for locating the fire pixels more accurately in the synthetic images.

Keywords: Coal Fire, OLI, Spatiotemporal Fusion, VIIRS, STARFM, ESTARFM

ACKNOWLEDGEMENTS

I have taken efforts in completing this research work but, it would not have been possible without the invaluable moral support and inspiration of my parents, whom I would like to extend my heartfelt gratitude for rendering a helping hand throughout and prayers for initiating in organizing every activity of my thesis.

I am also sincerely thankful to my supervisors from IIRS and ITC, Mr. Prasun Kumar Gupta, Dr. Valentyn Tolpekin and Dr. S. K. Srivastav for their patient guidance, support, constant supervision and providing potent and intriguing insights during the complete duration of this research work in providing me with necessary information and materials regarding my work. My sincere gratitude towards the M.Sc. Course Co-ordinator and Head of the Department Geo-informatics Division of IIRS, Dr. Sameer Saran for his forbearing help and support.

Thanking everyone by their names will not be possible, but every person I came across were very helpful and supportive throughout my journey of this research.

Finally, I would like to acknowledge the open source community for developing software, libraries and providing datasets.

Raktim Ghosh

ABBREVIATION USED

AAD	Absolute Average Difference
AFD	Active Fire Detection
ASTER	Advanced Spaceborne Thermal Emission and Reflection Radiometer
BME	Bayesian Maximum Entropy
CC	Correlation Coefficient
CFPQI	Coal Fire Product Quality Index
EDRs	Environmental Data Records
ERGAS	The ErreurRelative Globale Adimensionnelle de Synthèse
ESTARFM	Enhanced Spatiotemporal Adaptive Reflectance Fusion Method
ETM	Enhanced Thematic Mapper
FDR	False Discovery Rate
FN	False Negative
FP	False Positive
FSDAF	Flexible Spatio-temporal Data Fusion
GOES	Geostationary Operational Environmental Satellite system
HJ-1	Huan Jing-1
I	Imagery Resolution Band (used for VIIRS)
LST	Land Surface Temperature
M	Moderate Resolution Band (used for VIIRS)
MCC	Matthews Correlation Coefficient
MERIS	Medium Resolution Imaging Spectrometer
MODIS	Moderate Resolution Imaging Spectroradiometer
MMT	Multi-sensor Multi-resolution Technique
MWIR	Mid-wave Infrared
NDVI	Normalised Difference Vegetation Index
NIR	Near Infrared
NRAFD	Normalised Reflectance-based Active Fire Detection
OLI	Operational Land Imager
PPV	Predictive Positive Value
PSF	Point Spread Function
RMSE	Root Mean Square Error
SPSTFM	Sparse Representation-based Spatiotemporal Fusion Model
STARFM	Spatiotemporal Adaptive Reflectance Fusion Method
STDFA	Spatial Temporal Data Fusion Approach
STRUM	Spatial Temporal Reflectance Unmixing Method
SWIR	Short-wave Infrared
TIR	Thermal Infrared
TIRS	Thermal Infrared Remote Sensing
TN	True Negative
TP	True Positive
TPR	Total Positive Rate
VIIRS	Visible Infrared Imaging Radiometer Suite

TABLE OF CONTENTS

LIST OF FIGURES

LIST OF TABLES

1. INTRODUCTION

1.1. Motivation

"A coal fire is defined as combustion of coal in a coal seam (or a pile of stored or waste coal), which has a potential to burn for a long time by spreading along both directions of the strike and dip of the coal seam" (Kuenzer, 2004). Coal fire can be broadly categorized as surface and sub-surface fire (Gangopadhyaya, 2003). The surface fires are commonly found in spoil stack of overburden as well as in opencast mining region. However, the subsurface fires are appeared due to the penetration of oxygen via mining induced cracks or fissures towards underground mining areas. Generally, coal fires are caused by an exothermic reaction of carbon content with the adsorption of oxygen at the exposed surface (Kuenzer, Zhang, Tetzlaff, et al., 2007). If the temperature of coal reaches a threshold value (between 80ºC to 120ºC), the obnoxious gaseous products (e.g., NO, SO_2, CO, CH_4) are emitted (Chatterjee, 2006). Furthermore, the temperature will continue to increase to reach a state of ignition temperature (between 230ºC to 280ºC), thereby resulting in the burning of coal (Huo et al., 2014). Moreover, the spontaneous, active fire starts propagating from the source of ignition towards subsequent fire-prone zone under the influence of wind, rainfall, topography, geological phenomena (faults, folds, dikes). Consequently, coal fire triggers operational constraints which eventually leads to the hindrance of efficient production in the mining environment. Therefore, systematic monitoring of coal fire is essential to predict the probable directional propagation of active fires accurately. As the in-situ measurement is time-consuming and incurs a significant cost, the application of remote sensing methods is a powerful tool for assessing as well as predicting the unknown coal fire regions (Kuenzer, 2004).

The vulnerability associated with the active fire-affected areas is intricately related to dangerous consequences of environmental degradation in various countries across the globe such as China, India, and Australia (Kuenzer, Zhang, Tetzlaff, et al., 2007). Consequently, coal fire depletes a large amount of prospective geologic reserve and the stability of environmental dynamics is deteriorated rapidly during the exploration as well as production phase of mining. Furthermore, it affects the environment by releasing gasses, fumes, as well as igniting grassland, brush, small trees and other topographic features which are prone to fire and as a consequence, the local ambient atmospheric temperature increases. Moreover, the process of land subsidence due to fire-affected areas collapse the surface infrastructures such as buildings, railroads, high-tension electric poles (Zhou, Zhang, Wang, Huang, & Pan, 2013). In essence, the active coal fire causes unprecedented surface subsidence where the massive amount of agricultural lands get affected which in turn is leading to production loss for the agricultural industries. Therefore, the existing surface, as well as sub-surface coal fire, is dynamically altering techno-economic factors that are inextricably linked with site-specific mining applications (Huo et al., 2014). Systematic mapping and monitoring of mining-induced fires are extremely helpful for quantifying the economic and environmental loss.

A significant amount of research activities have been carried out with the help of numerous thermal infrared (TIR) data acquired by spaceborne, an airborne and ground-based instrument specifically in the field of active coal fire mapping and monitoring applications (Kuenzer & Dech, 2013). Interestingly, Visible Infrared Imaging Radiometer Suite (VIIRS) has gained a lot of popularity over the last few years due to its contribution towards primary remote sensing related applications in the domain of biomass burning, active fire identification (Bennett & Smith, 2017; Kanniah et al., 2016; Schroeder, Oliva, Giglio,

& Csiszar, 2014). On the other hand, Landsat series satellites have been extensively used for coal fire related applications over the last few decades (Raju, Gupta, & Prakash, 2013). There are various active fire mapping algorithms which were built upon VIIRS (Elvidge, Zhizhin, Hsu, & Baugh, 2013; Schroeder et al., 2014) and Landsat (Chatterjee, 2006; Roy, Guha, & Kumar, 2015; Schroeder et al., 2016) data, considerably used for distinguishing fire affected pixels from other ground sources. However, the possibility of blending the data derived from the sensors mentioned above will be advantageous for generating high resolution and high-frequency synthetic coal fire product.

Recently, VIIRS data has been profoundly used for detecting active fire due to its ability to capture radiances from the ground sources more accurately in respect of its predecessors (Vadrevu & Lasko, 2018). The VIIRS sensor which is mounted on the Suomi-NPP satellite and placed in a sun-synchronous orbit acquires co-registered data with a spatial resolution of 375 m and 750 m (Oliva & Schroeder, 2015). Earlier, two operational products were being generated using new VIIRS data for meteorological applications: the key Environmental Data Records (EDRs) and the Application-Related Products (Justice et al., 2013). Additionally, a new active night fire detection algorithm was also designed to characterise hot sources using short-wave infrared (SWIR), near-infrared (NIR) and mid-wave infrared (MWIR) channels, of which elementary detection band (M10) was located at SWIR region between 1.571 μm to 1.631 μm (Elvidge et al., 2013). After all, the significant advantage of VIIRS is that it has drastically removed the errors appeared earlier from pixel-saturation, blooming as well as the dearth of in-flight calibration (Bennett & Smith, 2017). However, due to the low spatial resolution of VIIRS, the hot sources with smaller areas often get misidentified.

Even though there is a significant remark of VIIRS in recent days, several research activities have also been performed by incorporating principles of thermal remote sensing on Landsat series satellite data for detecting active fire over the last few decades (Syed, Riyas, & Kuenzer, 2018). The Landsat-8 sensor, augmented with Operational Land Imager (OLI) and the Thermal Infrared Sensor (TIRS), was built by a joint collaboration of NASA-USGS team (Roy et al., 2014), flown in a sun-synchronous orbit with a spatial resolution of 30 m (Irons, Dwyer, & Barsi, 2012). Previous studies built an active fire detection algorithm which was designed as well as implemented on Landsat 7 ETM+ and ASTER data (Giglio et al., 2008; Schroeder et al., 2008). In addition to previous work, an algorithm was developed on Landsat-8 / OLI data, of which the primary detection band (l7) was located at SWIR region between 2.11 μm to 2.29 μm (Schroeder et al., 2016). However, simultaneous pixel saturation, folding of DN values have been significant disadvantages of active fire detection algorithms built over Landsat-8 data.

The principles of thermal remote sensing have been widely used in the domain of active as well as passive fire monitoring applications (Kuenzer & Dech, 2013). The rate of exponential increment of voluminous satellite-derived remote sensing images of distinct characteristics including multi-temporal, multi-spectral, multi-polarization and multiresolution, has led the foundation of integrating different images to improve pre-existing information (Dong, Zhuang, Huang, & Fu, 2009). Therefore, the concept of image fusion is relevant to harmonize various spatial, spectral and temporal resolution images captured by distinct satellite/airborne sensors to generate composite images mostly applicable for change detection and monitoring related applications. The existing image fusion techniques can be broadly categorised as spatiotemporal, spatio-spectral and multi-sensor image fusion in the domain of remote sensing (Meng, Shen, Zhang, Yuan, & Li, 2015). The application of spatiotemporal image fusion technique plays a pivotal role in generating high resolution, high-frequency synthetic image product which is considerably helpful for producing images with high information content. Therefore, the dangerous consequences of coal fire can easily be mitigated with the help of systematic mapping and monitoring using spatiotemporal image fusion techniques that can be applied over the spaceborne sensors having complementary features.

In light of the above discussions, generating a high-frequency coal fire image product will be convenient for coal industries. There are several existing spatiotemporal image fusion algorithms predominantly used for miscellaneous remote sensing applications (Gao, Masek, Schwaller, & Hall, 2006; Hazaymeh & Hassan, 2015; Huang & Song, 2012; W. Zhang et al., 2013; Zhu, Chen, Gao, Chen, & Masek, 2010). Consequently, the quality assessment of a fused product plays a crucial role in remote sensing (Pohl & Van Genderen, 1998). Therefore, the propagation of uncertainty associated with the image fusion algorithms can be assessed to minimize the errors linked upon the synthetic end product. Furthermore, the spatial, temporal and spectral uncertainty of complementary inputs has to be explored to critically design a weight function to implement by incorporating distinct characteristics (spatial resolution, temporal resolution, and spectral resolution) of each data derived from each sensor. Also, the orbital parameters, as well as the spectral response function associated with coal fire for both sensors, are different from each other. Collectively, there are various advantages and disadvantages associated with VIIRS and Landsat 8 OLI / TIRS data concerning different fire detection algorithms. Since both datasets provide complementary features concerning spatial and temporal resolutions, it is possible to formulate a methodology by blending these datasets, wherein, a high-frequency and high-resolution resolution synthetic Landsat images can be generated. Moreover, the synthetic coal fire affected pixel can be retrieved by designing criteria using the spectral characteristics of fire affected pixels derived from each image. Consequently, the end product will benefit the mining industry in respect of coal fire mapping and monitoring applications, and also the health & safety departments can use these products to assess the risk associated with fire propagation. Furthermore, the end product can be used for the environmental impact assessment of a specific mining area over a definite period by the departments entrusted with the environmental studies.

1.2. Problem Statement

Coal fire detection is based on the prevalence of at-sensor spectral radiance having a dominant emissive component within the spectral range of SWIR and TIR. Most of the sensors such as Landsat, VIIRS captures emitted radiation more effectively at night time. Hence, the availability of a night-time scene is reliable for estimating the radiant temperature of the earth surface. However, during the daytime, due to the mixing of reflected solar radiation with the emitted radiation, it is challenging to estimate accurate radiant temperature. The alternative way of distinguishing fire affected pixels is to introduce the concept of channel-specific spectral reflectance values of Landsat 8 OLI sensor as an input. Furthermore, generating a high-frequency and high-resolution synthetic coal fire product is reliable in detecting the sudden propagation of coal fire, thereby accurate monitoring can be performed. According to the author's knowledge, both Landsat 8 OLI and VIIRS sensor have not been fused yet in the domain of coal fire related applications.

Therefore, this study will attempt to apply various conventional as well as recent coal fire detection techniques to detect and distinguish active-fire affected pixels from its background. After successfully exploring various algorithms, this study will further explore the different spectral channels to construct a framework for spatial-spectral-temporal fusion technique by blending Landsat-8 OLI / TIRS and VIIRS dataset to generate high-resolution and high-frequency coal fire product.

1.3. Research Identification

The overall focus of this research is to detect the surface coal fire by using VIIRS and Landsat 8 / OLI data, thereby to fuse the aforementioned dataset to generate a high frequency and high-resolution data product.

1.4. Research Objectives

The primary objective of this research is to investigate the multi-spectral information for the identification of coal fire from day-time VIIRS and Landsat 8 / OLI data to formulate a methodology for spatial-spectral-temporal fusion by merging aforementioned data to generate high resolution and high-frequency data product. The overall objectives can be classified into three specific objectives. They are,

1) Review and study contextual features, active fire identification method to detect fire-affected pixels.
2) To explore and construct the spatial-spectral-temporal data fusion techniques in the context of coal fire related applications.
3) To construct a novel method for detecting the coal fire pixels from the synthetic Landsat like images and its fidelity in the actual Landsat data.

1.4.1. Research Questions

According to the specific research objectives, the following research questions can be addressed.

1. Specific objective 1:
   a. Which contextual and spectral features derived from the datasets have been used in the identification of sub-pixel hot sources?
   b. Which thresholding techniques and classification methods have been used to detect and characterise sub-pixel hot sources?
   c. What kind of limitations are imposed on coal fire detection using Landsat 8 / OLI and VIIRS data due to sensor characteristics and environmental conditions?
2. Specific objective 2:
   a. Which processing levels have been used so far to construct spatiotemporal fusion in reference to coal fire related applications?
   b. What kind of preprocessing technique is performed prior to the data blending keeping in view of spectral, temporal and spatial bias?
   c. Based on what parameters, the value of combined weights and conversion coefficients can be computed dynamically to predict the radiance image accurately?
3. Specific objective 3:
   a. Which spectral features are to be used to generate criteria for extracting coal fire pixels from the synthetic image?
   b. How to design the criteria in view of its viability for retrieving the fire-affected pixels from the actual as well as the synthetic Landsat images?
   c. What thresholding techniques can be used?

1.5. Innovation

The study attempts to construct a spatiotemporal fusion framework using VIIRS and Landsat 8 OLI data to generate a high-resolution and high-frequency product in order to detect and delineate the coal fire related thermal anomalies. The study proposes to formulate a methodology for detecting coal fire from synthetic images which will be generated using the spatiotemporal fusion methods.

1.6. Research Workflow

A Generalized workflow of the research has been depicted in Figure 1.1.

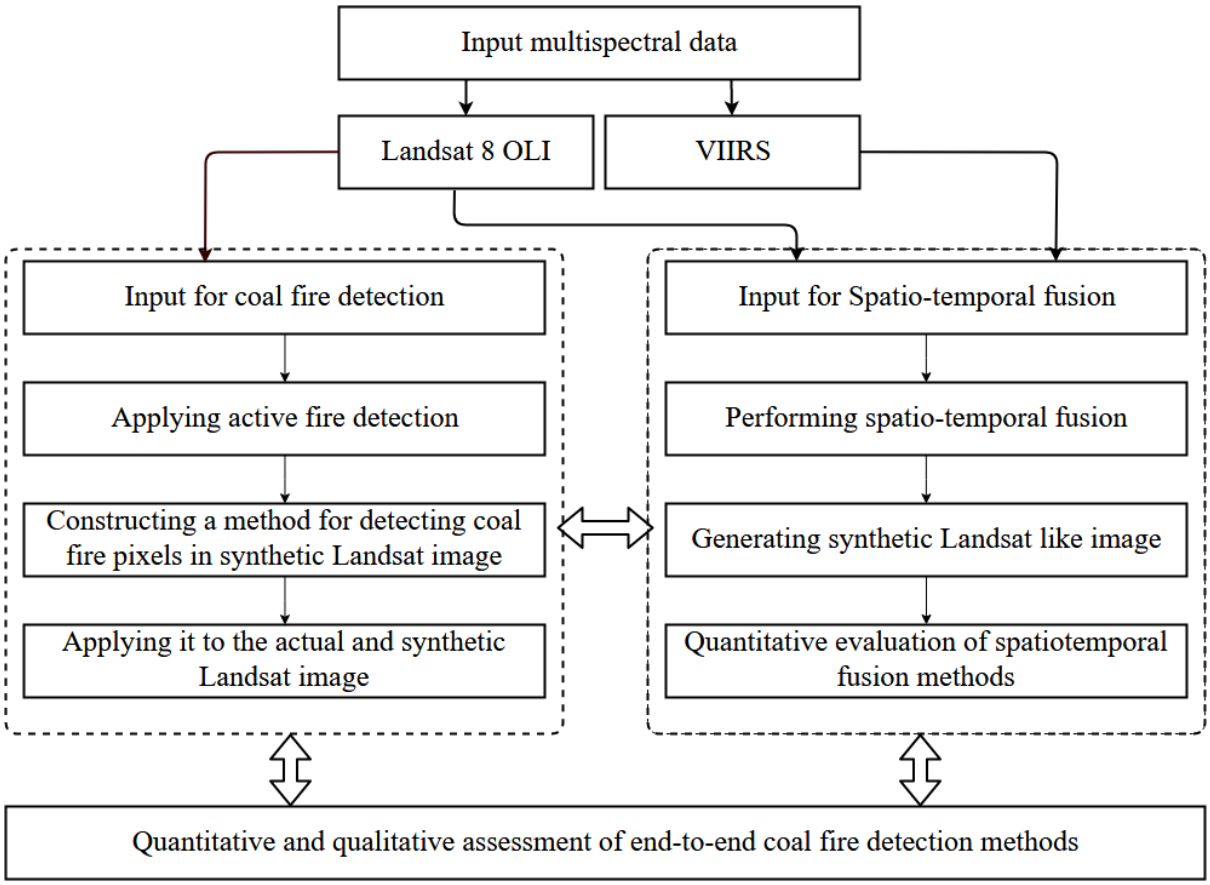

Figure 1.1. Generalized methodology

1.7. Thesis Outline

The entire thesis has been organized into seven chapters. **Chapter 1** describes some basic concepts of the topic, research identifications, corresponding research objectives and associated research questions along with the depiction of the schematic workflow of this research. **Chapter 2** elucidates the basic principles of thermal and shortwave infrared remote sensing and its applications for coal fire detection techniques as well as the miscellaneous domain of spatiotemporal fusion methods. **Chapter 3** introduces the methods adopted for spatiotemporal fusion approaches. **Chapter 4** describes the chosen study area, datasets and software used for this research. **Chapter 5** highlights the results obtained. **Chapter 6** describes the critical interpretations of the results. **Chapter 7** concludes the research with an answer to the research objectives and the associated future scope of this study.

2. THEORY AND LITERATURE REVIEW

This chapter highlights the brief review of coal fire detection methods using satellite remote sensing. **Section 2.1** elucidates the coal fire detection methods and the importance of thermal remote sensing in delineating coal fire regions. **Section 2.2** depicts the miscellaneous applications of Landsat series satellite data in detecting and delineating coal fires. **Section 2.3** elucidates the several spatiotemporal fusion approaches in generating high-resolution and high-frequency synthetic images largely applicable for change detection and monitoring related applications.

2.1. Coal fire detection using satellite remote sensing

The satellite remote sensing is largely used for coal fire detection and monitoring applications. The domain of thermal and shortwave infrared remote sensing plays a pivotal role in detecting and monitoring coal fire regions. In the next section, the underlying theoretical basis of these remote sensing approaches is elucidated.

2.1.1. Importance of thermal infrared remote sensing

The application of thermal infrared remote sensing (TIRS) plays a significant role in detecting coal fire related thermal anomalies (Kuenzer & Dech, 2013). TIRS remote sensing explicitly uses the atmospheric window ranges from 3 μm to 5 μm and 8 μm to 14 μm because of insignificant atmospheric interaction. Therefore, the emitted electromagnetic radiation is captured by the thermal sensors which in turn, is effective in identifying hotspots or high-temperature objects or sub-pixels hot sources. The spectral radiant intensity of an object is regulated by Planck's radiation equation. Therefore, it is possible to retrieve the kinetic temperature of an object or a pixel in an image (in remote sensing), and those thermally anomalous pixels or objects can be distinguished from its surroundings. This chapter has depicted some of the underlying theoretical principles of thermal physics.

2.1.2. Theoretical basis of thermal remote sensing

2.1.2.1. Planck's Law

Planck's law describes the density of electromagnetic spectral radiance emitted by a Black Body at a specific temperature and frequency can be defined (Boya, 1900) as follows in Eq. (2.1):

$$L_\lambda = \frac{2hc^2\lambda^{-5}}{e^{hc/\lambda kT_{rad}} - 1} \tag{2.1}$$

Where,

L_λ Spectral radiance ($W\ m^{-2}\ sr^{-1}\ \mu m^{-1}$)
λ Wavelength (m)
T_{rad} Radiant temperature of the object (K)
h Planck's constant = 6.26×10^{-34} $J\ s$
c Speed of Light = 3×10^{8} m/s
k Boltzmann constant = 1.381×10^{-23} J/K

In reference to thermal remote sensing, after retrieving at-sensor spectral radiance from raw digital data, the kinetic temperature of an object can be estimated as described in Section 2.1.2.4.

2.1.2.2. Stefan's Boltzmann Law

The total amount of radiant flux (M_λ) emitted per unit surface area of a blackbody is strictly proportional to the fourth power of the temperature (T) on which it is emitting per unit time over the entire spectral range:

$$M_\lambda = \sigma \times T^4 \tag{2.2}$$

Where σ is the Stefan-Boltzmann constant with a value of $5.67 \times 10^{-8}\ W\ m^{-2}\ K^{-4}$

No material on Earth surface is a perfect emitter. Therefore, the emissivity of real material is always less than 1. The emissivity of a particular object depends on the wavelength at which it radiates.

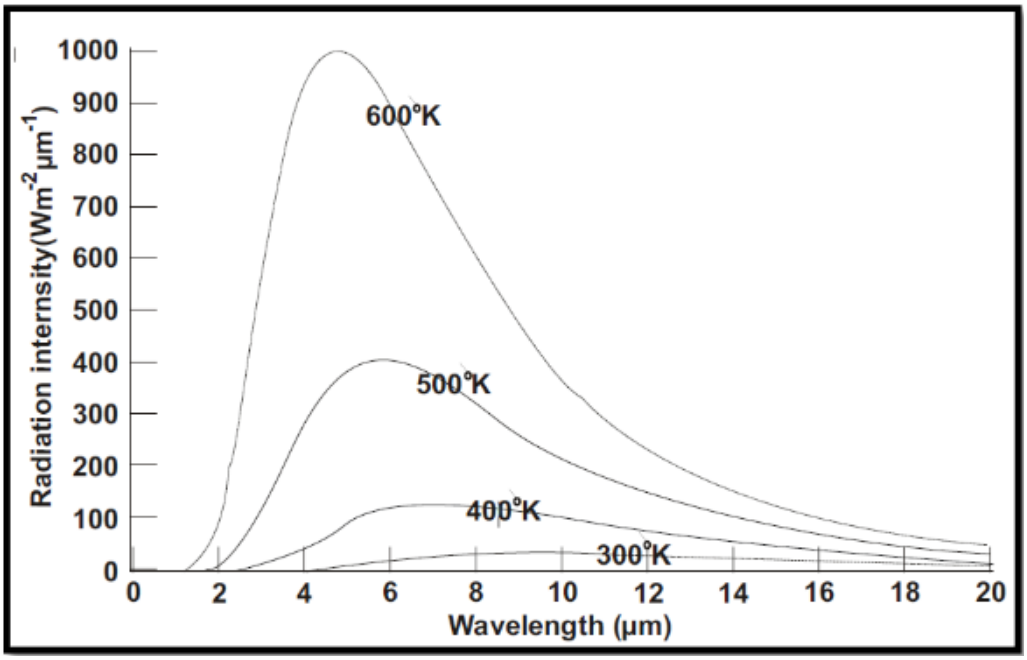

Figure 2.1. The relationship between radiant intensity and wavelength (Voigt, Tetzlaff, Zhang, & Ku, 2004)

2.1.2.3. Peak radiant emission and Wien's displacement law

The radiant energy of an object is a function of wavelength at a constant kinetic temperature. The kinetic temperature at which an object emits the highest radiant flux is termed as peak radiant emissive wavelength (λ_{max}). With the increasing temperature, the total amount of radiant energy increases, and the wavelength at which peak radiant emission occurs is shifted towards shorter wavelength (Figure 2.1). This phenomenon is attributed as Wien's displacement law (Feynman, Leighton, & Sands, 1989):

$$\lambda_{max} = \frac{2897}{T_{rad}} \tag{2.3}$$

Where T_{rad} is the radiant temperature at K, and 2897 is a constant with unit $\mu m\ K$. Therefore, the object with higher radiant intensity can be detected using SWIR spectral channel of thermal sensors.

2.1.2.4. Kinetic temperature, radiant flux and heat transfer

Every material with a temperature higher than -273.73 ºC emits electromagnetic radiation. The kinetic heat is emitted due to the energy released during the random motion of particles within a matter. Consequently, the collision which is triggered by the Brownian motion is responsible for the change of energy state and the resulting electromagnetic radiation is emitted from the surface of the material. Therefore, the kinetic and/or internal as well as heat energy is then converted to radiant energy.

The kinetic temperature of an object is the measure of the total concentrated heat of the surface material. It is measured by putting a thermometer in contact with the object. On the other hand, the radiant flux is the measure of the emitted electromagnetic radiation from an object. Therefore, the radiant temperature is quantified by estimating the total concentrated radiant energy of an object. Also, the kinetic temperature is always greater than the radiant temperature as the ratio of the amount of electromagnetic radiation emitted by a real object to a black body is always less than 1. The radiant temperature can be computed using Eq. (2.2):

$$T_{rad} = \frac{\frac{hc}{k}}{\lambda \times \ln\left[\frac{2hc^2\lambda^{-5}}{L_\lambda} + 1\right]} \tag{2.4}$$

In the Eq. (2.4), the central value of the wavelength of a specific spectral channel of the thermal sensor is considered for estimating radiant temperature. After computing the spectral radiance using a band-specific calibration coefficient, the pixel-integrated radiant temperature can be calculated using the above Eq. (2.4). Furthermore, after estimating the spectral emissivity (ε_λ), the kinetic temperature can be obtained using the following mathematical relation (Huo et al., 2015):

$$T_{kin} = \frac{T_{rad}}{\varepsilon^{0.25}} \tag{2.5}$$

Where ε denotes the emissivity of the material in Eq. (2.5). The aforementioned kinetic temperature in Eq. (2.5), can be used to identify hot sources or coal fires in the mining region. In essence, the satellite sensors which are augmented with the thermal spectral channel has been effectively used to detect and characterize thermally anomalous pixels (Syed et al., 2018).

2.1.2.5. Spectral emissivity

The emissivity of surface material can be determined by the ratio of the amount of electromagnetic radiation emitted at a given temperature with the amount of theoretical electromagnetic radiation emitted by a blackbody with the same temperature and wavelength:

$$\varepsilon_\lambda = \frac{L(\lambda, T)}{L^o(\lambda, T)} \tag{2.6}$$

Where $L(\lambda, T)$ is the spectral radiance of material at wavelength λ and temperature T, $L^o(\lambda, T)$ denotes the spectral radiance of a blackbody at a similar wavelength and temperature. An emissivity of a material is an intrinsic property and independent of irradiance.

In reference to thermal remote sensing, the kinetic temperature of an object is obtained with known T_{rad} and ε. The spectral emissivity of the earth surface is governed by several factors. The higher amount of

water content generally results in higher emissivity due to the absorption properties within the IR region. Therefore, the thermal emissivity of water generally ranges from 0.97 to 1.0. With increasing vegetation cover, the thermal emissivity of a surface material increases (Jin & Liang, 2006). An empirical relationship was established between emissivity and Normalised Difference Vegetation Index (NDVI) for different surface cover (Van De Griend & Owe, 1993):

$$\varepsilon_\lambda = a + b \times \ln(NDVI) \tag{2.7}$$

The a and b in Eq. (2.7), are two constants with a = 1.0094 and b = 0.047 with a correlation coefficient of 0.941 for ε_λ and NDVI (0.01 level of significance). In reference to thermal remote sensing, while generating the pixel-integrated temperature map for the datasets derived from the TIR channel, the above empirical relationship is applicable for those pixels where the NDVI is greater than zero. Furthermore, the reflectance of water-logged areas within the visible range is significantly higher than the NIR range, often leading to negative NDVI. Therefore, the Eq. (2.7), is invalid for those pixels. Moreover, in case of the rock surfaces and bare soil, the reflectance value is quite similar within the spectral range of red and NIR, thereby resulting in the value of NDVI closer to zero. As the fire-affected pixels in the mining region generally devoid of vegetation, the emissivity of sandstone, rock and loosely bare soils can be kept as 0.92 (Buettner & Kern, 1965).

2.2. Applications of Landsat series satellite sensors in detecting coal fire

The Landsat derived satellite data have been used for several decades in coal fire mapping and monitoring applications (Chatterjee, 2006; Cracknell & Mansor, 1993; Kuenzer et al., 2007; Mansor et al., 1994; Oppenheimer et al., 1993). The thermal channel, as well as SWIR channel, is generally used for detecting surface and sub-surface coal fire. In case of the thermal channel, the satellite captures the emitted radiance and the signal which is captured within a spectral range of SWIR is composed of both emitted and/or reflected radiance from earth surface. Using the concept of kinetic temperature, the coal fire affected pixels are distinguished from other background pixels.

2.2.1. Importance of thermal infrared (TIR) channel

From the year 1990 to 1997, the potential of TIR channel of Landsat TM was heavily explored to detect coal fire related thermal anomalies (Bhattacharya, Reddy, & Mukherjee, 1991; Cracknell & Mansor, 1993; Mansor et al., 1994; Prakash, Saraf, & Gupta, 1995; Van Genderen, & Cassells, 1996).

The density slicing method was prevalent to characterise the thermal anomalies by incorporating the rigorous trial-and-error method and observing the statistical variations with slopes derived from the field data (Guha, Kumar, & Kamaraju, 2008; Prakash & Gupta, 1998). The daytime band 6 of Landsat TM, was primarily used for retrieving temperature threshold, however, due to reflected solar heating, sometimes the at-sensor radiant temperature was not representative of proper ground temperature, and as a result, the nighttime TM data were used to distinguish fire affected pixels from the background. The thermal anomaly of Jharia Coalfield, India was first detected using density slicing method incorporated on Landsat TM and a temperature threshold was set to 40º C (Cracknell & Mansor, 1993; Mansor et al., 1994). The three steps were used to retrieve kinetic temperature from the raw digital data. At first, the raw digital data was converted to spectral radiance, and in the second step, using Planck's radiation equation, the radiant temperature was calculated. Lastly, using the value of thermal emissivity, the kinetic pixel-integrated temperature map was generated. Therefore, to distinguish the coal fire affected pixels, the thresholding method was adopted to generate a coal-fire map. However, Prakash et al. (1995) carried out a thresholding method based on band-specific DN value to delineate fire-affected pixels from the background. Guha et

al. (2008) carried out a density slicing method over the Jharia coalfield to distinguish the coal-fire affected pixels for quantifying the coal fire affected areas using nighttime TIR channel of Advanced Spaceborne Thermal Emission and Reflected Radiometer (ASTER).

Apart from density slicing, several complex methods were adopted to delineate the surface and sub-surface coal fires from its surroundings (Chatterjee, 2006; Kuenzer, Zhang, Li, et al., 2007). The field-based modelling was carried out by Chatterjee (2006), to explicitly distinguish the surface fire mixed pixels by assuming a typical 50 % of the mixed pixel got affected by the fire. Kuenzer et al. (2007) developed a rigorous moving window based approach (varying sizes from 11 × 11 to 35 × 35) to effectively select the local temperature thresholds by critically analysing the local histograms derived from those windows. However, the method was computationally intensive.

2.2.2. Importance of short-wave infrared channel

During 1990, the potential of SWIR band was explored to detect and delineate the coal fire affected areas due to its ability of capturing both emitted and reflected signals from a hotspot or fire-affected pixels (Andres & Rose, 1995; Dozier, 1981; Francis & De Silva, 1989; Oppenheimer, Rothery, Fieri, Abrams, & Carrere, 1993; Prakash, Gupta, & Saraf, 1997; Reddy, Srivastav, & Bhattacharya, 1993; Rothery, Francis, & Wood, 1988). The Landsat TM was equipped with two SWIR channel: band 7 (centered at 2.215 μm) and band 5 (centered at 1.65 μm). According to the Planck's radiation equation, the peak radiant emission is shifted towards the SWIR region as the temperature of a material increases. Therefore, the emitted component of a hot-source is captured more efficiently within the spectral range of the SWIR region. The pixel-integrated kinetic temperature was calculated using the dual-channel-based temperature retrieval method by incorporating the band 5 and band 7 (Oppenheimer et al., 1993). Furthermore, the temperature and area of a typical sub-pixel hot source were retrieved using the dual-channel (band 7 and band 5 of Landsat TM) based approach (Dozier, 1981).

In order to correct the captured radiance at SWIR region which is composed of both emitted and reflected signals (solar radiance), the neighbourhood pixels can be considered to subtract the combined DN value from the actual DN value of hotspot with an extended assumption of absence of emitted radiation from the neighbourhood. Chatterjee (2006) investigated the saturation of TIR channel at 70 ºC, and hence the SWIR channel was considered to delineate the surface and sub-surface areas where the temperature sensitivity of channel 7 of Landsat TM was 160 ºC to 277 ºC broadly matches with the actual coal fire temperature (150 ºC to 250 ºC) of Jharia coalfield. However, the method is restricted to the assumption of the presence of a reflected solar component, spectral emissivity and the absence of emitted component along with the availability of two SWIR channel in a sensor.

2.2.3. Recent work

Recently, several research activities have been carried out to detect active fire affected pixels using reflectance and radiance value as an input. Schroeder et al. (2016) have developed a completely new active fire detection algorithm using the concept of bi-channel based fixed thresholding technique which was established upon a previously built ASTER and Landsat-7 / ETM+ (Giglio et al., 2008), by taking into consideration of visible as well as near-infrared bands. However, simultaneously ambiguous pixel saturation over the channel 7 centered at SWIR region as well as spurious DN folding, has been identified as a major constraint. Furthermore, the accurate retrieval of temperature and area of sub-pixel hot sources with an assumption of homogeneous temperature, have been developed using band 7 (centered at SWIR region) of Landsat 8 / OLI data recently (Kato, Kouyama, Nakamura, Matsunaga, & Fukuhara, 2018). The study has shown the potential of Landsat 8 / OLI data over MODIS and VIIRS, in case of detecting small hotspots. However, the aforementioned study has a crucial limitation (assumption of a singular

component of sub-pixel hot sources) while the multiple heat sources (heterogeneous temperature) come into the picture. Roy et al. (2015) have depicted a cluster-based separated max-min radiant temperature approach to distinguish coal fires from the background, using unbiasedly scattered homogeneous blocks of pixels from ASTER (band 13, block (9×9)) and Landsat-8 (band 8, block (27×27)) data. Interestingly, the detection of the surface, as well as sub-surface fire during the summer season, has various challenges due to ambiguousness arises between coal-fire pixels and the water bodies in reference to Land Surface Temperature (LST) (Mukherjee, Mukherjee, & Chakravarty, 2018). However, the novelty of the proposed method relies on the detection as well as separation of water bodies from other objects prior to analysing fire-affected pixels on the image.

2.2.4. Active fire detection algorithm using Landsat 8 OLI

Schroeder et al. (2016) developed an algorithm based on dual-channel based fixed-threshold integrated with the contextual approach to extract the potentially unambiguous active fire affected pixels by exploiting the differential spectral response of SWIR and NIR channel of Landsat 8 OLI data. The algorithm was previously developed for Landsat 7 ETM+ as well as ASTER (Giglio et al., 2008). Consequently, the active fire detection (AFD) algorithm which was primarily built on utilizing the channel 7 of Landsat 8 OLI sensor, can be split into two modules: (i) daytime and (ii) nighttime detection.

2.2.4.1. Daytime detection

The daytime detection consists of constructive conditional tests by incorporating the OLI channels as an input function. During the daytime, it has been observed that the SWIR channel (2.2 μm) captures the emitted as well as reflected signals from the hot sources. In order to exclude the effect of reflected component (daytime solar radiation) in channel 7 (2.2 μm), the channel 5 (0.865 μm) is considered which is usually insensitive to the emitted signals and depict a strong correlation with the channel 7 of Landsat sensor except for the fire affected areas (Giglio et al., 2008). Therefore, the potentially unambiguous active fire affected pixels are distinguished based on the following conditions:

$$R_{75} > 2.5 \text{ AND } r_7 - r_5 > 0.3 \text{ AND } r_7 > 0.5 \tag{2.8}$$

Where R_{ij} represents the ratios of the reflectance in channel i and channel j $\left(\text{i. e.}, {}^{r_i}/_{r_j}\right)$, r_i is the measure of reflectance. The test depicted in Eq. (2.8), has been successful in extracting the potentially unambiguous active coal fire affected pixels. However, due to the existence of active fires with higher intensity in a pixel, may lead to Digital Number (DN) folding within the spectral range of channel 7, thereby resulting in the radiometric artifact. In order to detect pixels with such an ambiguous property, the second test has been performed utilizing the channel 1 (0.443 μm band), 5 (0.865 μm band), 6 (1.6 μm band) and 7 (2.2 μm band):

$$r_6 > 0.8 \text{ AND } r_1 < 0.2 \text{ AND } (r_5 > 0.5 \text{ OR } r_7 < 0.1) \tag{2.9}$$

Accompanying the extraction of fire affected pixels, the threshold in Eq. (2.8) is further weaken to select a significant number of candidate pixels for subsequent analysis:

$$R_{75} > 1.8 \text{ AND } r_7 - r_5 > 0.17 \tag{2.10}$$

By executing the aforementioned test sequences, if the shortlisted candidate pixels pass the test (2.10), should meet the subsequent criteria based on fixed thresholds integrated with the contextual tests as depicted here:

$$R_{75} > \overline{R_{75}} + \max\left(3\sigma_{R_{75}}, 0.8\right) \tag{2.11}$$

AND

$$r_7 > \bar{r_7} + \max\left(3\sigma_{r_7}, 0.08\right) \tag{2.12}$$

AND

$$R_{76} > 1.6 \tag{2.13}$$

Where $\bar{r_i}$ and $\sigma_{R_{ij}}$ represent the mean and standard deviation of estimated band ratio (using channel 7 and channel 5) by utilizing a 61 × 61 window centered at valid candidate pixels shortlisted using Eq. (2.10). However, the selection of optimal window size can be investigated considering the spatial variability. Moreover, a pixel can be categorized as a fire affected pixel if its reflectance is greater than zero and meet all the criteria of the aforementioned test sequences $(3.4a - 3.4c)$ and if there exists no ambiguity between water and fire affected pixels. In order to address the effect of water pixels, two distinct tests are executed:

$$\{r_4 > r_5 \text{ AND } r_5 > r_6 \text{ AND } r_6 > r_7 \text{ AND } r_1 - r_7 < 0.2\} \tag{2.14}$$

AND

$$\{(r_3 > r_2) \text{ OR } (r_1 > r_2 \text{ AND } r_2 > r_3 \text{ AND } r_3 > r_4)\} \tag{2.15}$$

The tests in Eq. (2.14) and Eq. (2.15), are distinctly effective in mapping the shallow as well as the deep water bodies respectively. However, the ambiguities may exist between the water pixels and the pixels covered by cloud and shadow as the valid background statistics are not addressed to distinguish between the two (Schroeder et al., 2016). In contrast, the overall active fire detection technique is not affected by the effect of excluding the background statistics mentioned earlier.

2.2.4.2. Nighttime detection

Using the SWIR channel 7 of Landsat 8 OLI, it is possible to retrieve the fire affected pixels from the nighttime scene by incorporating a direct threshold:

$$L_7 > 1 \text{ W m}^{-2} \text{ sr}^{-1} \mu\text{m}^{-1} \tag{2.16}$$

Where L_7 represents the spectral radiance of channel 7. The Eq. (2.16) is similar to Giglio et al. (2008). Furthermore, a detailed treatment of the aforementioned test sequences is depicted and evaluated by Schroeder et al. (2016).

2.3. Satellite-based image fusions

With the rapid development and availability of distinct sensors for miscellaneous remote sensing applications, the possibility of integrating different sensor derived datasets have led the foundation of improving the information in a spatial, temporal and spectral domain. Each and every space-borne sensors have their own distinct characteristics. In reference to earth observation, image fusion can be defined as a process of integrating multiple images to produce a synthetic composite with improved information

content (Goshtasby & Nikolov, 2007). Traditionally, image fusion techniques can be grouped into different categories. According to different processing level, the fusion methods can be classified as a pixel based, feature-based or decision-based fusion (Ehlers, Klonus, Åstrand, & Rosso, 2010). Alternatively, it can also be classified according to multi-source or multi-sensor methods (Zhang, 2010). Another way of categorising the fusion technique is to incorporate the concept of statistical and numerical method, colour related method (HIS, RGB) and hybrid method (Ehlers et al., 2010; Roy et al., 2008; Zhang, 2008). An integrated fusion framework has been depicted in Figure 2.2.

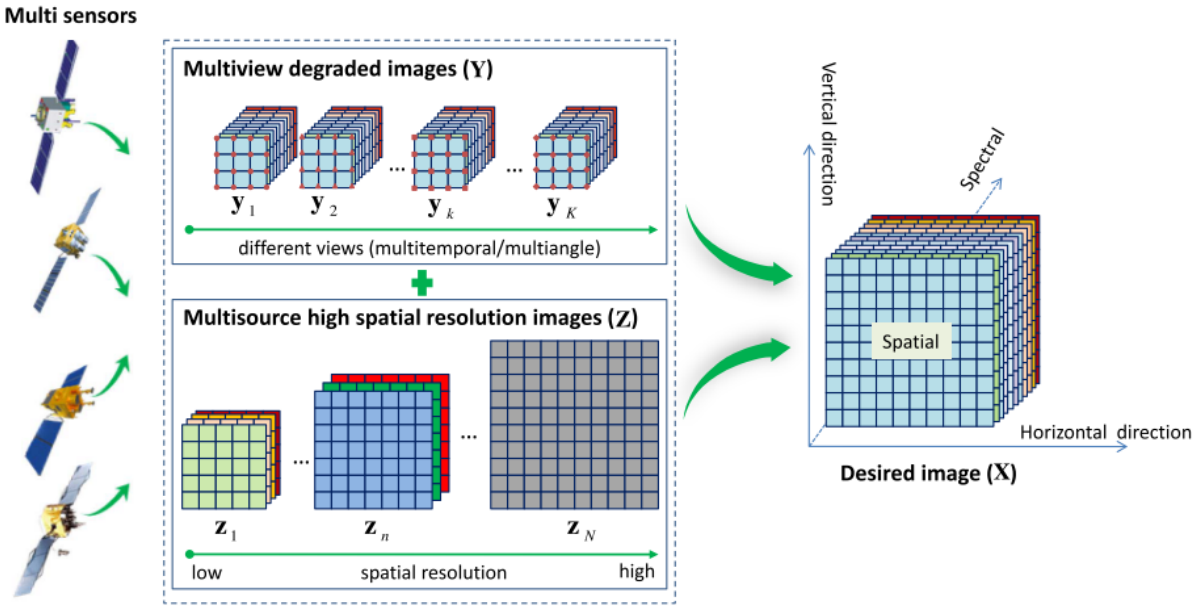

Figure 2.2. A generic fusion framework. Source: Shen, Meng, & Zhang (2016)

Among all the areas of image fusion, a new domain of spatiotemporal image fusion has evolved based on the framework of statistical and numerical methods. These methods incorporate the concept of integrating different satellite-derived images with distinct characteristics (spatial resolution, temporal resolution, orbital characteristics) to produce high spatial and temporal resolution synthetic image. In the next section, the broader view of spatiotemporal fusion has also been depicted.

2.3.1. Spatiotemporal data fusion methods

A theoretical framework of a novel spatiotemporal fusion method was established by Gao et al. (2006) with an objective of producing synthetic daily reflectance images using Landsat (30 m spatial resolution with 16 day revisit) and MODIS (500 m spatial resolution with daily revisit) as an input. Later on, several methods of spatiotemporal fusion have been developed (Zhu et al., 2010; Fu, Chen, Wang, Zhu, & Hilker, 2013; Weng, Fu, & Gao, 2014). The performance evaluation of different methods have been tested over various satellite images such as (i) Landsat and MODIS (Gao et al., 2006; Zhu et al., 2010); (ii) GOES and Landsat (Wu, Shen, Ai, & Liu, 2013); (iii) MODIS and HJ-1 (Meng, Du, & Wu, 2013); (iv) MERIS and Landsat (Zurita-Milla, Kaiser, Clevers, Schneider, & Schaepman, 2009) . Generally, the central idea of each spatiotemporal fusion model is to blend high spatial and low temporal resolution image with the high temporal and low spatial resolution image. Using these concepts, the synthetic images are generated to assess the temporal dynamics of several environmental parameters such as surface reflectance, Normalised Difference Vegetation Index (NDVI), Land Surface Temperature (LST), evapotranspiration (Anderson et al., 2011; Gao et al., 2006; J. Meng et al., 2013; Weng et al., 2014; Wu et al., 2013). According to the recent review by Zhu, Cai, Tian, & Williams (2018), the spatiotemporal fusion model can be broadly categorised

as: (i) unmixing based method (Zhang et al., 2013; Zhukov, Oertel, Lanzl, & Reinhäckel, 1999); (ii) bayesian-based method (Huang et al., 2013; Li et al., 2013); (iii) learning-based method (Huang & Song, 2012; Song & Huang, 2013a); (iv) hybrid method (Rao, Zhu, Chen, & Wang, 2015; Zhu et al., 2016); (v) weighted-function based method (Gao et al., 2006; Zhu et al., 2010). A Generalized schematic layout of spatiotemporal fusion method has been depicted in Figure 2.2.

2.3.1.1. Unmixing-based method

The underlying concept of unmixing based fusion method is to incorporate the classification approaches in generating synthetic composites with high spatial and temporal resolutions. Furthermore, the linear spectral mixing technique is utilized for unmixing the coarse resolution pixels to estimate the value of fine resolution pixels. Using the concept of unmixing based fusion, the first model was introduced by Zhukov et al. (1999) named multi-sensor multi-resolution technique (MMT). The proposed MMT model has four major steps:

1. Defining endmembers by classifying the fine resolution image;
2. Computing the fraction of endmembers for each coarse resolution pixels;
3. Using a pre-defined moving window, unmixing the coarse resolution pixels;
4. Reconstructing an unmixed synthetic image by assigning derived reflectance to fine resolution pixels.

Zurita-Milla et al. (2009) developed an unmixing based model using Medium Resolution Imaging Spectrometer (MERIS, 300 m spatial resolution) and Landsat (30m) time series data. The technique assigns an unmixed signal to the corresponding classes present in the neighbourhood of a central pixel within a moving window. The performance of the above model was strictly dependent on the accuracy and availability of land use land cover (LULC) database. The spatial temporal data fusion approach (STDFA) developed an unmixing model to estimate the change of reflectance from both input and predicted image through moving window, thereby assigning the change to the base fine resolution image (Niu, 2012).

2.3.1.2. Bayesian method

Bayesian-based methods incorporate the theoretical framework of Bayesian estimation to model the relationship between input and predicted images. The central idea of blending input images in Bayesian domain is to maximize the estimated conditional probability associated with corresponding fine and coarse resolution images (Shen et al., 2016). The Bayesian principles coupled with intuitive interpretations were used to model a flexible relationship between input and predicted images (Huang et al., 2013). In essence, the relationship between coarse and fine resolution images can be depicted as two types:

1. The observed coarse and fine resolution image at the same date which is termed as a scale model in Bayesian framework;
2. The temporal relationship between input images which can be described as a temporal model.

Generally, the concept of point spread function (PSF) is used in a scale model to establish a relationship between the fine and coarse resolution image (Xue, Leung, & Fung, 2017). The methods of different Bayesian-based spatiotemporal fusion is used to describe the relationship depending on the rate of change of temporal dynamics governed by several environmental parameters such as phenology, forest fire, and trend of LST. The low pass filtering method was incorporated in unified fusion method to establish the relationship between the fine and coarse resolution images (Huang et al., 2013). The concept of covariance function was first introduced in the Bayesian Maximum Entropy (BME) model to establish a statistical

link between coarse and fine resolution image (Shen et al., 2016). Recently, a new spatiotemporal model was developed by combining the high pass frequency modulated from fine resolution image with the bilinear interpolation of coarse resolution image to establish a scale model integrating with the joint covariance based temporal model (Xue et al., 2017).

2.3.1.3. Learning based method

The theoretical concept of sparse representation-based spatiotemporal fusion model (SPSTFM) was developed by Huang & Song (2012), using three MODIS images (at date t_1, t_2 and t_3) and two Landsat images (t_1 and t_3) as an input to predict the synthetic image product at date t_2. The underlying concept can be depicted as:

1. Incorporating a sparse representation technique to enhance the spatial resolution of MODIS images corresponding to the same resolution of Landsat image (30 m);
2. Constructing an equivalent dictionary pair with corresponding Landsat and MODIS images at date t_1 and t_3 ($M(t_1)$ with $L(t_1)$; ($M(t_3)$ with $L(t_3)$);
3. Predicting and reconstructing the synthetic image using different parameterized weighting function.

Even though SPSTFM provided better accuracy in comparison to STARFM, the method had a computational complexity. Later on, the complexity was reduced by Song & Huang (2013b) using a single pair of MODIS and single Landsat data.

2.3.1.4. Hybrid methods

The hybrid methods use to integrate the concept of distinct fusion techniques to develop an improved spatiotemporal fusion model. Interestingly, the flexible spatiotemporal data fusion (FSDAF) method successfully integrated the concept of weight-based function along with the unmixing based method to predict the abrupt land cover changes in the heterogeneous region (Zhu et al., 2016). Furthermore, the spatial and temporal reflectance unmixing model (STRUM) used a hybrid technique to integrate the concept of unmixing techniques with the theoretical framework of STARFM (Gevaert & García-Haro, 2015).

2.3.1.5. Weight-function based method

The weighted function based methods design a weight based on statistical and numerical techniques and assign it to the central pixel of a moving window for estimating the surface reflectance. Gao et al. (2006) introduced the concept of spatial and temporal adaptive reflectance fusion model (STARFM) to produce synthetic Landsat-like daily surface reflectance product for monitoring phenology changes. Keeping in view of the orbital similarity between Landsat and MODIS, STARFM assumes the rate of change of reflectance between Landsat and MODIS images are consistent and comparable. The three major steps of STARFM includes:

1. Extracting spectrally similar homogeneous pixels from the neighbourhood of Landsat image within a moving window.
2. Computing a weight function and multiply with the summation of the difference of surface reflectance between two MODIS images at two different times at t_1 and t_2 is $\left(M_{t_2} - M_{t_1}\right)$ and Landsat image at t_1 $\left(L_{t_1}\right)$.
3. Generating synthetic image at time t_2 by assigning the weighted sum to the central pixel of the moving window.

Although STARFM generates the synthetic Landsat-like images, the major limitations include: (i) performance degrades while considering the heterogeneous region; (ii) the window size has to be tested for different applications; (iii) the spectrally similar homogeneous pixels may not present within the moving window. To overcome these limitations associated with heterogeneity, Zhu et al. (2010) developed an Enhanced STARFM (ESTARFM) model. A new concept of conversion coefficient was introduced to perform a regression analysis of spectrally similar homogeneous pixels using a dual pair of MODIS and Landsat data at two different dates. Using a dual pair of MODIS and Landsat datasets at two different dates $t_1$and t_3, the synthetic image is produced in an intermediate date t_2 $(t_1 < t_2 < t_3)$. Even though the prediction accuracy was comparable with the original STARFM, it had similar problems associated with computation complexity and the size of the window as well as a selection of spectrally similar homogeneous pixels. In order to overcome the above limitations, Fu et al. (2013) modified the criteria for selecting spectrally similar homogeneous pixels. However, it had the same problem of computational complexity. Consequently, the concept of STARFM was used to miscellaneous applications such as evapotranspiration (Anderson et al., 2011), daily surface temperature retrieval (Liu & Weng, 2012). Integrating the concept of annual temperature cycle with the existing STARFM model, Weng et al. (2014) developed a spatiotemporal adaptive data fusion (SADFAT) model for temperature mapping.

2.4. Theoretical framework of spatiotemporal fusion methods

The spatiotemporal data fusion techniques have been widely used for various remote sensing applications. Gao et al. (2006) developed a novel spatiotemporal fusion technique named spatiotemporal adaptive reflectance fusion model (STARFM) using Landsat and MODIS images as an input.

However, the author had also mentioned the possibility of using Landsat and VIIRS data as an input to explore the different domain of remote sensing applications. It was developed by selecting the pixels with spectral similarity (high spatial resolution image) within a moving window. Using those spectrally similar pixels, the subsequent weights are assigned to the central pixel for computing the surface reflectance at the predicted date. The corresponding weights are computed using the concept of the spectral difference, spatial difference and temporal difference between the spectrally similar pixels with the subsequent coarse and fine resolution pixels. Figure 3.2 depicts an underlying working principle of STARFM.
The input dataset which has been used to blend and produce a synthetic Landsat like image (Figure 3.2):

1. Coarse resolution image (VIIRS) at t_1
2. Fine resolution image (Landsat 8 OLI / TIRS) at t_1
3. Coarse resolution image (VIIRS) at t_2

2.4.1. Algorithmic overview of STARFM

The pre-requisite criterion of implementing the STARFM algorithm is to calibrate the observation from different sensors (pre-processing such as re-projection, resampling, scaling of the reflectance value) into surface reflectance, including the atmospheric correction. However, the systematic biases are anticipated due to the dissimilarities associated with the chain of processing scheme, bandwidth, spectral response function, geolocation error and distinct sensor characteristics.

If the aforementioned biases are neglected, a coarse resolution heterogeneous pixel with a surface reflectance of H_t can be aggregated to a linear combination of the product of surface reflectance (F_t^i) of fine resolution homogeneous pixels with the fraction of area coverage (A_t^i) by individual pixel:

$$H_t = \sum_{i=1}^{n} F_t^i \times A_t^i \tag{2.17}$$

Where i is the spatial index of corresponding homogeneous pixels, and n denotes the number of homogeneous pixels within the spatial bound of a coarse resolution heterogeneous pixel. However, it is difficult to get a unique solution (using Eq. (2.17) considering the similarity of areas for all the fine resolution pixels. Therefore, if it is possible to get the value of F_t^i from the neighbouring pixels, the corresponding biases between actual and predicted pixels can be eliminated.

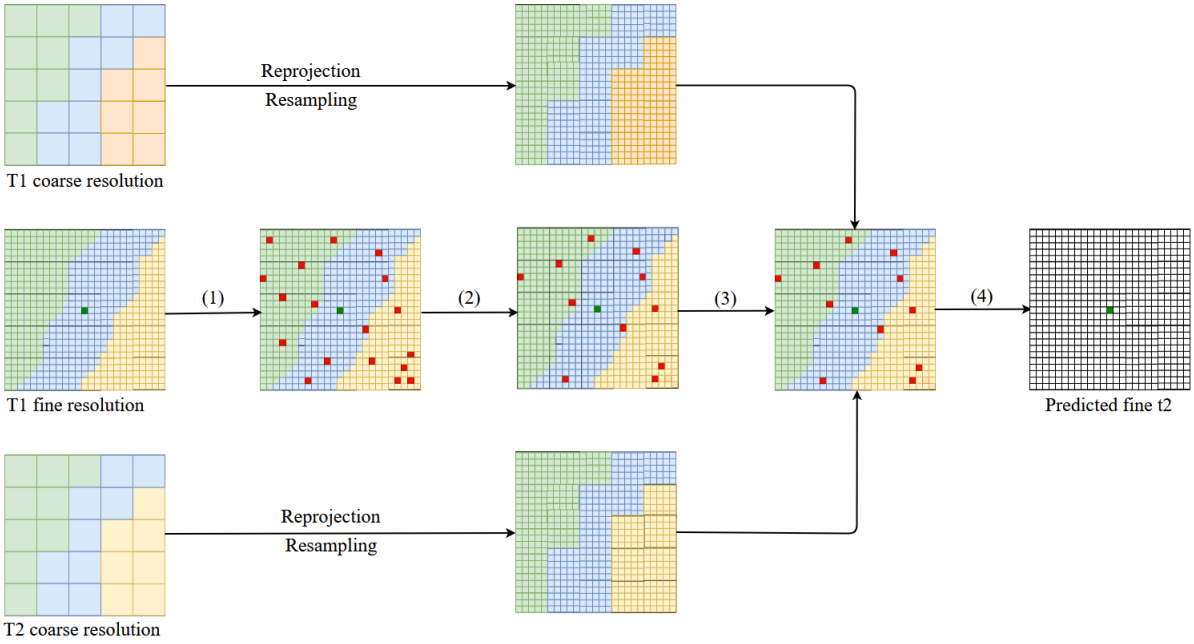

Figure 2.2. The Schematic working principle of STARFM. Initially, the fine resolution image at t_1 is used to search for spectrally similar homogeneous pixels within a moving window in step (1). In the next step (2), the homogeneous pixels (marked red) are further filtered out from a moving window (central pixel marked in green). Afterwards, the weight is assigned to the central pixel according to the spectral difference, spatial difference and temporal difference derived from the pixels associated with the single pair of coarse resolution images at t_1 and t_2 and fine resolution image at t_1 considering the corresponding location of spectrally similar homogeneous pixels (3). At last, the reflectance of the central pixel is estimated (4) using the combined weight derived in step (3).

Hence, the goal is to extract spectrally similar homogeneous pixels considering the effect of the neighbourhood for a candidate pixel. After performing the down-scaling operation (bilinear interpolation, nearest neighbour interpolation) of VIIRS surface reflectance product within the bounds of the spatial resolution of Landsat 8 OLI product, the surface reflectance value of a fine resolution homogeneous pixel can be expressed as:

$$L(x_i, y_i, t_k) = V(x_i, y_i, t_k) + \varepsilon_k \tag{2.18}$$

Where (x_i, y_j) is the location of both Landsat 8 OLI and VIIRS pixel which shares the same size and coordinate system, and t_k represents the acquisition date, $L(x_i, y_i, t_k)$ and $V(x_i, y_i, t_k)$ represent the surface reflectance of Landsat 8 and VIIRS respectively, ε_k denotes the difference in surface reflectance.

Now if we want to predict the surface reflectance of Landsat 8 at t_p, the predicted value of synthetic pixels can be expressed as:

$$L(x_i, y_i, t_p) = V(x_i, y_i, t_p) + \varepsilon_p \tag{2.19}$$

If the topographic changes and system errors are neglected within the prediction date (t_p) and estimation date (t_k), the assumption of $\varepsilon_k = \varepsilon_p$ will lead to:

$$L(x_i, y_i, t_p) = V(x_i, y_i, t_p) + L(x_i, y_i, t_k) - V(x_i, y_i, t_k) \tag{2.20}$$

However, the situation in Eq. (2.20) cannot be satisfied because of changes in topography between the date t_k and t_p, differential solar geometry, variations in bidirectional reflectance distribution function (BRDF) and associated biases in reference to the distinct sensor. Therefore, to estimate the surface reflectance of the central pixel of a moving window, the computation of the weight (W_{ijk}) plays a pivotal role. The weight is estimated using the spectral, spatial and temporal difference between the corresponding VIIRS and Landsat pixels (spectrally similar and homogeneous) simultaneously extracted within a moving window.

$$L(x_{w/2}, y_{w/2}, t_p) = \sum_{i=1}^{w} \sum_{j=1}^{w} \sum_{k=1}^{n} W_{ijk} \times \left(V(x_{i,} y_{j,} t_p) + L(x_{i,} y_{j,} t_k) - V(x_{i,} y_{j,} t_k)\right) \tag{2.21}$$

Where $w \times w$ denotes the area of the square window, $L(x_{i,}\, y_{j,}\, t_k)$ indicates the predicted value of synthetic Landsat pixel. In order to compute the weight (W_{ijk}), the spectrally similar homogeneous pixels have to be extracted. In order to perform the aforementioned task, the criteria can be established considering the overall spectral variance of an image within a distinct spectral domain and the number of classes associated with a chosen study area:

$$\left|L(x_{i,}\, y_{j,}\, t_k) - L\left(xw_{/2,}\, yw_{/2,}\, t_k\right)\right| \leq 2 \times \frac{\sigma(B)}{n} \tag{2.22}$$

Where $L(x_{i,}\, y_{j,}\, t_k)$ denotes a pixel belonging to the domain of square window, $\sigma(B)$ indicates the standard deviation of the entire image with band B, n denotes the number of classes of a chosen study area. If a pixel satisfies the criteria in Eq. (2.22), it will be termed as a spectrally similar homogeneous pixel. After extracting those spectrally similar homogeneous pixels within a moving window from the Eq. (2.22) , the computation of the weight (W_{ijk}) is performed by considering the spectral difference, spatial difference and temporal difference between the homogenous pixels in Landsat 8 and the pixels with a similar location in VIIRS within a moving window of equal size.

2.4.1.1. Spectral Difference:

The spectral difference is the estimate of the difference between the value of surface reflectance of a Landsat 8 homogeneous pixel $L(x_{i,}\, y_{j,}\, t_k)$ and the VIIRS pixel $V(x_{i,} y_{j,} t_k)$ within the same moving window.

$$S_{ijk} = \left|L(x_{i,}\, y_{j,}\, t_k) - V(x_{i,} y_{j,} t_k)\right| \tag{2.23}$$

Where S_{ijk} indirectly measures the approximate homogeneity between the VIIRS pixels. Therefore, a smaller value in Eq. (2.23) indicates the spectral similarity within the proximity of fine resolution pixels. If $S_{ijk} = 0$, the predicted value of surface reflectance should also be equal to the value of $L(x_i, y_j, t_k)$.

2.4.1.2. Temporal Difference:

The temporal difference is the estimate of the difference between the value of surface reflectance of a VIIRS pixel $V(x_i, y_j, t_p)$ at the predicted date and the VIIRS pixel $V(x_i, y_j, t_k)$ at date t_k within the similar moving window. The location (x_i, y_j) is similar to the homogeneous pixel of Landsat 8.

$$T_{ijk} = \left| V(x_i, y_j, t_p) - V(x_i, y_j, t_k) \right| \tag{2.24}$$

Where T_{ijk} measures the rate of change of reflectance between t_p and t_k for a VIIRS pixel at the location of (x_i, y_j). The higher value of the temporal difference in Eq. (2.24), typically indicates a rapid change of phenology between the observed and the predicted date.

2.4.1.3. Spatial Difference:

The spatial difference is the measure of the Euclidean distance between a candidate homogeneous pixel and a central pixel within a moving window at the date t_k

$$d_{ijk}{}^2 = \left(x_i - x_{w/2}\right)^2 + \left(y_i - y_{w/2}\right)^2 \tag{2.25}$$

The distance mentioned in Eq. (2.25), has been converted to a relative distance D_{ijk} by considering the implementation scheme:

$$D_{ijk} = 1.0 + \frac{d_{ijk}}{A} \tag{2.26}$$

Where A is the measure of relative importance of spatial distance with respect to the spectral and temporal difference. A is normally kept as the half of the width of the square window $(w/2)$ during the time of implementation. Generally, the value of the weight is inversely proportional to the distance between a central pixel and a spectrally similar pixel.

2.4.1.4. Combined weight

If we combine the spectral difference(S_{ijk}), temporal difference (T_{ijk}) and spatial difference(D_{ijk}), the resulting equation will be:

$$C_{ijk} = S_{ijk} \times T_{ijk} \times D_{ijk} \tag{2.27}$$

The normalised reverse distance is considered as a weight function (W_{ijk}):

$$W_{ijk} = \left(\frac{1}{C_{ijk}}\right) / \left(\sum_{i=1}^{w} \sum_{j=1}^{w} \sum_{k=1}^{n} \frac{1}{C_{ijk}}\right) \tag{2.28}$$

If the VIIRS surface reflectance does not change from t_k to t_p, the resulting value will be $V(x_i, y_j, t_p) = V(x_i, y_j, t_k)$, then $T_{ijk} = 0$ and $C_{ijk} = 0$, and the weight (W_{ijk}) is set to maximum value. In that case, the resulting value of the synthetic central pixel will be $L\left(xw_{/2}, yw_{/2}, t_p\right) = L\left(xw_{/2}, yw_{/2}, t_k\right)$. The initial assumption was, if no changes happen in the surface reflectance of VIIRS, then no changes should happen in the Landsat 8 OLI.

On the other hand, if the Landsat 8 surface reflectance is equal to the surface reflectance of VIIRS. $L(x_i, y_j, t_k) = V(x_i, y_j, t_k)$, then $S_{ijk} = 0$ and $C_{ijk} = 0$, and the weight (W_{ijk}) is set to maximum value. Therefore, the resulting value of the synthetic central pixel would be estimated as $L\left(xw_{/2}, yw_{/2}, t_p\right) = V\left(xw_{/2}, yw_{/2}, t_p\right)$.

2.4.2. Algorithmic overview of Enhanced STARFM:

Zhu et al. (2010) further improved the STARFM for heterogeneous surfaces using the concept of linear regression and conversion coefficient to assign a weight for estimating the predicted reflectance.

The basic assumption of ESTARFM is that the data derived from different sensors with the same acquisition date are comparable after atmospheric correction, radiometric calibration and geometric correction. However, systematic biases are expected due to dissimilarities associated with the orbital parameters, spectral bandwidth, and differential radiometric response of the corresponding sensors. The central idea of ESTARFM is to consider the correlation between multisource data to fuse information within a similar spectral range of multi-sensors. Moreover, the concept of heterogeneity of earth surface is introduced to further improve the performance of original STARFM.

The input dataset which has been used to blend and produce a synthetic Landsat like image (Figure

1. Coarse resolution images (VIIRS) at t_1 and t_3
2. Fine resolution image (Landsat 8 OLI / TIRS)at t_1 and t_3
3. Coarse resolution image (VIIRS) at t_2

2.4.2.1. Pure coarse-resolution pixel

With an assumption of the coarse-resolution image being re-projected and resampled to the same bounds and extent of a fine resolution image, the difference between the value of coarse resolution and fine resolution pixel results from systematic errors. Moreover, those errors cannot be corrected by geometric rectification, atmospheric correction and all other sources associated with it.

Therefore, a linear model can be established considering the reflectance value of corresponding coarse and fine resolution pixels as:

$$F(x, y, t_k, B) = a \times C(x, y, t_k, B) + b \tag{2.29}$$

Where F, C is the value of fine and coarse resolution surface reflectance, (x, y) denotes the location of pixels, t_k is the acquisition date, B corresponds to band with similar spectral range, a and b are the coefficient of the linear regression model. With an extended assumption of sensor stability, the Eq. (2.29) should be consistent. However, due to the differences in solar geometry, altitude variation, and associated bias, systematic variability cannot be eliminated. Therefore, there exists a location dependency of the coefficients a and b in Eq.(2.29).

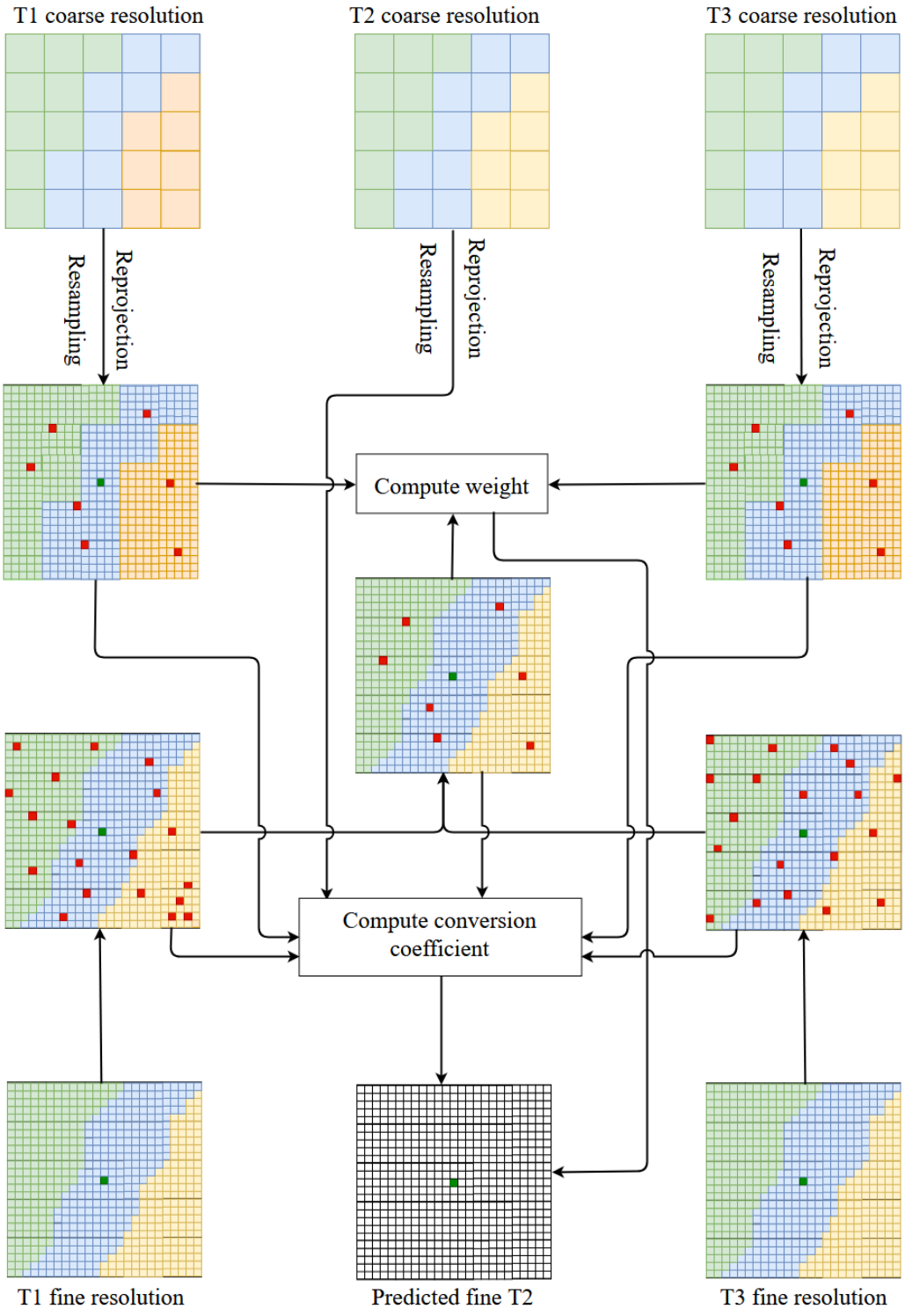

Figure 2.3. The schematic working principle of ESTARFM. At first, the spectrally similar homogeneous pixels (marked in red) are extracted from a moving window (central pixel marked in green) using fine resolution image at t_1 and t_3. Moreover, the intersection of similar pixels along with the corresponding pixels from the re-projected and resampled coarse resolution images (marked in red) at t_1 and t_3 are used to compute weight. In the next step, the reflectance of the central pixel is computed using the estimated weight and conversion coefficient of similar pixels.

Henceforth, the localised value of a and b should be taken into consideration. If two images are acquired simultaneously at the date t_0 and t_p, the Eq. (2.29) can be written as Eq. (2.30) and Eq. (2.31):

$$F(x, y, t_o, B) = a \times C(x, y, t_o, B) + b \tag{2.30}$$

$$F(x, y, t_p, B) = a \times C(x, y, t_p, B) + b \tag{2.31}$$

From Eq. (2.30) and Eq. (2.31), the following equation can be obtained:

$$F(x, y, t_p, B) = F(x, y, t_o, B) + a \times \left(C(x, y, t_p, B) - C(x, y, t_o, B)\right) \tag{2.32}$$

The Eq. (2.32) shows the predicted reflectance at date t_p is the sum of fine resolution reflectance at a date t_o and the change of reflectance between the corresponding coarse-resolution pixels at t_o and t_p with a coefficient of a. If two pairs of the input image at a time t_m and t_n are acquired, the correlation coefficient can be obtained using linear regression between fine resolution pixels against coarse resolution pixels at a time t_m and t_n . Consequently, the correlation coefficient is valid for surfaces which do not change rapidly between observed and predicted date.

2.4.2.2. Heterogeneous coarse-resolution pixel

Due to the existence of heterogeneity of land cover surfaces, most of the pixels exhibit complex property. If a mixed pixel can be modelled by the product of fractional area coverage of a land cover type with the corresponding reflectance, a mathematical relationship can be established between the changes in reflectance from t_m to t_n. Assuming the negligible change in surface properties between t_m and t_n, the relationship between the reflectance of coarse resolution heterogeneous pixel and the fine-resolution homogeneous pixel can be written as:

$$C_m = \sum_{i=1}^{M} f_i \left(\frac{1}{a} F_{im} - \frac{b}{a}\right) + \varepsilon \tag{2.33}$$

$$C_n = \sum_{i=1}^{M} f_i \left(\frac{1}{a} F_{in} - \frac{b}{a}\right) + \varepsilon \tag{2.34}$$

Where C_m and C_n are the corresponding reflectance (coarse resolution) at the date t_m and t_n respectively, f_i denotes the fractional area coverage of i^{th} endmember, F_{im} and F_{in} denotes the reflectance (fine resolution image) of i^{th} endmember, M is the total number of endmembers, a and b denotes the relative calibration coefficient between coarse resolution and fine resolution pixels. Here, all the fine resolution pixels within the bounds of coarse resolution pixels can be attributed to the relative endmembers. From Eq. (2.33) and Eq. (2.34), it can be written as:

$$C_n - C_m = \sum_{i=1}^{M} \frac{f_i}{a} (F_{in} - F_{im}) \tag{2.35}$$

An extended assumption can be made to model a linear change in reflectance of each endmember from the time t_m to t_n. Therefore, a linear relationship can be established between the changes of reflectance of i^{th} endmember from time t_m to t_n.

$$F_{in} = h_i \times \Delta t + F_{im} \tag{2.36}$$

Where $\Delta t = t_m - t_n$, h_i represents the rate of change of reflectance between t_m and t_n. The assumption of linearity between the short periods can be made as it is difficult to model a non-linear relationship of the rate of change of reflectance due to the heterogeneous complexity of earth surfaces. Then, the Eq. (2.35) can be rewritten as:

$$C_n - C_m = \Delta t \times \sum_{i=1}^{M} \frac{f_i \times h_i}{a} \tag{2.37}$$

With the known value of surface reflectance of l^{th} endmember at date t_m and t_n, the difference Δt can be represented as:

$$\Delta t = \frac{F_{ln} - F_{lm}}{h_l} \tag{2.38}$$

Where h_l denotes the rate of change of reflectance of l^{th} endmember between date t_m and t_n. Combining Eq. (2.37) and Eq. (2.38), it can be encapsulated as:

$$\frac{F_{ln} - F_{lm}}{C_{ln} - C_{lm}} = \frac{h_l}{\sum_{i=1}^{M} \frac{f_i \times h_i}{a}} = v_l \tag{2.39}$$

The right part of the Eq. (2.39), depicts the ratio of the rate of change of reflectance for l^{th} endmember and a mixed coarse resolution pixel. Thus, the value of v_l represents a proportion of linearity between each endmember against a coarse resolution heterogeneous pixel aligning with the prior assumption of linearity. In this case, an endmember is considered to be a fine resolution pixel (x, y) falling within the bound of the coarse-resolution heterogeneous pixel. Therefore, for each endmember, a conversion coefficient $v(x, y)$ can easily be determined using linear regression. With a single pair of fine and coarse resolution image, the predicted reflectance at (x, y) can be rewritten as:

$$F(x, y, t_p, B) = F(x, y, t_o, B) + v(x, y) \times \left(C(x, y, t_p, B) - C(x, y, t_o, B)\right) \tag{2.40}$$

As the Eq. (2.32) and Eq. (2.40), has a similar form, but Eq. (2.32) depicts that the pure pixels are normalised between different resolution images, however, the Eq. (2.40) determines the relationship between the rate of change of reflectance between an endmember and a coarse resolution heterogeneous pixel. Moreover, Eq. (2.32) and Eq. (2.40) considers only distinct information from a single pixel, however, the result can be further improved by introducing the concept of moving window to extract spectrally similar homogeneous pixels from the neighbourhood (Gao et al., 2006). Therefore, Eq. (2.40) can be further modified by assuming a square window (area w × w) and considering the central pixel of that window as:

$$F\left(x_{\frac{w}{2}},\ y_{\frac{w}{2}}, t_p, B\right) = F\left(x_{\frac{w}{2}},\ y_{\frac{w}{2}}, t_o, B\right) + \sum_{i=1}^{N} W_i \times V_i \times \left(C(x_i, y_i, t_p, B) - C(x_i, y_i, t_o, B)\right) \quad (2.41)$$

Where N denotes the number of spectrally similar homogeneous pixels including the central pixel of the moving window, (x_i, y_j) denotes the location of i^{th} similar pixel, W_i is the weight contributed by i^{th} similar pixel. The homogeneous pixels are characterised by similar land cover type as the central pixel within a window. The window size w is inversely proportional to the homogeneity of the surface. V_i is the conversion coefficient of i^{th} similar pixel.

2.4.2.3. Extraction of spectrally similar homogeneous pixels

The spectrally similar homogeneous pixels are extracted either by performing unsupervised clustering method or by incorporating fixed-thresholding technique using the difference of reflectance value between central pixels of a moving window with all other pixels. The homogeneous pixels are extracted using the Eq. (2.22) as described in Section 2.4.1.

2.4.2.4. Computation of weight (W_i)

The weight W_i for i^{th} similar pixels are computed by incorporating the concept of the contribution of each similar pixel with respect to their corresponding spatial distance from a central pixel of the moving window. The pixel with higher similarity and lesser distance contributes to the higher weight. The correlation coefficient of each fine-resolution pixel with corresponding coarse resolution pixel within the same moving window is used to compute weight:

$$R_i = \frac{E\left[\left(F_i - E(F_i)\right)\left(C_i - E(C_i)\right)\right]}{\sqrt{V(F_i) \times V(C_i)}} \quad (2.42)$$

$$F_i = \{F(x_i, y_i, t_m, B_1), \ldots, F(x_i, y_i, t_m, B_N), F(x_i, y_i, t_n, B_1), \ldots, F(x_i, y_i, t_n, B_N)\}$$

$$C_i = \{C(x_i, y_i, t_m, B_1), \ldots, C(x_i, y_i, t_m, B_N), C(x_i, y_i, t_n, B_1), \ldots, C(x_i, y_i, t_n, B_N)\}$$

Where R_i indicates the spectral correlation coefficient of each similar pixel within a moving window, F_i and C_i denotes the spectral vector of each spectrally similar pixels for each band (from B_1 to B_N) at time t_m and t_n. $V(F_i), V(C_i)$ denotes the variance of fine and coarse resolution pixels respectively. The range of R_i varies between -1 to +1. The spectral distance between a similar pixel and central pixel is determined using Euclidean distance:

$$d_i = 1 + \frac{\sqrt{\left(x_i - x_{w/2}\right)^2 + \left(y_i - y_{w/2}\right)^2}}{w/2} \quad (2.43)$$

After combining the Eq. (2.42) and Eq. (2.43), an index (D_i) can be used to represent the relative contribution of each pixel:

$$D_i = (1 - R_i) \times d_i \quad (2.44)$$

In the Eq. (2.44), a larger value of D_i represents a relatively lesser contribution towards computing the synthetic reflectance of a predicted pixel located at the centre of the moving window. Therefore, the normalised weight of each similar pixel with respect to all other similar pixels within a moving window can be defined as:

$$W_i = \frac{1/D_i}{\sum_{i=1}^{N} 1/D_i} \tag{2.45}$$

The range of W_i varies from 0 to 1, and the combined weight of all similar pixels within a moving window is 1. In a situation where 'P' number of extracted similar pixels and their corresponding coarse resolution pixels are pure, the weights are assigned as $1/P$ for those pixels, and the weights of the $(N - P)$ pixels are assigned according to the Eq. (2.45).

2.4.2.5. Calculation of the conversion coefficient(V_i)

The linear regression analysis considering all the similar pixels within a moving window is performed to estimate the conversion coefficient. The gradient of the linear regression line (for every moving window) is the actual measure of v_i after computing the correlation of each fine resolution pixel against the corresponding coarse resolution pixel at date t_m and t_n. Due to several constraints associated with the pre-processing of both coarse and fine resolution images in relation to the non-removal of positional accuracy as well as systematic biases, aggregating information from spectrally similar homogeneous pixels from the neighbourhood would be reliable to estimate the conversion coefficient.

2.4.2.6. Estimation of the reflectance of the central pixel

After estimating the value of weight (W_i) as well as the conversion coefficient (V_i), the prediction of higher resolution reflectance at the date t_p is performed using two pairs of fine and corresponding coarse resolution images at the date t_m and t_n with an additional coarse resolution image at the date t_p. Consequently, the normalised-inverse change of reflectance between the prediction date t_p and base date t_m and t_n is used to estimate the following parameter:

$$T_k = \frac{1/\left|\sum_{i=1}^{w}\sum_{j=1}^{w} C(x_i, y_j, t_k, B) - \sum_{i=1}^{w}\sum_{j=1}^{w} C(x_i, y_j, t_p, B)\right|}{\sum_{k=m,n} 1/\left|\sum_{i=1}^{w}\sum_{j=1}^{w} C(x_i, y_j, t_k, B) - \sum_{i=1}^{w}\sum_{j=1}^{w} C(x_i, y_j, t_p, B)\right|} \tag{2.46}$$

Where T_k denotes the temporal weight of each pixel with respect to all other similar pixels. Therefore, the accuracy of prediction can be increased by incorporating a linear combination of temporal weight with the corresponding synthetic central reflectance value at date t_p. Thus, the final reflected radiance can be written as:

$$F\left(xw/2,\ yw/2, t_p, B\right) = T_m \times F_m\left(xw/2,\ yw/2, t_p, B\right) + T_n \times F_n\left(xw/2,\ yw/2, t_p, B\right) \tag{2.47}$$

3. METHODOLOGY

This chapter highlights the methods and approaches used for detecting coal fire affected pixels in actual Landsat images as well as synthetically predicted Landsat like images generated from the various multi-sensor fusion methods. **Section 3.1** describes the flowchart of experiments conducted for the current study. **Section 3.2** elucidates the novel coal fire detection method established. **Section 3.3** depicts the modifications performed on ESTARFM and STARFM method. **Section 3.4** describes the qualitative and quantitative assessment of synthetic products derived from spatiotemporal fusion methods.

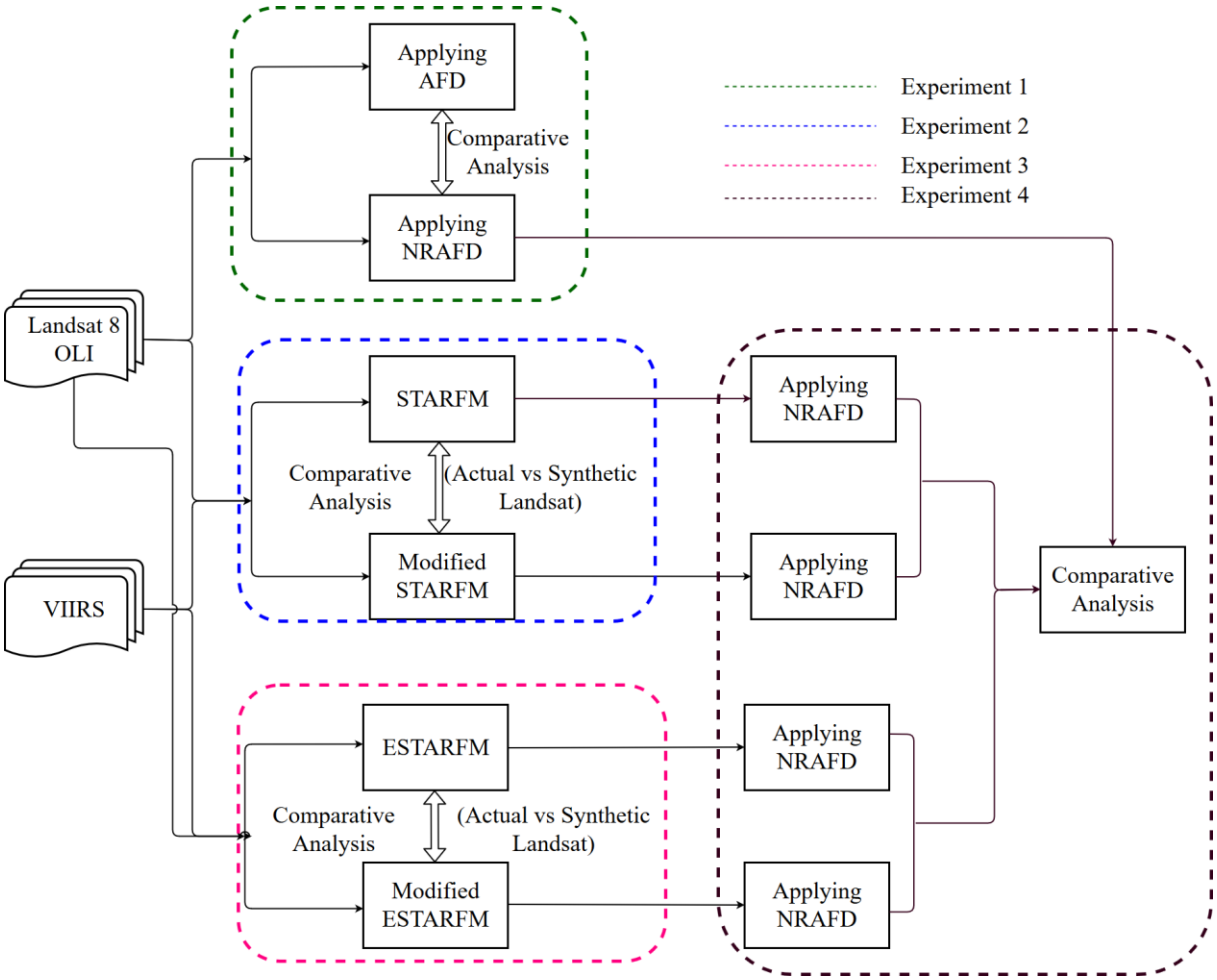

Figure 3.1. The experimental setup

3.1. Experimental setup

The Landsat 8 OLI and VIIRS were used to detect the coal fire from the actual image and synthetically predicted image derived from spatiotemporal fusion method. In Figure 3.1, it was shown that several experiments were conducted in subsequent stages of research.

3.1.1. Experiment 1

In the first experiment as shown in Figure 3.1, Landsat-8 data was used to detect and delineate the coal fire affected pixels by incorporating the AFD. After observing the underestimation caused by AFD, a

novel coal fire detection method named Normalised Reflectance-based Active Fire Detection (NRAFD) method was established. Furthermore, a comparative analysis was performed between AFD and NRAFD. The results and the associated comparative analysis of the first experiment were reported to Section 5.1.

Due to the unavailability of a reference map of coal fire for the chosen study area, a visual inspection was carried out to assess the fidelity of the newly developed NRAFD method for extracting coal fire affected pixels. However, it is difficult to investigate the mixed pixels which are lying within the close proximity of the coal fire regions. The pixels which are appeared as bright yellow and yellowish red using the FCC composite of band 5, band 6 and band 7 in Landsat 8 OLI, are referred to as coal fire affected pixels.

3.1.2. Experiment 2

The second experiment was carried out with the implementation of STARFM and the modified STARFM in a python environment. The quantitative and qualitative assessments of the fused products derived from these two spatiotemporal fusion methods were performed by several metrics (Section 3.4). The assessments of the synthetic Landsat products were done by producing the fused images on a particular date overlapping with the 16 days repeat cycle of Landsat-8 OLI sensor. The results and comparative analysis of experiment 2 were illustrated in Section 5.2.

For STARFM and modified STARFM, the actual Landsat and VIIRS datasets on December 24, 2017, along with another dataset of VIIRS on January 9, 2018, were used to generate a synthetic Landsat image January 9, 2018.

3.1.3. Experiment 3

In the third experiment as depicted in Figure 3.1, the ESTARFM and modified ESTARFM were executed in a python environment. The subsequent qualitative and quantitative assessments of the fused products derived from these two spatiotemporal fusion methods were carried out using several metrics (Section 3.4). The assessments of the fused products were performed by producing the synthetic image on a particular date overlapping with the 16 days repeat cycle of Landsat-8 OLI sensor.

For ESTARFM and modified ESTARFM, one pair of actual Landsat-8 and VIIRS on December 24, 2017 (1st observed date) and one pair of actual Landsat-8 and VIIRS on January 25, 2018 (2nd observed date), were used to generate a synthetic image on January 9, 2018 (predicted date). A detailed treatment of these experimental results and associated comparative analysis was reported to Section 5.2.2.

3.1.4. Experiment 4

In the fourth experiment in Figure 3.1, the NRAFD method was executed on synthetic products derived from experiment 2 and experiment 3. After that, the results of different synthetic coal fire maps were compared with the actual coal fire map from experiment 1 on the same date. The comparative analysis was carried out by deriving confusion matrix for actual and synthetic coal fire map. The results and associated comparative analysis were highlighted in Section 5.3.

The reason of selecting the prediction date on January 9, 2018, was that an actual Landsat scene was available on the chosen date, and hence, the necessary performance evaluation between different fusion methods was carried out based on several assessment metrics.

3.2. Normalised Reflectance-based Active Fire Detection Method (NRAFD)

The NRAFD method was developed by using the stepwise normalisation between the concurrent fire responsive channels of Landsat 8 OLI sensors from NIR to SWIR region respectively. Using the AFD algorithm, the actual surface coal fire pixels were extracted by incorporating the concurrent test sequences (Section 2.2.4). Consequently, the spectral pattern of the fire affected pixels was extracted using all the spectral channel of Landsat 8 OLI data. The interpretation of spectral trend and the associated channel-specific normalisation procedures have been elucidated below.

3.2.1. Interpretation of spectral trend

The spectral pattern (lower left in Figure 3.3) clearly depicts that between the channels 5 to 7, the trend of surface reflectance is strictly increasing for active fire pixels. Moreover, the slope between channels 6 and 7 was significantly higher than the slope between channels 5 and 6. Interestingly, the effect of corresponding slopes was addressed by channel-specific normalisation between band 5, band 6 and band 7 for designing criteria to distinguish those pixels which were following the spectral trend as depicted in Figure 3.3.

3.2.2. Channel-specific normalisation

Let us assume that the surface reflectance of a typical fire affected pixel is ρ_5, ρ_6 and ρ_7 for channels 5 to 7 respectively. The band-specific normalisation between the band 7 and band 6 as well as band 6 and band 5 will be:

$$I_1 = \frac{\rho_7 - \rho_6}{\rho_7 + \rho_6} \text{ AND } I_2 = \frac{\rho_6 - \rho_5}{\rho_6 + \rho_5} \tag{3.1}$$

If the ratio between the reflectance $\varepsilon_{67} = {\rho_6}/{\rho_7}$ and $\varepsilon_{56} = {\rho_5}/{\rho_6}$ are replaced in the Eq. (3.1), it will yield in the form:

$$I_1 = \frac{1 - \varepsilon_{67}}{1 + \varepsilon_{67}} \text{ AND } I_2 = \frac{1 - \varepsilon_{56}}{1 + \varepsilon_{56}} \quad \text{where,} \quad \varepsilon_{67}, \varepsilon_{56} \leq 1 \tag{3.2}$$

The criteria $\varepsilon_{67}, \varepsilon_{56} \leq 1$ will satisfy the properties of coal fire affected pixels as depicted in Figure (3.3). Furthermore, the scatterplot also illustrates a strong correlation between the channel 5 and the channel 7 as well as between the channel 6 and channel 7, except for the anomalous fire affected pixels (encircled in red, Figure 3.2). Therefore, to select the candidate pixels, the ratios were exploited vis-à-vis spectral trend.

Now, it is known that the band 7 and band 6 receive emitted as well as reflected radiation and the sensitivity of band 7 is greater than band 6 in respect of capturing the emitted radiation from the fire affected areas. However, the slope between band 7 and band 6 is greater than the slope between band 6 and band 5 (Figure 3.7). Therefore, it can be written as:

$$\varepsilon_{67} < \varepsilon_{56} = \begin{cases} 1 + \varepsilon_{67} < 1 + \varepsilon_{56} \\ 1 - \varepsilon_{67} > 1 - \varepsilon_{56} \end{cases} \tag{3.3}$$

Utilizing the equations Eq. (3.1), Eq. (3.2) and Eq. (3.3), the overall criteria can be integrated to:

$$I_1 = \frac{\rho_7 - \rho_6}{\rho_7 + \rho_6} > 0.0 \text{ AND } I_2 = \frac{\rho_6 - \rho_5}{\rho_6 + \rho_5} > 0.0 \text{ AND } I_1 > I_2 \tag{3.4}$$

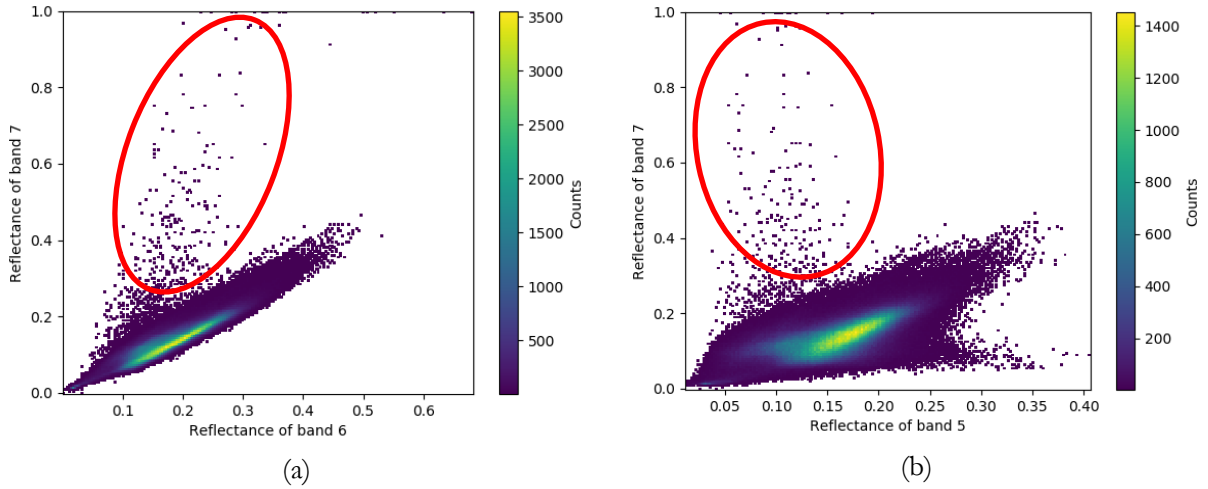

Figure 3.2: Scatter plots between SWIR and NIR channel of subset extracted from Landsat 8 OLI data. (a) – the scatterplot between the reflectance of band 6 and band 7 of Landsat 8 data. (b) – the scatter plot between the reflectance of band 5 and band 7 of Landsat 8 OL data. The value 1.6 typically indicates the sensor saturation.

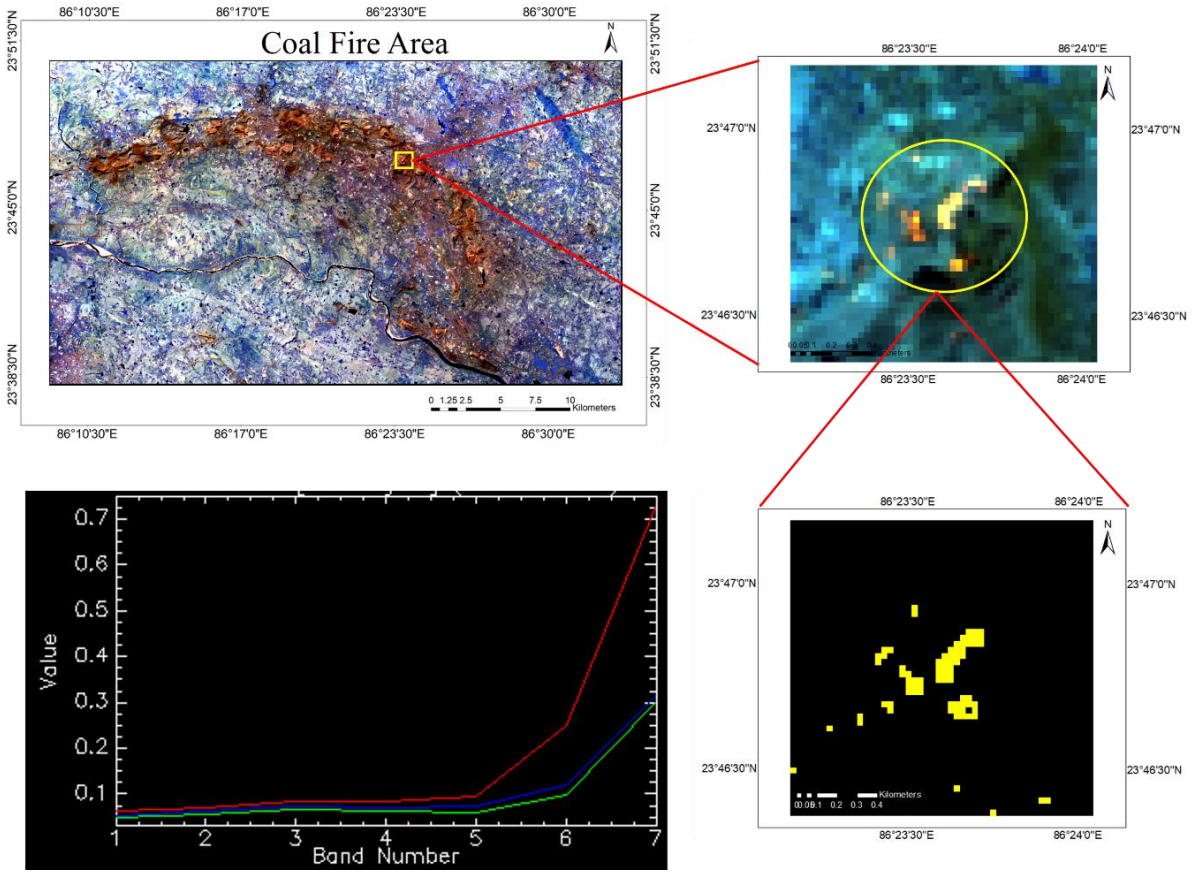

Figure 3.3. The Coal fire region in Jharia Coalfield. Upper left is the FCC composite of band 5, band 6 and band 7 of Landsat 8 OLI data. The pixels falling into the yellow circle of the upper right figure represents the fire affected pixels. The lower yellow pixels in lower right are extracted using the AFD (section 3.1). The pattern in the lower left figure depicts the spectral trend of surface reflectance of coal fire affected pixels.

As the trend between channels 5 to 7 in Landsat-8, exhibited a strictly increasing response, the corresponding ratios of I_1 and I_2 was set to greater than zero, the index I_1 was set to greater than I_2 in the third condition of Eq. (3.4).

After executing the Eq. (3.4) for channels 5, 6 and 7 in Landsat-8 data, the test successfully extracted a significant number of coal fire affected pixels which were underestimating after incorporating the AFD algorithm for the same data (Section 2.2.4). However, an additional number of pixels covered by riverbed and overburden materials (in context of surface mining, the overburden material appears as brown for the FCC composite of channel 5, 6 and 7 of Landsat 8 OLI data), were also extracted using Eq. (3.4). Therefore, another criterion was added to the Eq. (3.4) for distinguishing those pixels from the actual coal fire-affected pixels. The overall criteria can be integrated to:

$$I_1 = \frac{\rho_7 - \rho_6}{\rho_7 + \rho_6} > 0.0 \text{ AND } I_2 = \frac{\rho_6 - \rho_5}{\rho_6 + \rho_5} > 0.0 \text{ AND } I_1 > I_2 \text{ AND } I_3 = \frac{\rho_7 - \rho_5}{\rho_7 + \rho_5} > 0.25 \quad (3.5)$$

3.3. Modifications performed on STARFM and ESTARFM

3.3.1. Computation of weight for modified STARFM

The original STARFM used the concept of pixel vector in order to retrieve the spectrally similar homogeneous pixels from the moving window using Eq. (2.22). However, we proposed to treat each spectral channel (band 5, band 6 and band 7 of Landsat-8) separately for extracting similar pixels using the Eq. (2.22).

3.3.2. Computation of weight for modified ESTARFM

In reference to extracting the spectrally similar homogeneous pixels, instead of utilizing the concurrent use of three spectral channels together as pixel vectors (band 5, band 6 and band 7 of Landsat-8 sensor), each channel has been considered separately for extracting similar pixels. Furthermore, in the original algorithm, the Landsat scene from t_m and t_n were utilized to filter out the spectrally similar homogeneous pixel vectors and the vectors with locational similarity (each pair of pixel vectors encircled in blue within (A ∩ B) in Figure 3.4), were considered for computing the correlation coefficient in Eq. (2.42). However, we utilized the intersected as well as non-intersected portions from each date (Ai ∪ Bi, where i ∈ (1, 3), and i represents each individual spectral channel as in Figure 3.4) after splitting each of the pixel vectors, and creating 6 distinct sets depicted in Figure 3.4. Moreover, $A1 \cup B1$, $A2 \cup B2$, and $A3 \cup B3$ have been used to compute the correlation coefficient for band 5, band 6 and band 7 respectively (Figure 3.4).

Therefore, if M number of pixels are extracted from i^{th} band at date t_m and N number of pixels are shortlisted at the date t_n, the number of shortlisted pixels can be put to a single set:

$$S_n = \begin{cases} F_{nK} = \{F(x_{i1}, y_{j1}, t_n, B_i), \dots, F(x_{iN}, y_{jN}, t_n, B_i)\} \\ C_{nK} = \{C(x_{i1}, y_{i1}, t_n, B_i), \dots, C(x_{iN}, y_{iN}, t_n, B_i)\} \end{cases} \quad i \in (1, K) \vee t_k \in (t_m, t_n)$$

$$S_m = \begin{cases} F_{mK} = \{F(x_{i1}, y_{j1}, t_m, B_i), \dots, F(x_{iN}, y_{jN}, t_m, B_i)\} \\ C_{mK} = \{C(x_{i1}, y_{i1}, t_m, B_i), \dots, C(x_{iN}, y_{iN}, t_m, B_i)\} \end{cases} \quad i \in (1, K) \vee t_k \in (t_m, t_n)$$

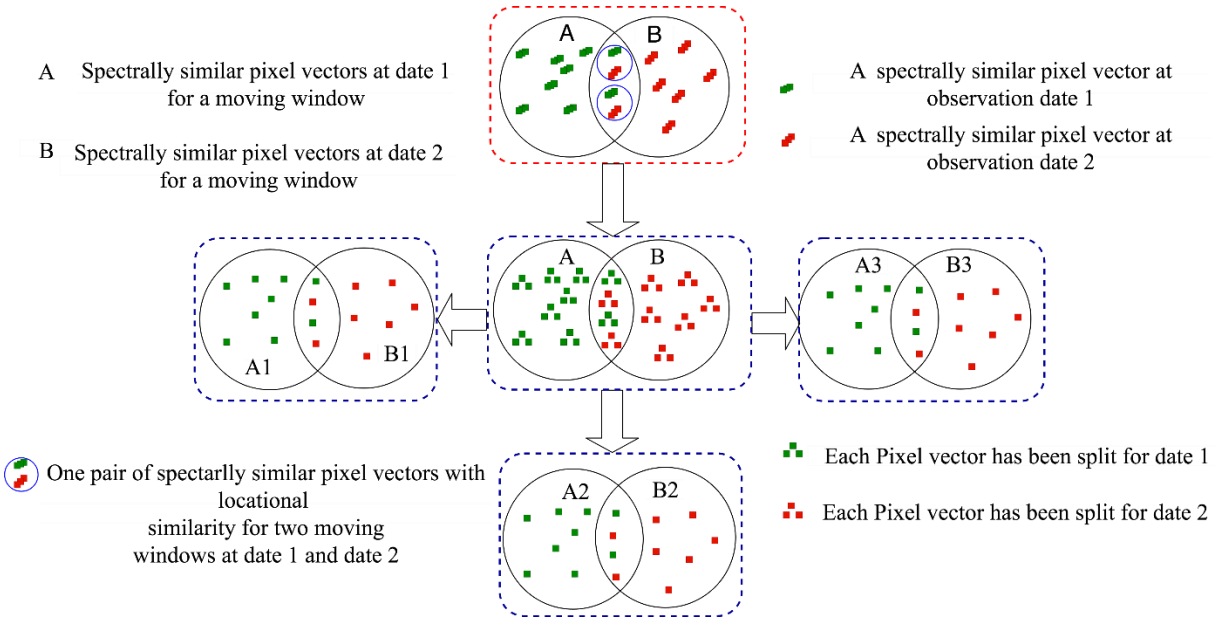

Figure 3.4. A and B denote the set of all spectrally similar pixel vectors for date 1 and date 2 in ESTARFM (encircled in red). In the original ESTARFM, each pair of spectrally similar pixel vectors (encircled in blue within A ∩ B) in the intersected portion with the locational similarity have been considered for estimating the correlation coefficient in Eq. (2.44). However, in the modified ESTARFM, all the spectrally similar pixel vectors have been split into three component, and corresponding 6 sets (A1 ∪ B1 for band 5; A2 ∪ B2 for band 6; A3 ∪ B3 for band 7 in Landsat 8 OLI data) are established. The Ai ∪ Bi, i ∈ (1, 3), has been considered for estimating the correlation coefficient for individual pixels.

Where S_m and S_n denote set of the similar pixels extracted from fine resolution pixels and corresponding coarse resolution pixels, and F_{mK}, F_{nK}, denote the set of all similar pixels extracted from a moving window of actual Landsat images at t_m and t_n respectively, and C_{mK}, C_{nK} denotes the pixels (resampled coarse resolution pixels at t_m and t_n for VIIRS) correspond to a similar location of the pixels in F_{mK}, F_{nK} respectively. If F_{nK} and F_{mK} as well as C_{nK} and C_{mK} are combined, the distinct sets can be written in form of:

$$F_{(m+n)K} = \{F(x_{i1}, y_{j1}, t_m, B_i), \dots, F(x_{iM}, y_{jM}, t_m, B_i), \dots, F(x_{i1}, y_{j1}, t_n, B_i), \dots, F(x_{iN}, y_{jN}, t_n, B_i)\}$$

AND

$$C_{(m+n)K} = \{C(x_{i1}, y_{j1}, t_m, B_i), \dots, C(x_{iM}, y_{jM}, t_m, B_i), \dots, C(x_{i1}, y_{j1}, t_n, B_i), \dots, C(x_{iN}, y_{jN}, t_n, B_i)\}$$

The $F_{(m+n)K}$ corresponds to $(Ai \cup Bi)$ for i^{th} spectral channel of the high-resolution image in Figure 3.4. Also, $C_{(m+n)K}$ corresponds to set of similar pixels (extracted from resampled coarse resolution pixels) with locational similarity for fine resolution similar pixels in $F_{(m+n)K}$.

Therefore, the corresponding correlation coefficient of similar pixels can be written as:

$$R_L = \frac{E\left[\left(F_L - E(F_{(m+n)K})\right)\left(C_L - E(C_{(m+n)K})\right)\right]}{\sqrt{V(F_{(m+n)K}) \times V(C_{(m+n)K})}}, \qquad L \in \{1, (M+N)\} \tag{3.6}$$

Where,
L – The total number of pixels from a moving window at t_m and t_n,
$E(F_{(m+n)K}), E(C_{(m+n)K}) -$ Mean of all the similar pixels extracted from moving windows at t_m and t_n
$V(F_{(m+n)K}), V(C_{(m+n)K}) -$ Variance of the similar pixels extracted from moving windows at t_m and t_n
$F_L, C_L -$ is the L^{th} fine resolution pixel from the set $F_{(m+n)K}$ and $C_{(m+n)K}$ respectively
$(M + N)$ – The total number of similar pixels extracted from fine resolution Landsat images at t_m and t_n

Utilizing the value of R_L, the corresponding weights are estimated in Eq. (2.45). Therefore, the subsequent tests are repeated distinctly using NIR, SWIR1 and SWIR2 channels of both VIIRS and Landsat 8 OLI data.

3.4. Qualitative and quantitative assessment of the fusion methods

The quantitative and qualitative assessments are carried out to check the feasibility of a fused product for miscellaneous applications in remote sensing. The qualitative assessments are performed based on visual interpretations to assess that the rate of change of phenology from the observed and predicted date are captured accurately or not. Furthermore, the similarity of spatial pattern in phenology between the observed and predicted date is assessed for its consistency with the actual product. On the other hand, quantitative assessments are performed using several assessment metrics.

3.4.1. Root Mean Square Error (RMSE)

In this study, the quantitative assessments of fused products are carried out by estimating the root mean square error between the synthetically predicted images with the actual images of Landsat 8 OLI data. Therefore, it can be formulated as:

$$\mathrm{RMSE} = \sqrt{\frac{\sum_{i=1}^{N}(x_i - y_i)^2}{N}} \tag{3.7}$$

Where x_i and y_i denote the corresponding surface reflectance value of i^{th} pixel in the actual and predicted image respectively, and N denotes the total number of pixels in the actual and synthetic image, the similar date of prediction and date of acquisition of the actual scene.

3.4.2. Absolute Average Difference (AAD)

The AAD can be estimated for the actual and predicted image of Landsat 8 OLI data. It also indicates the biases of synthetic product. It can be written as:

$$\mathrm{AAD} = \frac{\sum_{i=1}^{N}|x_i - y_i|}{N} \tag{3.8}$$

3.4.3. Correlation Coefficient (CC)

The CC is a measure of linear correlation between two Random variables X and Y. In this study, if the set of actual values (Landsat image) are assigned to the random variable of X, and the set of predicted values (synthetic Landsat image) are assigned to another random variable Y, the formula can be depicted as:

$$\rho_{X,Y} = \frac{E[(X - \mu_X)(Y - \mu_Y)]}{\sigma_X \sigma_Y} \tag{3.9}$$

Where,

$\rho_{X,Y}$ - Correlation coefficient and the value ranges from -1 to +1. +1 indicates a total positive correlation, -1 denotes a negative correlation and 0 indicates no correlation,

μ_X, μ_Y - Mean of X, Y respectively,

σ_X, σ_Y - Standard deviation of X, Y respectively,

E - Expectation.

3.4.4. The ErreurRelative Globale Adimensionnelle de Synthèse (ERGAS)

The index ERGAS is the measure of similarity between the reference and fused image (Xue et al., 2017). It also considers the number of bands employed for spatiotemporal fusion. The index can be formulated as:

$$ERGAS = 100\frac{h}{l}\sqrt{\frac{1}{N_{ban}}\sum_{k=1}^{N_{ban}}\left({RMSE_k}/{M_k}\right)^2} \tag{3.10}$$

Where,

H - Spatial resolution of fine resolution image (Landsat 8 OLI),

l - Spatial resolution of coarse resolution image (VIIRS),

M_k - Mean of the k^{th} band employed for fusion,

N_{ban} - Number of bands employed for spatiotemporal fusions

Considering the ideal cases, if the channel-specific $RMSE$ values are zero, the estimated value of $ERGAS$ should be zero.

3.5. Assessment metrics for evaluating the performance of synthetic coal fire product:

The NRAFD method was applied to the synthetic products derived from several spatiotemporal fusion methods, with a view to delineating the surface coal fire affected pixels from its background. Consequently, the quantitative and qualitative assessments of the coal fire products derived from the synthetic images are carried out with several matrices. A brief overview of different metrics is illustrated below.

3.5.1. True Positive Rate (TPR)

The TPR is the ratio of true positive (TP) with the summation of true positive (TP) and false negative (FN). The equation can be depicted as:

$$TPR = \frac{TP}{TP + FN} \tag{3.11}$$

In this study, the synthetic Landsat composites were classified as coal fire (surface coal fire) and non-coal fire region by incorporating the NRAFD method. Later on, the binary classified image was assessed through these metrics. A lower value of FN in Eq. (3.11) represents the higher TPR.

3.5.2. Positive Predictive Value (PPV)

The PPV is the ratio of the true positive (FP) with the summation of true positive (FP) and false positive (FP). PPV can be written as:

$$\mathrm{PPV} = \frac{\mathrm{TP}}{\mathrm{TP} + \mathrm{FP}} \tag{3.12}$$

A lower value of FP in Eq. (3.12) represents the higher value of PPV. The PPV ranges from 0 to 1. 0 designates the highest quality in terms of precision of a statistical test. On the other hand, 1 designates the lowest quality.

3.5.3. F_1 Score

F_1 score denotes the accuracy of the test in statistical analysis (binary classification) and is estimated by taking the harmonic mean of TPR and PPV. The $\mathrm{F_1}$ score can be written as:

$$\mathrm{F_1} = \left(\frac{\mathrm{TPR}^{-1} + \mathrm{PPV}^{-1}}{2}\right)^{-1} \tag{3.13}$$

The value of $\mathrm{F_1}$ score ranges from 0 to 1. '0' represents the worst quality and '1' designates the highest quality in terms of a statistical test.

3.5.4. Matthews Correlation Coefficient (MCC)

The MCC is the estimate of assessing the quality of binary classifications. It is primarily used in machine learning approaches. It takes into account the value of true positives, false positives, true negatives, and false negatives. Also, the coefficient is independent of the size of the classes (Matthews, 1975). It can be depicted as:

$$\mathrm{MCC} = \frac{\mathrm{TP} \times \mathrm{TN} - \mathrm{FP} \times \mathrm{FN}}{\sqrt{(\mathrm{TP} + \mathrm{FP})(\mathrm{TP} + \mathrm{FN})(\mathrm{TN} + \mathrm{FP})(\mathrm{TN} + \mathrm{FN})}} \tag{3.14}$$

Where,
TP – true positive, TN – true negative, FP – false positive, FN – false negative

3.5.5. Coal Fire Product Quality Index (CFPQI)

In order to address the combined effect of F_1 Score and MCC, the harmonic mean of MCC, TPR and PPV have been considered to designate as a quality of the end product. Here, the harmonic mean addresses the sensitivity of the MCC more effectively than simple arithmetic mean (e.g., if the prediction accuracy of $\mathrm{F_1}$score and accuracy is higher, doesn't necessarily indicate a higher value in MCC. Therefore, it can be written as:

$$\mathrm{CFPQI} = \left(\frac{\mathrm{TPR}^{-1} + \mathrm{PPV}^{-1} + \mathrm{MCC}^{-1}}{3}\right)^{-1} \tag{3.15}$$

Theoretically, the highest values of TPR, PPV and MCC should be 1. Consequently, the CFPQI holds the highest possible value of 1. Therefore, the CFPQI ranges from 0 to 1. '0' indicates the lowest quality product. On the other hand, '1' indicates the highest quality of the product.

4. STUDY AREA AND DATASETS

4.1. Study Area

The Jharia coalfield is primarily known for its robust industrialized zone with the richness of high-grade coking coal. With an estimated reserve of 19 million tons, Jharia coalfield is also known for its highest coal resources in India. The location and spatial extent is about 1150 km southeast of Delhi and 250 km northeast of Calcutta with 23°38′ N to 23°51′ N latitude and 86°07′ E to 86°30′ E longitude with a spatial coverage of 280 km². The activity of coal mining initiated during the year of 1984 and the first fire was detected in the year of 1916. The topographic elevation ranges from 150 m to 300 m above mean sea level. Furthermore, 70 major surface and subsurface fires were reported after the nationalisation of the coal industry. The location and spatial extent of the Jharia coalfield have been depicted in Figure 4.1.

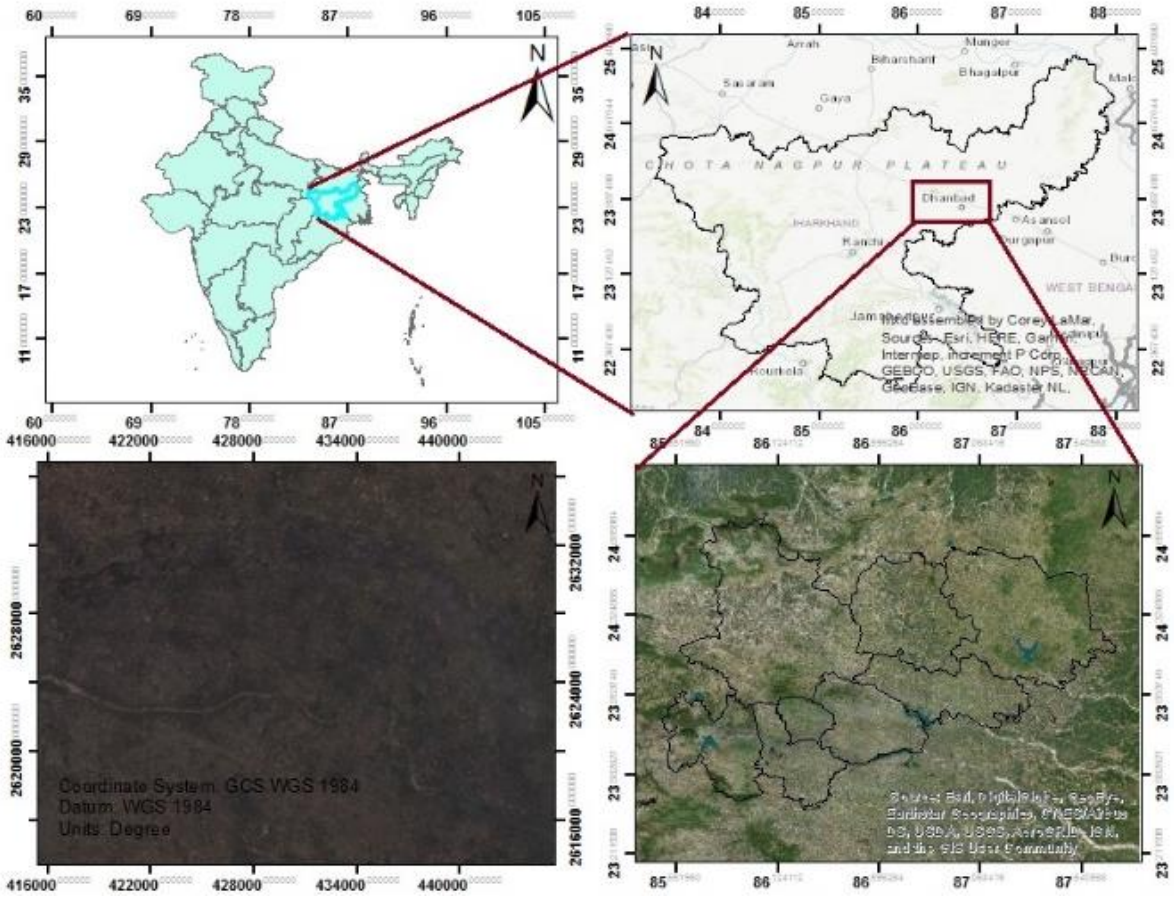

Figure 4.1. The location and spatial extent of Jharia coalfield

A significant amount of research activities have been carried out over the last few decades over the surface and subsurface fire of Jharia coalfield using the application of thermal as well as shortwave infrared remote sensing (Bhattacharya & Reddy, 1994; Bhattacharya et al., 1991; Chatterjee, 2006; Cracknell & Mansor, 1993; Gupta, Mohanty, Kumar, & Banerjee, 2014; Mishra, Bahuguna, & Singh, 2011; T. K. Mukherjee, Bandyopadhyay, & Pande, 1991; Prakash & Gupta, 1998; Prakash et al., 1995; Saraf, Prakash, Sengupta, & Gupta, 1995). The southeast part of the coalfield is covered by Damodar River. The dynamics of land surface have been changing which led to serious environmental degradation due to severe issues associated with coal fire. Consequently, the people who use to live within the close proximity of coal fire-affected areas, are majorly affected and several accidents have occurred. Therefore, the chosen

study area needs to be researched for the systematic detection and monitoring of coal fire (Kuenzer, Hecker, Zhang, Wessling, & Wagner, 2008).

4.2. Dataset extraction and preprocessing

4.2.1. LANDSAT 8 OLI/TIRS

The Landsat 8 OLI surface reflectance product (level 2 atmospherically corrected and terrain corrected) with product identity has been depicted below.

Table 4.1 The Landsat 8 OLI surface reflectance product with the product ID

Landsat 8 OLI (product ID)	Date of Acquisition
"LC08_L1TP_140043_20171224_20180103_01_T1"	December 24, 2017
"LC08_L1TP_140043_20180109_20180119_01_T1"	January 9, 2018

Preprocessing

The Landsat 8 OLI surface reflectance product was manually cropped to the region which is covered by the major coalfield areas. The location and spatial extent of the cropped area was 413130.0 m (upper left – axis x) to 453990.0 m (lower right – axis x) with 2637330.0 m (upper right – axis y) to 2614110.0 m (lower right – axis y) with a projection system of WGS 84, UTM 45, North. The dimension of the cropped image was 775 rows × 1363 columns with a spatial coverage ≈ 950.69 km² ((a) in Figure 4.2).

4.2.2. VIIRS

The VIIRS surface reflectance product (VNP09GA) with product identity is shown in Table 3.2.

Table 4.2: The VIIRS surface reflectance product which is used for spatiotemporal fusion

VIIRS (product ID)	Date of Acquisition
"VNP09GA.A2017358.h25v06.001.2017360195442.h5"	December 24, 2017
"VNP09GA.A2018010.h25v06.001.2018011100233.h5"	January 9, 2018
"VNP09GA.A2018025.h25v06.001.2018026084420.h5"	January 25, 2018

Preprocessing

The preprocessing included the re-projection and resampling of VIIRS surface reflectance product (VNP09GA).

1. The HDF-EOS to GeoTIFF conversion tool (HEG) has been used to re-project the VIIRS data from sinusoidal to UTM, WGS84 (45 North) projection system with a spatial resolution of 463.0 m for **I** band and 927.0 m for **M** band (Taaheri, 2018).

2. After reprojection, the resampling of VIIRS data has been performed by incorporating the nearest neighbour and bilinear resampling method to resample the 463.0 m resolution **I** band and 927.0 m resolution **M** band to 30.0 m resolution.
3. The region was manually cropped to the similar spatial extent of the subset in Landsat 8 OLI.

Table 4.3: Input dataset and the associated spectral range used for spatiotemporal fusion methods for generating synthetic Landsat like images and the date of acquisition of Landsat 8 OLI and VIIRS scene.

Input Dataset	Spectral range (1) (NIR)	Spectral range (2) (SWIR1)	Spectral range (3) (SWIR2)	Acquisition date
Landsat 8 OLI	B5 (0.85 – 0.88 μm)	B6 (1.56 – 1.65 μm)	B7 (2.08 – 2.35 μm)	December 24, 2017
VIIRS1	I2 (0.85 – 0.88 μm)	I3 (1.55 – 1.75 μm)	M11 (2.23 – 2.28 μm)	January 9, 2018
VIIRS2	I2 (0.85 – 0.88 μm)	I3 (1.55 – 1.75 μm)	M11 (2.23 – 2.28 μm)	January 25, 2018

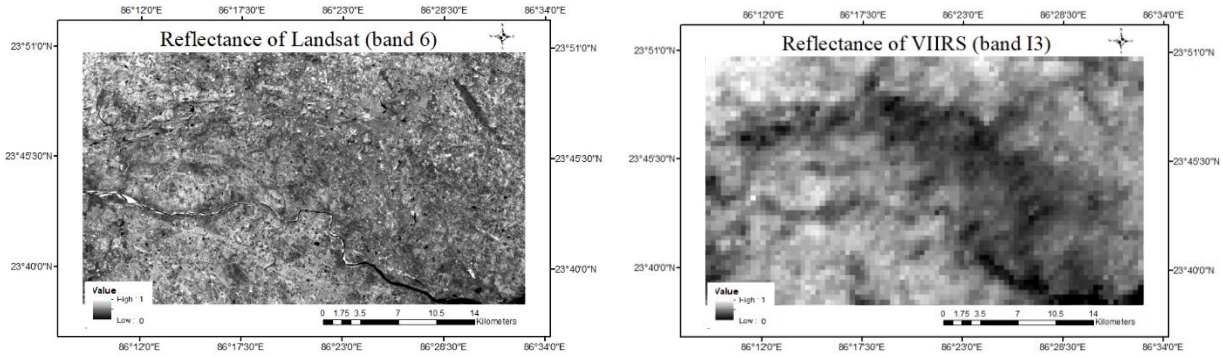

(a) (b)

Figure 4.2. The surface reflectance of band 6 in Landsat 8 OLI composite (Date – December 24, 2017), (b) – the surface reflectance of channel I3 in VIIRS composite (Date – December 24, 2017).

4.3. Sensor characteristics

The different specifications of Landsat 8 and VIIRS sensors have been depicted in respect of distinct characteristics associated with the spatial, temporal, spectral resolution, and corresponding scanning width.

Table 4.4 The distinct sensor characteristics

Specifications	Landsat 8 OLI / TIRS	VIIRS
Spatial Resolution	30.0 m	375.0 m, 750.0 m
Spectral Resolution	8 Bands	21 Bands
Temporal Resolution	16 days	Daily
Scanning width	170 km × 185 km	3040 km × 12 km

4.4. Description of products

4.4.1. Dataset description (Landsat 8 OLI)

The standard terrain and atmospherically corrected surface reflectance products (Level 2) of Landsat 8 OLI / TIRS sensors are generated by Landsat Surface Reflectance Code (LaSRC) which incorporates the aerosol inversion test using coastal aerosol band, uses climate data from MODIS as well as implement a unique radiative transfer model (U.S Geological Survey, 2018).

4.4.2. Dataset description (VIIRS)

The VIIRS observation includes 375.0 m spatial resolution for Imagery Resolution band (**I**) and 750.0 m spatial resolution of moderate resolution band (**M**). The NPP/VIIRS surface reflectance products (VNP09GA) are generated using VIIRS top-of-atmospheric reflectance, VIIRS visible band, cloud mask and atmospheric parameters as input. The generated product is further resampled to 463.0 m for I1-I3 bands and 927.0 m for M1-M8 and M10-M13 by incorporating the unique pixel aggregation scheme. Moreover, the products are gridded to 10 km × 10 km frame using sinusoidal projection (EARTHDATA, 2019).

4.5. Software used

All the methods have been applied and implemented in a python environment (Python 3.7). In carrying out preprocessing, ERDAS IMAGINE 2016 and ENVI 5.3 CLASSIC have been used. For the generation of maps, ArcMap 3.1 has been used.

5. RESULTS AND ANALYSIS

This chapter depicts the results achieved by incorporating the following methods in Section 3.1, which are aligning with the specific objectives. **Section 5.1** depicts the results achieved for different coal fire detection methods and associated comparative analysis. **Section 5.2** reports the results achieved by incorporating different spatiotemporal fusion methods and comparative analysis between them. S**ection 5.3** illustrates the performance evaluation of a novel coal fire detection method (NRAFD) on synthetic Landsat images with the actual Landsat image using various coal fire detection methods explored in this research.

5.1. Comparative analysis between AFD and NRAFD

5.1.1. Results of AFD

The active fire detection method was performed by using the Landsat 8 OLI data on January 9, 2018, as an input. The initial test sequence using Eq. (2.8), extracted 92 pixels with the spatial coverage ≈ 0.08 km^2. The extracted pixels are defined as potentially ambiguous fire affected pixels. After that, the second test utilising Eq. (2.9), was conducted to detect the highly energetic fires often leading to DN folding in channel 7 of Landsat 8 OLI data. However, no pixels were shortlisted after executing the test. Furthermore, the thresholds in Eq. (2.8), were relaxed in Eq. (2.10), in order to select a significant number of candidate pixels for subsequent analysis. The test using the Eq. (2.10), extracted 292 pixels with a spatial converge ≈ 0.26 km^2. Furthermore, the shortlisted candidate pixels (equation 3.3) were passed through a fixed threshold along with the contextual criteria in Eq. (2.11). After concurrent execution of all the test sequences, 198 pixels (spatial coverage ≈ 0.18 km^2) were delineated as potentially unambiguous fire affected pixels.

In this study area, a visual inspection was carried out to check the associated ambiguities between the coal fires affected pixels and the pixels covered by water bodies and shadows. However, such ambiguity didn't exist for the chosen study area. Even though the AFD method was able to delineate a significant number of fire-affected pixels, it was underestimating for some of the fire affected regions as depicted in Figure 5.1. From (a2) vs (b2) and (a4) vs (b4) in Figure 5.1, the method was unable to extract an additional number of fire affected pixels which were also appearing as yellowish red (encircled in yellow in Figure 5.1) typically depicting the fire-affected pixels with low intensity.

5.1.2. Results of NRAFD

The improved criteria detected an additional number of fire affected pixels. In the original AFD, the test sequences specified in Section 5.1.1, extracted 198 number of pixels (spatial coverage ≈ 0.18 km^2). However, the improved criteria in Eq. (3.5), detected 630 number of fire affected pixels (spatial coverage ≈ 0.50 km^2) with an overlap of 190 pixels (spatial coverage ≈ 0.17 km^2) in reference to the pixels extracted by AFD. Therefore, the overlapping regions between these two algorithms were 95 % (190 / 198) considering the fidelity of AFD. Moreover, the pixels underestimating in AFD was successfully extracted by NRAFD (marked in yellow circle in a(2) vs (c2) and (a4) vs (c4) in Figure 5.1). Furthermore, it was observed that for some of the regions which were within the close proximity of active fire, hold a probability of being a mixed pixel (colours ranging between brown to brownish red). For those pixels (mixed), the NRAFD method led to overestimation or underestimation for some of regions. The quantitative assessments of those pixels were ceased due to the unavailability of reference coal fire map for the entire coalfield. Furthermore, there might be some errors associated with the systematic visual

inspection between the location of actual fire pixels in FCC composite (channel 5, 6 and 7 of Landsat-8) and the location of pixels belonging to coal fire (in form of a binary image).

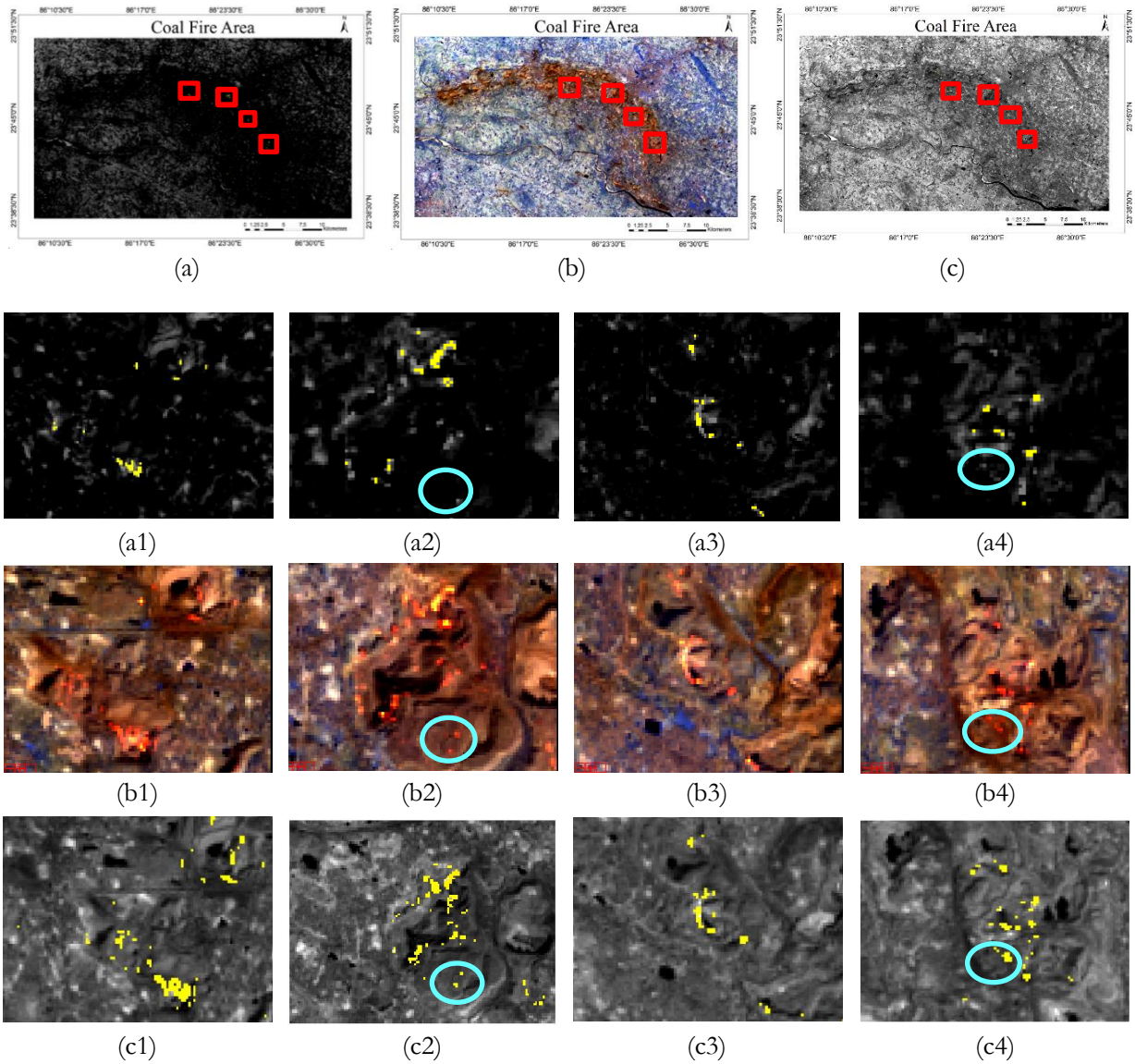

Figure 5.1. (a) The detected coal fire pixels are marked in yellow for the chosen study area using AFD executed on Landsat-8 OLI (acquisition date – January 9, 2018). (b) FCC composite of channel 5, 6 and 7 of Landsat 8 OLI data where the fire affected pixels are appearing as yellow/yellowish red. (a1 – a4) corresponds to the similar location in (b1 – b4) and (c1 - c4). (c) The detected coal fire pixels are marked in yellow for the chosen study area using NRAFD.

The NRAFD method was tested for 24 cloud-free scenes of actual Landsat-8 data from January 2014 to January 2018 for the same study area. As the method was successful in extracting the coal fire affected pixels for all the scenes, the NRADF was chosen as a reference method in terms of generating synthetic coal fire products as reported in Section 5.2.

5.2. Results of spatiotemporal fusion methods

5.2.1. Comparative analysis between STARFM and modified STARFM

The STARFM was implemented as well as executed in a python environment. The corresponding spectral domains which were matching successively for Landsat 8 OLI and VIIRS, used to generate synthetic Landsat like images (Table 4.3). As the Landsat-8 sensor has a repeat cycle of 16 days, the single pair of VIIRS at December 24, 2017 and January 9, 2018 with the actual Landsat data on December 24, 2017, were used to generate the synthetic Landsat data on January 9, 2018 over the spectral channel of NIR, SWIR1 and SWIR2. We selected 1410 m × 1410 m as moving window which is approximately 3 × 3 VIIRS 463.0 m resolution pixel (**I** band) or approximately 47 × 47 Landsat-8 30-m resolution pixel. Also, we utilized the similar window size for fusing M11 band (spatial resolution 927.0 m, and resampled to the 30.0 resolution using bilinear resampling method; SWIR2 region) of VIIRS data with the band 7 (spatial resolution 30.0 m, SWIR2 region) of Landsat-8 OLI data. The number of classes was set as 10 in Eq. (2.22). In order to select a spectrally similar homogeneous pixel vector, the condition in Eq. (2.22) had to be passed 3 times as the dimension of the pixel vector was 3 × 1 (NIR, SWIR1 and SWIR2 in Landsat-8). After that, the weighting function in Eq. (2.28) was used for predicting the surface reflectance in the central pixel of a moving window. The land cover type was homogeneous for the regions where the overburden materials from the surface mining operations appeared as small brownish contours, however, for most of the surface type, the phenology was heterogeneous. Also, the very large patches of similar surface types were lesser in the chosen study area. Due to that, a pure coarse resolution homogenous pixel from VIIRS data might not be found. Generally, STARFM performs better if there exist homogeneous pixels in low-resolution VIIRS data. On the other hand, for modified STARFM, the distinct channels are considered for extracting similar pixels (for example, while predicting the reflectance in NIR channel, the other channels such as SWIR1 and SWIR2 was not considered as described in Section 3.3.1). It was done to extract the additional number of similar pixels for estimating the reflectance using the weight function depicted in Eq. (2.28).

Figure 5.2 (a), (b) and (c), shows the synthetic FCC composite (band 5, 6 and 7) of actual Landsat-8 data (a), predicted Landsat-8 using STARFM (b), and predicted Landsat-8 (c) by incorporating the modified STARFM respectively. It was observed that the FCC composite between actual and predicted images are comparable, and exhibit spectral similarities between different phenology. Also, it was found (within the zoomed window in (a), (b) and (c) in Figure 5.2) that the brightness of the few coal fire affected pixels (from yellow to yellowish red) got reduced for the synthetically predicted images. Moreover, the channel specific scatterplots between the actual and predicted Landsat image for STARFM (ab1 - ab3 in Figure 5.2) and modified STARFM (ac1 – ac3 in Figure 5.2), depict a strong correspondence with the actual Landsat image. For both of these methods, the number of outliers was comparatively less for band 5 (ab1 in Figure 5.2) and band 6 (ab2 in Figure 5.2). However, for band 7, the number of outliers was slightly higher for both of these methods (ab3 vs ac3 in Figure 5.2). The synthetically generated products using these two methods on January 9, 2018, were assessed quantitatively with the actual Landsat image on the same date by estimating several metrics (Table 5.1). The RMSE and AAD were approximately similar for the corresponding synthetic channels (using STARFM and modified STARFM) with the actual channels of Landsat 8. However, from the Table 5.1, the CC is slightly higher for each channel of synthetic product derived from the actual STARFM in reference to the modified STARFM (NIR band: 0.960 vs 0.958; SWIR1 band: 0.972 vs 0.971; SWIR2 band: 0.961 vs 0.959). Moreover, the value of ERGAS was lower (0.511 in Table 5.1) compared to modified STARFM. As it was known that the lower the value of ERGAS, the better the quality of fusion (Xue et al., 2017). Therefore, the spectral similarity was higher for the fused products derived from STARFM in respect of modified STARFM, with the reference image in January 9, 2018.

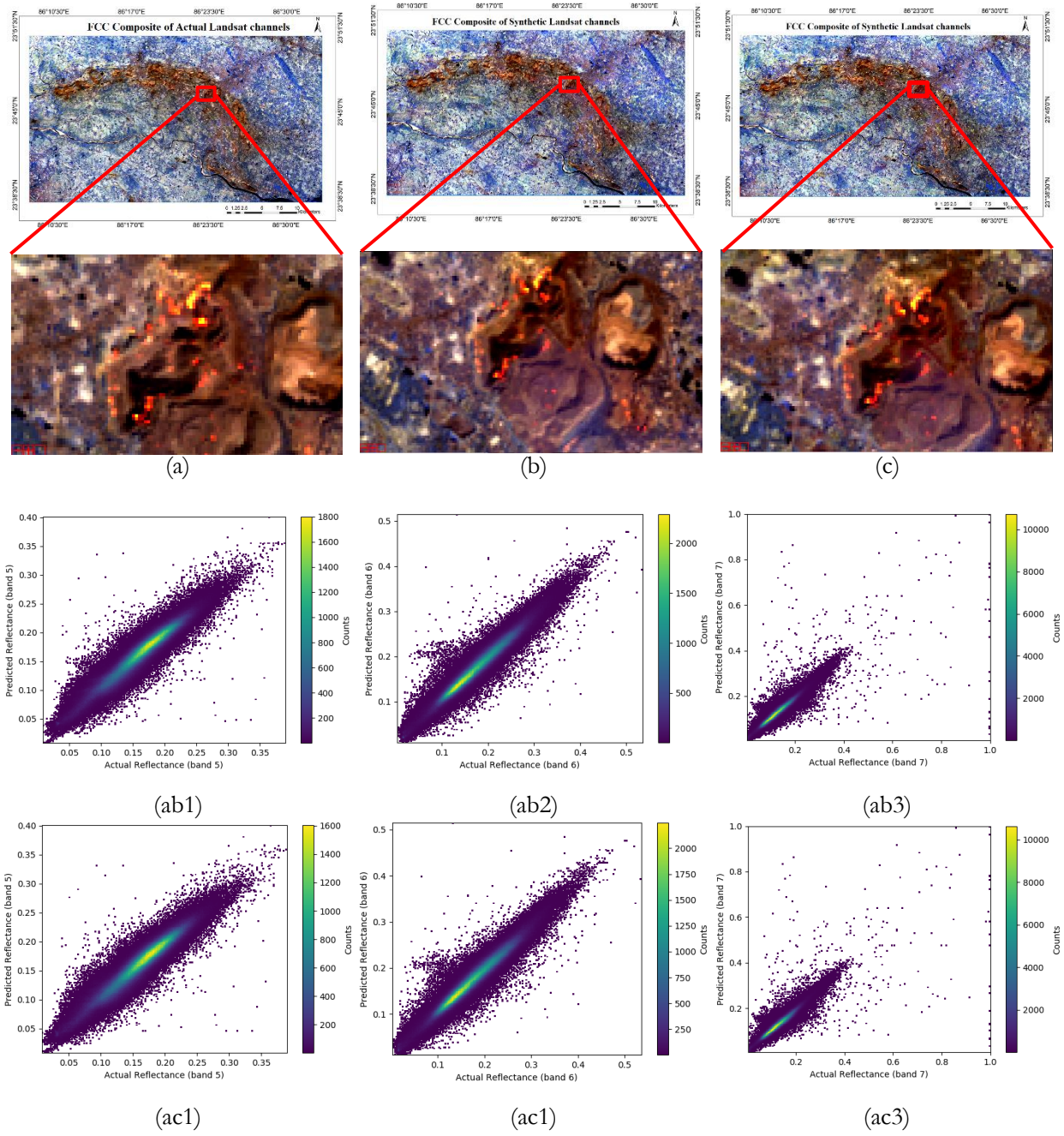

Figure 5.2 (a) The FCC composite of actual Landsat-8 image using band 5, band 6 and band 7 on January 9, 2018. (b) FCC composite of synthetic Landsat-8 images using similar channels on January 9, 2018 by incorporating STARFM. (c) FCC composite of synthetic Landsat-8 images using similar channels by incorporating Modified – STARFM. (ab1-ab3) depicts the scatterplots between the actual (a) and synthetic Landsat image (b) for band 5 (ab1), band 6 (ab2) and band 6(ab3) respectively. (ac1 – ac3) depicts the scatterplots between the actual (a) and predicted (c) Landsat image for channel 5 (ac1), channel 6 (ac2) and channel 7 (ac3) respectively.

5.2.2. Comparative Analysis between ESTARFM and modified ESTARFM

The ESTARFM and modified ESTARFM were implemented and executed in a python environment using the two pairs of Landsat and VIIRS acquired at 24 December 2017 (1st observation date) and 25 January 2018 (2nd observation date) and another VIIRS data on January 9, 2018 (prediction date). After successfully implementing both methods, synthetic Landsat like products were generated on January 9, 2018. The similar spectral channels (Table 4.3), between Landsat-8 and VIIRS, were incorporated for the aforementioned spatiotemporal fusion methods. We selected the moving window size as 47 × 47, using a similar principle as depicted for STARFM and modified STARFM in Section 5.2.1. Also, a similar number of classes was set in Eq. (2.22). In case of ESTARFM, the spectrally similar homogeneous pixel vectors were extracted from the band 5, band 6 and band 7 of actual Landsat 8 OLI data on December 24, 2017, and January 25, 2018. Also, the pixel vectors (band 5, 6 and 7) satisfying the criterion in Eq. (2.22), for two aforementioned observed dates with a locational similarity within the corresponding moving windows, were extracted for estimating the corresponding weight and conversion coefficient to predict the reflectance of the central pixel. It was observed that, to select a spectrally similar pixel vector, the criterion in Eq. (2.22), had to be passed for 6 times consecutively (3 times for 3 spectral channels on the 1st observed date – 24/12/2017 and 3 times for 3 channels on the 2nd observed date 2 – 25/01/2018). Due to that, the number of shortlisted spectrally similar pixel vectors from the moving windows were relatively lower as the homogeneous patches with larger size were comparatively lesser for the chosen study area. As a result, the computation of the correlation coefficient in Eq. (2.42), for estimating corresponding weights in Eq. (2.45), were leading to underestimation or overestimation for some of the pixels. For a similar reason, the conversion coefficient which was estimated by the slope derived from the regression line, leading to the erroneous prediction of surface reflectance for some of the pixels. Due to these uncertainties, the artifacts appeared while predicting the reflectance of the central pixel for a few of the moving windows (Figure 5.3 (b), a product derived by incorporating the ESTARFM).

Figure 5.3 shows the synthetic FCC composite (band 5, 6 and 7) of actual Landsat-8 data (a), predicted Landsat-8 using ESTARFM (b), and predicted Landsat-8 (c) by incorporating the modified ESTARFM respectively. In order to overcome the artifacts associated with the synthetic Landsat-8 products (encircled yellow in zoomed view of Figure 5.3 (b)), the ESTARFM was modified to improve the quality further. Instead of using 3 spectral channels together as in original ESTARFM, we proposed to utilize the channel-specific retrieval of similar pixels within each spectral range separately (Section 3.3.2). Consequently, the effects of artifact were significantly reduced, and as a result, the actual FCC composite and predicted FCC composite over the similar region in Figure 5.3 (a) and (c), respectively, exhibited spectral similarities between different phenology. Moreover, the channel specific scatterplots between the actual and predicted Landsat image for ESTARFM (ab1 - ab3 in Figure 5.3) and modified ESTARFM (ac1 – ac3 in Figure 5.3), depicted that the significant number of outliers were removed for band 5 and band 6 in modified ESTARFM (ac1 – ac2 in Figure 5.3). Also, the scatterplots (ab3; ac3 in Figure 5.3) illustrated the linear relationship and depicted a strong correlation between the two. Table 5.1 depicts the quantitative assessment of the prediction error between various spatiotemporal fusion methods. It was observed that the performance of modified ESTARFM was slightly higher than the ESTARFM in respect of AAD. (AAD values – NIR band: 0.010 vs 0.006; SWIR1 band: 0.012 vs 0.007; SWIR2 band: 0.006 vs 0.006). Moreover, the estimated RMSE was relatively lower for modified ESTARFM in reference to other spatiotemporal fusion methods (Table 5.1). The correlation coefficients of band 5, band 6 and band 7, were relatively higher for modified ESTARM in respect of other spatiotemporal fusion methods depicted in Table 5.1. Furthermore, the estimated ERGAS was minimum (0.401 for modified ESTARFM as in Table 5.1) in comparison to other spatiotemporal fusion methods. Also, the change of phenology was comparable during the short period. Moreover, all the spatiotemporal fusion methods depicted a strong

correspondence qualitatively and quantitatively with each other. As a whole, the modified ESTARFM outperformed all other fusion methods in terms of assessment metrics.

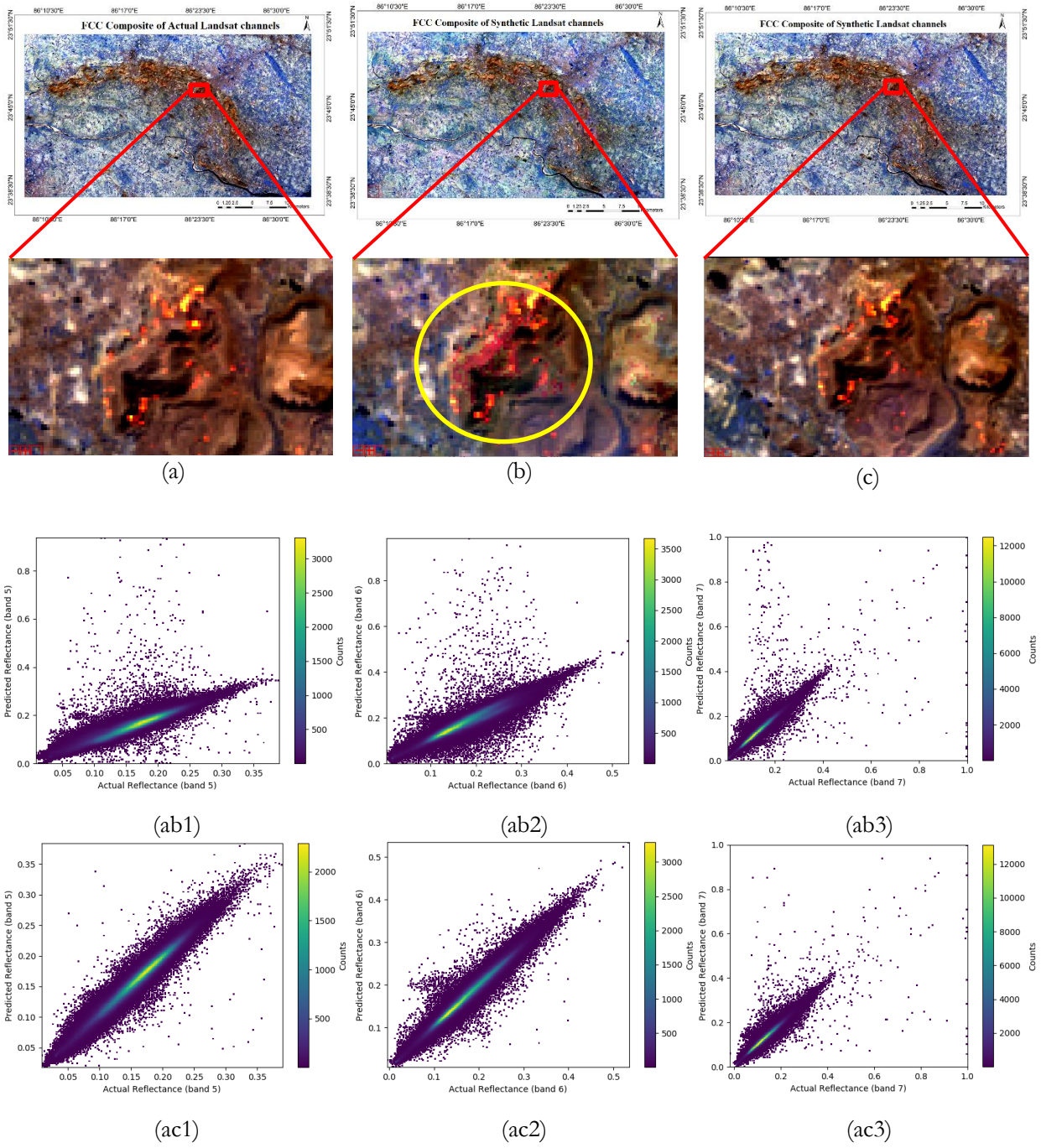

Figure 5.3. (a) The Landsat-8 FCC composite image using band 5, band 6 and band 7 on January 9, 2018. (b) FCC composite of synthetic Landsat-8 images using similar channels on January 9, 2018 by incorporating ESTARFM. (c) FCC composite of synthetic Landsat-8 images using similar channels by incorporating Modified – ESTARFM. (ab1 - ab3) depicts the scatterplots between the actual (a) and synthetic Landsat image (b) for band 5 (ab1), band 6 (ab2) and band 6 (ab3) respectively for ESTARFM. (ac1 – ac3) depicts the scatterplots between the actual (a) and predicted (c) Landsat image for channel 5 (ac1), channel 6 (ac2) and channel 7 (ac3) respectively for modified ESTARFM.

5.2.3. Overall comparative analysis between various spatiotemporal fusion methods

In respect to evaluating the performance quantitatively, the modified ESTARFM outperformed all other spatiotemporal fusion methods which were explored in this study (Table 5.1). As per visual inspection, the spectral similarities were closer to the reference image for the products derived from the various spatiotemporal fusion methods except for ESTARFM (artifacts encircled in yellow for (b) in Figure 5.3), on January 9, 2018. Also, the quantitative metrics such as RMSE, AAD were relatively lower compared to other fusion methods, in all the spectral channels employed for the fusion techniques. From the Table , the correlation coefficients between the actual and fused images for different spectral channels using modified ESTRAFM, were slightly higher than those derived from STARFM (NIR band: 0.960 vs 0.979; SWIR1 band: 0.972 vs 0.983; SWIR2 band: 0.961 vs 0.974). Also, the value of ERGAS was relatively lower for modified ESTARFM in reference to other fusion approaches.

Table 5.1. The performance evaluation of various spatiotemporal fusion methods (within each spectral domain) are depicted in terms of RMSE, AAD, CC and ERGAS (Section 3.4). The B5, B6 and B7 correspond to the NIR (0.865 μm band), SWIR1 (1.6 μm band) and SWIR2 (2.2 μm band) channels respectively. The actual and modified-version of various spatiotemporal fusion methods are listed in the 1st column.

Approaches	RMSE			AAD			CC			ERGAS
	B5	B6	B7	B5	B6	B7	B5	B6	B7	
STARFM	0.012	0.013	0.012	0.009	0.009	0.008	0.960	0.972	0.961	0.511
Modified-STARFM	0.012	0.013	0.012	0.009	0.009	0.008	0.958	0.971	0.959	0.524
ESTARFM	0.015	0.018	0.010	0.010	0.012	0.006	0.934	0.937	0.967	0.678
Modified-ESTARFM	0.009	0.010	0.010	0.006	0.007	0.006	0.979	0.983	0.974	0.401

5.3. Results and comparative analysis of coal fire detection on synthetic images

The novel coal fire detection method (NRAFD) was executed on the products derived from various spatiotemporal fusion methods. Also, the quantitative assessments of coal fire maps were carried out by several metrics.

5.3.1. Experimental results after executing NRAFD on STARFM and modified STARFM

Figure 5.4 shows the synthetic coal fire map generated using the STARFM (a) and modified STARFM (b) methods on January 9, 2018. The yellow colour represents the location of the extracted coal fire pixels after executing the NRAFD method.

The NRAFD method was applied to the fused products derived from STARFM and modified STARFM for retrieving synthetic coal fire affected pixels. From the Table (a) and (b) in Figure 5.4, the estimated number of actual coal fire affected pixels (630 Landsat pixels) with the spatial coverage ≈ 0.57 km^2, were retrieved after executing the NRAFD method on actual Landsat-8 image. Using STARFM, the total 649 number of synthetic coal fire pixels were filtered out with a spatial coverage ≈ 0.58 km^2, of which the total 380 number of synthetic pixels with the spatial coverage ≈ 0.34 km^2 hold the locational similarity with the actual coal fire map derived on January 9, 2018. Also, the total number of false positives which appeared in synthetic coal fire map was approximately 0.24 km^2. Moreover, the estimated area of ≈ 0.23 km^2, got undetected in the synthetic coal fire map which was extracted in an actual coal fire map. On the other hand, the estimated overlapping region between the actual coal fires maps with the synthetically predicted

coal fire map derived from modified STARFM, was approximately 0.33 km². However, the false positives which appeared in the products generated using the modified STARFM were slightly higher than the actual STARFM (Overlapping region: 0.27 km² vs 0.24 km²).

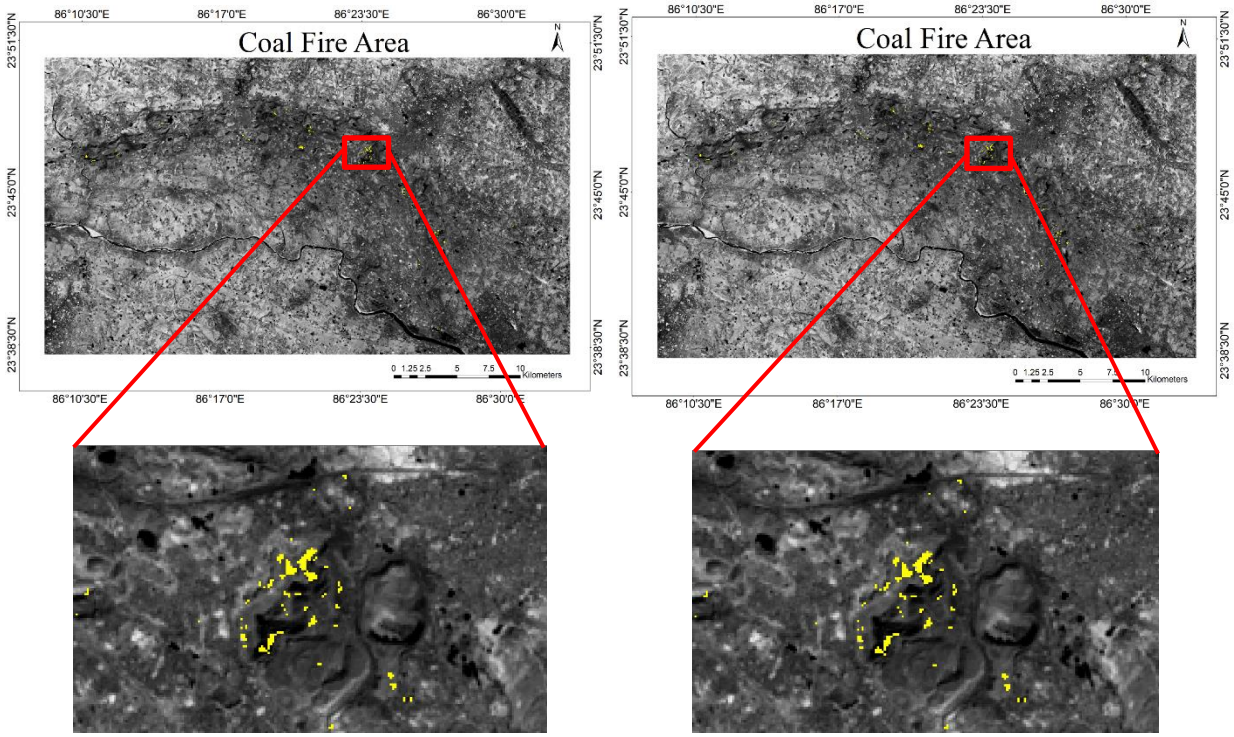

Figure 5.4 The predicted coal fire map derived by incorporating the NRAFD method on synthetic Landsat images (spectral range – band 5, band 6 and band 7 of synthetic Landsat 8 data). (a) Synthetic coal map generated from actual STARFM. (b) Synthetic coal map generated from modified STARFM

5.3.2. Experimental results after executing NRAFD on ESTARFM and modified ESTARFM

Figure 5.5 depicts the synthetic coal fire map generated using the synthetic Landsat images derived from ESTARFM (a) and modified ESTARFM (b) methods on January 9, 2018. The novel NRAFD method was applied for extracting the location of synthetic coal fire pixels. The yellow colour represents the location of the extracted coal fire pixels. It was observed that a significant number of false positives appeared on the coal fire map derived from the actual ESTARFM (encircled cyan in the zoomed view, (a) in Figure 5.5). From Table (c) and (d) in Figure 5.6, the spatial coverage of the actual coal fire affected pixels was approximately 0.57 km².

Using ESTARFM, 1121 number of synthetic coal fire pixels were retrieved with a spatial coverage ≈ 1.00 km², of which the total 416 number of synthetic pixels with the spatial coverage ≈ 0.374 km² overlapped with the actual coal fire map derived on January 9, 2018 ((c) in Figure 5.6). Furthermore, the total of 0.63 km² appeared as false positives which got detected as coal fire. Also, the estimated area of ≈ 0.20 km², remain undetected in the synthetic coal fire map in reference to actual coal fire map. Using the modified ESTARFM, 706 number of synthetic coal fire pixels were retrieved with a spatial coverage ≈ 0.63 km², of which, 418 number of synthetic pixels with the spatial coverage ≈ 0.376 km² overlapped with the actual coal fire map derived on January 9, 2018. Furthermore, the total 0.254 km² appeared falsely which got detected as coal fire in the synthetic coal fire product. However, the estimated area of ≈ 0.20 km², remain undetected in the synthetic coal fire map in reference to actual coal fire map on January 9, 2018.

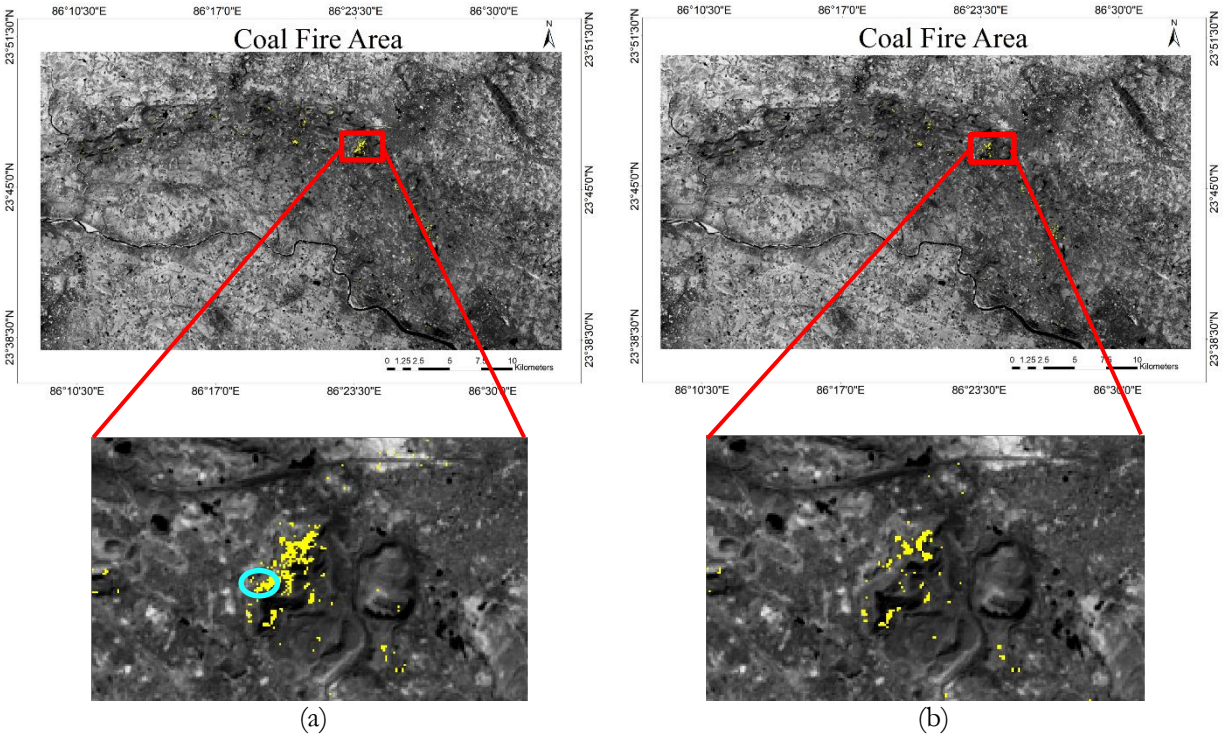

Figure 5.5. The predicted coal fire map derived by incorporating the NRAFD method on synthetic Landsat images (spectral range – band 5, band 6 and band 7 of synthetic Landsat 8 data). (a) Synthetic coal map generated from actual ESTARFM. (b) Synthetic coal map generated from modified ESTARFM

5.3.3. Accuracy assessments of coal fire maps derived from synthetic Landsat images using various spatiotemporal fusion approaches

The coal fire maps generated by executing NRAFD method on the synthetic products derived from various spatiotemporal fusion methods were evaluated by assessment metrics coupled with the confusion matrices. It was observed that the coal fire products generated by modified ESTARFM outperformed all other spatiotemporal fusion methods in terms of assessment metrics. The F_1 score (ranges from 0 to 1, both inclusive) of modified ESTARFM was 0.625 along with the TPR as 0.663. Furthermore, the value of PPV was the highest (0.592 from Table 5.1) for the modified ESTARFM compared to other spatiotemporal fusion methods. Even though the value of TPR for ESTARFM was closer to modified ESTARFM, the value of the PPV was lowest in comparison to other fused products strictly indicating the presence of false alarms with a higher rate. Also, the CFPQI (ranges from 0 to 1), which was established for evaluating the quality of synthetic coal fire product, depicted the highest value (0.626 from Table 5.1) for the coal fire map derived from modified ESTARFM.

In light of the above discussions, it was observed that the performance evaluation of several spatiotemporal fusion methods was comparable with others (Table 5.1). The relative differences between the values of the assessment metrics are within the acceptable limit as per previous studies in reference to the methods of spatiotemporal fusion approaches. In this context, it is noteworthy that there had been no previous literature related to the quantitative assessments of the synthetic coal fire products generate by spatiotemporal fusion methods over the region of Jharia coalfield, India. Although accuracies of the fused images are within the acceptable limit for the spatiotemporal fusion methods (Table 5.1), it doesn't necessarily imply the improvement of the synthetic coal fire products subsequently (Table 5.1).

STARFM Number of Pixels = 960093	Predicted fire pixels NO	Predicted fire pixels: YES	
Actual fire pixels NO	959194	269	959463
Actual fire pixels YES	250	380	630
	959444	649	960093

(a)

Modified STARFM Number of Pixels = 960093	Predicted fire pixels NO	Predicted fire pixels: YES	
Actual fire pixels NO	958859	304	959463
Actual fire pixels YES	256	374	630
	959415	678	960093

(b)

ESTARFM Number of Pixels = 960093	Predicted fire pixels NO	Predicted fire pixels: YES	
Actual fire pixels NO	958758	705	959463
Actual fire pixels YES	214	416	630
	958972	1121	960093

(c)

Modified ESTARFM Number of Pixels = 960093	Predicted fire pixels NO	Predicted fire pixels: YES	
Actual fire pixels NO	959175	288	959463
Actual fire pixels YES	212	418	630
	959387	706	960093

(d)

Figure 5.6. Table (a) depicts the confusion matrix for STARFM generated using the actual and predicted coal fire map on January 9, 2018. Table (b), (c) and (d) depict the confusion matrices derived from similar experimental results for modified STARFM, ESTARFM and modified ESTARFM respectively.

Table 5.1. Quantitative assessment of the quality of the fused products using several metrics derived from the confusion matrices.

Approaches	**F_1 Score**	**MCC**	**TPR**	**PPV**	**CFPQI**
STARFM	0.594	0.594	0.603	0.586	0.594
Modified STARFM	0.571	0.571	0.593	0.551	0.571
ESTARFM	0.474	0.495	0.660	0.371	0.481
Modified ESTARM	0.625	0.627	0.663	0.592	0.626

6. DISCUSSION

This chapter illustrates the scientific investigations of the obtained results (Chapter 5), aligning with the specific objectives associated with the coal fire detection methods and spatiotemporal fusion approaches.

The AFD method as stated in Chapter 2, was used to detect and delineate the coal fire-affected regions in Jharia Coalfield, India. As per visual inspection, it was found that the AFD method was underestimating for some of the regions which were also affected by a surface coal fire. The underestimation was caused by the effect of contextual analysis concerning the background statistics. Also, this underestimation can be attributed to the higher fixed threshold values between the ratios of reflectance in the intermediate test sequences for the fire responsive channels. In this context, the AFD method was unable to identify the coal fire pixels with lower intensities (pixels corresponding to yellowish red and red colour). Therefore, a novel coal fire detection method (NRAFD) was established based on the channel specific normalisation. The advantage of the normalisation was that, by setting appropriate thresholds (Eq. (3.5)), the slope effects neglected the background statistics based on the spectral pattern which was strictly increasing from band 5 to band 7. Hence, NRAFD effectively extracted the previously undetected coal fire pixels. As a result, this novel method was successfully able to resolve the underestimation caused by the existing AFD method.

In this study, several weight-function based spatiotemporal fusion methods were incorporated to generate synthetic Landsat like images with a view to producing the high-resolution and high-frequency synthetic coal fire products. The comparative analysis in Chapter 5 showed that the modified ESTARFM produced more accurate results in comparison to the other spatiotemporal fusion techniques as discussed in Chapter 3. These improvements were caused by the channel-specific retrieval of similar pixels from a moving window. Here, the window wise correlation and conversion coefficients were used to generate a weight function for predicting the surface reflectance of the central pixel. Due to that, the artifacts appearing on the synthetic images were significantly removed in modified ESTARFM.

As part of the third objective, the goal was to detect and delineate the coal fire affected pixels from the synthetic Landsat images derived from the spatiotemporal fusion methods explored in this study. It was observed that the accuracies achieved from the synthetic coal fire pixels could not be compared because there were no relevant studies in this framework. Also, the investigations showed that the higher accuracies in the spatiotemporal fusion methods (Chapter 3) didn't necessarily imply the higher accuracies in the coal fire products derived from these synthetic images. In essence, the surface coal fire cannot be treated as a large patch (consisting of homogeneous pixels). Therefore, the probability of overlap between the pixels in the actual Landsat image and synthetic image pixels is relatively lower for the synthetic coal fire maps generated from the spatiotemporal fusion methods.

In light of the above discussions, the novel coal fire detection method (NRAFD) which was established in this study, didn't explicitly address the retrieval of sub-surface coal fire pixels. On the other hand, this study has explored the weight-function based spatiotemporal fusion framework in generating the synthetic Landsat images. However, the accuracy of the fused images may further be improved in other spatiotemporal fusion frameworks (e.g., Bayesian method, learning based method). Moreover, the systematic visual inspections were carried out due to the unavailability of the reference maps for checking the fidelity of the NRAFD method in retrieving the coal fire affected pixels. Also, the sensitivity of the accuracies of the fused images with the accuracy of the synthetic products was not explored.

7. CONCLUSIONS AND RECOMMENDATIONS

The core objective of this research is to formulate a methodology for generating a high resolution and high-frequency coal fire product by harmonizing the high spatial resolution Landsat 8 OLI data with the high temporal resolution VIIRS data within the spatiotemporal fusion framework. The chosen study area was Jharia coalfield, India. To achieve the overall objective, we developed distinct methodologies such as a novel reflectance-based active fire detection method, modified spatiotemporal fusion approaches, generation of synthetic Landsat like images and associated synthetic coal fire products. The performance of these methods was evaluated quantitatively and qualitatively. Section 7.1 elucidates the necessary conclusions which were drawn from the results aligning with the specific objectives.

7.1. Response to the research objectives

In response to the research questions linked with the specific objectives, overall conclusions were drawn for the specific objectives.

7.1.1. Response to objective 1

The goal of the first objective was to review and study the active fire detection methods for detecting and delineating the surface fire-affected areas. A contextual review of different coal fire detection methods was reported in Section 2.2. In this study, the channel-specific reflectance-based active fire detection method (AFD) was incorporated to retrieve the coal fire affected pixels from Landsat 8 OLI data. In was observed that the AFD method was successful in delineating a significant number of the surface coal fire affected pixels (appeared pure yellow and yellowish red in FCC composite of band 5, band 6, and band 7 of Landsat 8 OLI). However, the AFD method was unable to detect a significant number of fire-affected pixels which were also appearing as red and yellowish red as reported in Section 5.1. To resolve the underestimation as mentioned earlier, a normalised reflectance-based active fire detection (NRAFD) method was developed using the concept of channel-specific normalisation as presented in Section 3.2. The method was found to be successful in retrieving an additional number of fire-affected pixels which was undetected in AFD method. The fidelity of this method was tested on multiple Landsat-8 OLI (from January 2014 to January 2018) scenes over the chosen study area. The performance of the novel NRAFD method concludes that the method was successful in overcoming the underestimation caused by original AFD method. Therefore, this method was chosen as a reference in retrieving the coal fire pixels from the synthetic images generated from the spatiotemporal fusion approaches.

7.1.2. Response to objective 2

The second objective was dedicated to exploring the spatiotemporal fusion methods within the domain of miscellaneous fusion framework as reported in Section 2.3. In this research, the weight-function based fusion framework was utilized to harmonize the high spatial resolution Landsat 8 OLI data with the high temporal resolution VIIRS data (spectral domain: band 5 – I2 (NIR); band 6 – I3 (SWIR1); band 7 – M11 (SWIR2); corresponding spectral channel of Landsat and VIIRS sensor respectively as described in Table 4.3). Consequently, the STARFM and ESTARFM methods were incorporated to generate the synthetic Landsat like images. The qualitative and quantitative assessments of the predicted images were carried out about the actual images based on several metrics (RMSE, AAD, CC, and ERGAS) as reported in Section 5.2. It was observed that a significant number of artifacts appeared in the synthetic FCC composite generated from ESTARFM method (encircled yellow in the zoomed window of (b) in Figure 5.3). Therefore, the modified STARFM and the modified ESTARFM were established with the view to improving the overall accuracy (Section 3.3). Also, a comparative analysis between these methods was

reported in Section 5.2. Interestingly, the quantitative assessments of the fused images concluded that the modified ESTARFM outperformed all other fusion methods in terms of generating synthetic images with higher spectral similarity as illustrated in Section 5.2.3.

7.1.3. Response to objective 3

The third objective was dedicated to detecting coal fire pixels from the synthetic images generated from spatiotemporal fusion methods, thereby assessing the quality of the synthetic coal fire products in reference to actual coal fire products. The novel NRAFD method was applied to the synthetic images for retrieving the coal fire affected pixels. Furthermore, the qualitative and quantitative assessments of these products were carried out based on several metrics (F_1 Score, MCC, TPR, PPV). Also, a new product quality index (CFPQI) was designed to address to the quality of the synthetic products as reported in Section 3.5.5. The assessments of the synthetic coal fire products concluded that a synthetic product derived from modified ESTARFM method outperformed all other spatiotemporal fusion methods (Section 5.3.3).

7.2. Applicability of the research

This research was carried out with a view to establishing a framework for systematic monitoring of the surface coal fires of Jharia coalfield, India. Moreover, the directional propagation of coal fire within a period can be monitored and associated precautionary measures can be taken into considerations.

7.3. Recommendations

1. The novel coal fire detection method (NRAFD) could be tested for the other mining regions which are also affected by coal fire such as China, USA and Australia. Also, the reflectance-based coal fire detection method could also be further improved by incorporating different environmental parameters such as the direction of the wind, topographic variations and so on.

2. To generate a high-frequency coal fire product, a fusion-based neural network can be designed to predict the location of coal fire more accurately.

3. The uncertainty assessment of the synthetic coal fire products can be carried out in future studies, and the quality of the fused product can be further improved.

LIST OF REFERENCES

Anderson, M. C., Hain, C., Wardlow, B., Pimstein, A., Mecikalski, J. R., & Kustas, W. P. (2011). Evaluation of drought indices based on Thermal remote sensing of evapotranspiration over the continental United States. *Journal of Climate*, *24*(8), 2025–2044. https://doi.org/10.1175/2010JCLI3812.1

Andres, R. J., & Rose, W. I. (1995). Description of thermal anomalies on 2 active guatemalan volcanos using landsat thematic mapper imagery. *Photogrammetric Engineering and Remote Sensing*, *61*(6), 775–782. Retrieved from https://www.asprs.org/wp-content/uploads/pers/1995journal/jun/1995_jun_775-782.pdf

Bennett, M. M., & Smith, L. C. (2017). Advances in using multitemporal night-time lights satellite imagery to detect, estimate, and monitor socioeconomic dynamics. *Remote Sensing of Environment*, *192*, 176–197. https://doi.org/10.1016/j.rse.2017.01.005

Bhattacharya, A., & Reddy, C. S. (1994). Underground and surface coal mine fire detection in India's Jharia coal field using airborne thermal infrared data. *Asian Pacific Remote Sensing Journal 7*, 59–73.

Bhattacharya, A., Reddy, C. S., & Mukherjee, T. (1991). Multitier remote sensing data analysis for coal fire mapping in Jharia coalfield of Bihar, India. *Asian Conference on Remote Sensing*, 221–226.

Boya, L. J. (2004). *The Thermal Radiation Formula of Planck (2004)*.

Buettner, K. J. K., & Kern, C. D. (1965). The determination of infrared emissivities of terrestrial surfaces. *Journal of Geophysical Research*, *70*(6), 1329–1337. https://doi.org/10.1029/JZ070i006p01329

Chatterjee, R. S. (2006). Coal fire mapping from satellite thermal IR data - A case example in Jharia Coalfield, Jharkhand, India. *ISPRS Journal of Photogrammetry and Remote Sensing*, *60*(2), 113–128. https://doi.org/10.1016/j.isprsjprs.2005.12.002

Cracknell, A. P., & Mansor, S. B. (1993). Detection of sub-surface coal fires using Landsat Thematic Mapper data. *International Archives of Photogrammetry and Remote Sensing*, *29*(5), 750.

Dong, J., Zhuang, D., Huang, Y., & Fu, J. (2009). Advances in multi-sensor data fusion: Algorithms and applications. *Sensors*, *9*(10), 7771–7784. https://doi.org/10.3390/s91007771

Dozier, J. (1981). A method for satellite identification of surface temperature fields of subpixel resolution. *Remote Sensing of Environment*, *11*, 221–229. https://doi.org/10.1016/0034-4257(81)90021-3

EARTHDATA. (2019). VNP09GA - VIIRS/NPP Surface Reflectance Daily L2G Global 1km and 500m SIN Grid. Retrieved February 2, 2019, from https://ladsweb.modaps.eosdis.nasa.gov/missions-and-measurements/products/land-surface-reflectance/VNP09GA/

Ehlers, M., Klonus, S., Åstrand, P. J., & Rosso, P. (2010). Multi-sensor image fusion for pansharpening in remote sensing. *Internation Journal of Image and Data Fusion*, *1*(1), 25–45. https://doi.org/10.1080/19479830903561985

Elvidge, C., Zhizhin, M., Hsu, F.-C., & Baugh, K. (2013). VIIRS Nightfire: Satellite Pyrometry at Night. *Remote Sensing*, *5*(9), 4423–4449. https://doi.org/10.3390/rs5094423

Feynman, R. P., Leighton, R. B., & Sands, M. (1989). *The Feynman Lectures on Physics*. Newyork: Addison Wesley.

Francis, P. W., & De Silva, S. L. (1989). Application of the Landsat Thematic Mapper to the identification of potentially active volcanoes in the central Andes. *Remote Sensing of Environment*, *28*, 245–255. https://doi.org/10.1016/0034-4257(89)90117-X

Fu, D., Chen, B., Wang, J., Zhu, X., & Hilker, T. (2013). An improved image fusion approach based on enhanced spatial and temporal the adaptive reflectance fusion model. *Remote Sensing*, *5*(12), 6346–6360. https://doi.org/10.3390/rs5126346

Gangopadhyaya, P. K. (2003). *Coalfire detection and monitoring in Wuda, North China: A multi-spectral and multi-sensor TIR approach (MSc thesis)*. International Institute for Geo-information Science and Earth Observation Enschede, The Netherlands. Retrieved from https://webapps.itc.utwente.nl/librarywww/papers_2003/msc/ereg/prasun.pdf

Gao, F., Masek, J., Schwaller, M., & Hall, F. (2006). On the blending of the Landsat and MODIS surface reflectance: Predicting daily Landsat surface reflectance. *IEEE Transactions on Geoscience and Remote Sensing*, *44*(8), 2207–2218. https://doi.org/10.1109/TGRS.2006.872081

Gevaert, C. M., & García-Haro, F. J. (2015). A comparison of STARFM and an unmixing-based algorithm for Landsat and MODIS data fusion. *Remote Sensing of Environment*, *156*, 34–44. https://doi.org/10.1016/j.rse.2014.09.012

Giglio, L., Csiszar, I., Restás, Á., Morisette, J. T., Schroeder, W., Morton, D., & Justice, C. O. (2008).

Active fire detection and characterization with the advanced spaceborne thermal emission and reflection radiometer (ASTER). *Remote Sensing of Environment*, *112*(6), 3055–3063. https://doi.org/10.1016/j.rse.2008.03.003

Goshtasby, A. A., & Nikolov, S. (2007). Image fusion: Advances in the state of the art. *Information Fusion*, *8*, 114–118. https://doi.org/10.1016/j.inffus.2006.04.001

Guha, A., Kumar, K. V., & Kamaraju, M. V. . . (2008). A satellite-based study of coal fires and open-cast mining activity in Raniganj coalfield, West Bengal. *Current Science*, *95*(11), 1603–1607. https://doi.org/10.1016/j.minpro.2005.08.002

Gupta, M., Mohanty, K. K., Kumar, D., & Banerjee, R. (2014). Monitoring surface elevation changes in Jharia coalfield, India using synthetic aperture radar interferometry. *Environmental Earth Sciences*, *71*(6), 2875–2883. https://doi.org/10.1007/s12665-013-2664-9

Hazaymeh, K., & Hassan, Q. K. (2015). Spatiotemporal image-fusion model for enhancing the temporal resolution of Landsat-8 surface reflectance images using MODIS images. *Journal of Applied Remote Sensing*, *9*(1), 096095. https://doi.org/10.1117/1.JRS.9.096095

Huang, B., & Song, H. (2012). Spatiotemporal reflectance fusion via sparse representation. *IEEE Transactions on Geoscience and Remote Sensing*, *50*(10 PART1), 3707–3716. https://doi.org/10.1109/TGRS.2012.2186638

Huang, B., Zhang, H., Song, H., Wang, J., & Song, C. (2013). Unified fusion of remote-sensing imagery: Generating simultaneously high-resolution synthetic spatial–temporal–spectral earth observations. *Remote Sensing Letters*, *4*(6), 561–569. https://doi.org/10.1080/2150704X.2013.769283

Huo, H., Jiang, X., Song, X., Li, Z. L., Ni, Z., & Gao, C. (2014). Detection of coal fire dynamics and propagation direction from multi-temporal nighttime landsat SWIR and TIR data: A case study on the Rujigou Coalfield, Northwest (NW) China. *Remote Sensing*, *6*(2), 1234–1259. https://doi.org/10.3390/rs6021234

Huo, H., Ni, Z., Gao, C., Zhao, E., Zhang, Y., Lian, Y., … Cui, T. (2015). A study of coal fire propagation with remotely sensed thermal infrared data. *Remote Sensing*, *7*(3), 3088–3113. https://doi.org/10.3390/rs70303088

Irons, J. R., Dwyer, J. L., & Barsi, J. A. (2012). The next Landsat satellite: The Landsat Data Continuity Mission. *Remote Sensing of Environment*, *122*, 11–21. https://doi.org/10.1016/j.rse.2011.08.026

Jin, M., & Liang, S. (2006). An improved land surface emissivity parameter for land surface models using global remote sensing observations. *Journal of Climate*, *19*(12), 2867–2881. https://doi.org/10.1175/JCLI3720.1

Justice, C. O., Román, M. O., Csiszar, I., Vermote, E. F., Wolfe, R. E., Hook, S. J., … Masuoka, E. J. (2013). Land and cryosphere products from Suomi NPP VIIRS: Overview and status. *Journal of Geophysical Research*, *118*, 9753–9765. https://doi.org/10.1002/jgrd.50771

Kanniah, K. D., Kaskaoutis, D. G., San Lim, H., Latif, M. T., Kamarul Zaman, N. A. F., & Liew, J. (2016). Overview of atmospheric aerosol studies in Malaysia: Known and unknown. *Atmospheric Research*, *182*, 302–318. https://doi.org/10.1016/j.atmosres.2016.08.002

Kato, S., Kouyama, T., Nakamura, R., Matsunaga, T., & Fukuhara, T. (2018). Simultaneous retrieval of temperature and area according to sub-pixel hotspots from nighttime Landsat 8 OLI data. *Remote Sensing of Environment*, *204*(May 2016), 276–286. https://doi.org/10.1016/j.rse.2017.10.025

Kuenzer, C. (2004). *Spatial and statistical analysis of thermal satellite imagery for extraction of coal fire related anolmalies (Doctoral dissertation)*. Vienna University of Technology. Retrieved from https://publik.tuwien.ac.at/files/PubDat_119584.pdf

Kuenzer, C., & Dech, S. (2013). *Thermal Infrared Remote Sensing: Remote Sensing and Digital Image Processing 17*. Springer Verlag. Retrieved from https://www.dawsonera.com:443/abstract/9789400766396

Kuenzer, C., Hecker, C., Zhang, J., Wessling, S., & Wagner, W. (2008). The potential of multidiurnal MODIS thermal band data for coal fire detection. *International Journal of Remote Sensing*, *29*(3), 923–944. https://doi.org/10.1080/01431160701352147

Kuenzer, C., Zhang, J., Li, J., Voigt, S., Mehl, H., & Wagner, W. (2007). Detecting unknown coal fires: Synergy of automated coal fire risk area delineation and improved thermal anomaly extraction. *International Journal of Remote Sensing*, *28*(20), 4561–4585. https://doi.org/10.1080/01431160701250432

Kuenzer, C., Zhang, J., Tetzlaff, A., van Dijk, P., Voigt, S., Mehl, H., & Wagner, W. (2007). Uncontrolled coal fires and their environmental impacts: Investigating two arid mining regions in north-central China. *Applied Geography*, *27*(1), 42–62. https://doi.org/10.1016/j.apgeog.2006.09.007

Li, A., Bo, Y., Zhu, Y., Guo, P., Bi, J., & He, Y. (2013). Blending multi-resolution satellite sea surface

temperature (SST) products using Bayesian maximum entropy method. *Remote Sensing of Environment*, *135*, 52–63. https://doi.org/10.1016/j.rse.2013.03.021

Liu, H., & Weng, Q. (2012). Enhancing temporal resolution of satellite imagery for public health studies: A case study of West Nile Virus outbreak in Los Angeles in 2007. *Remote Sensing of Environment*, *117*, 57–71. https://doi.org/10.1016/j.rse.2011.06.023

Mansor, S. B., Cracknell, A. P., Shilin, B. V., & Gornyi, V. I. (1994). Monitoring of underground coal fires using thermal infrared data. *International Journal of Remote Sensing*, *15*(8), 1675–1685. https://doi.org/10.1080/01431169408954199

Matthews, B. W. (1975). Comparison of the predicted and observed secondary structure of T4 Phage Lysozyme. *Biochimica et Biophysica Acta (BBA) - Protein Structure*, *405*, 442–451. https://doi.org/10.1016/0005-2795(75)90109-9

Meng, J., Du, X., & Wu, B. (2013). Generation of high spatial and temporal resolution NDVI and its application in crop biomass estimation. *International Journal of Digital Earth*, *6*(3), 203–218. https://doi.org/10.1080/17538947.2011.623189

Meng, X., Shen, H., Zhang, L., Yuan, Q., & Li, H. (2015). A unified framework for spatio-temporal-spectral fusion. *IEEE International Geoscience and Remote Sensing Symposium (IGARSS)*, (1), 2584–2587.

Mishra, R. K., Bahuguna, P. P., & Singh, V. K. (2011). Detection of coal mine fire in Jharia Coal Field using Landsat-7 ETM+ data. *International Journal of Coal Geology*, *86*(1), 73–78. https://doi.org/10.1016/j.coal.2010.12.010

Mukherjee, J., Mukherjee, J., & Chakravarty, D. (2018). Detection of coal seam fires in summer seasons from landsat 8 OLI/TIRS in Dhanbad. *Communications in Computer and Information Science* (Vol. 841, pp. 529–539). Springer Singapore. https://doi.org/10.1007/978-981-13-0020-2_46

Mukherjee, T. K., Bandyopadhyay, T. K., & Pande, S. K. (1991). Detection and delineation of depth of subsurface coal-mine fires based on an airborne multispectral scanner survey in a part of the Jhari Coalfield, India. *Photogrammetric Engineering and Remote Sensing*, *57*(9), 1203–1207. Retrieved from https://trid.trb.org/view/359980

Niu, Z. (2012). Use of MODIS and Landsat time series data to generate high-resolution temporal synthetic Landsat data using a spatial and temporal reflectance fusion model. *Journal of Applied Remote Sensing*, *6*(1), 063507. https://doi.org/10.1117/1.JRS.6.063507

Oliva, P., & Schroeder, W. (2015). Assessment of VIIRS 375m active fire detection product for direct burned area mapping. *Remote Sensing of Environment*, *160*, 144–155. https://doi.org/10.1016/j.rse.2015.01.010

Oppenheimer, C., Rothery, D. A., Fieri, D. C., Abrams, M. J., & Carrere, V. (1993). Analysis of airborne visible/infrared imaging spectrometer (Aviris) data of volcanic hot spots. *International Journal of Remote Sensing*, *14*(16), 2919–2934. https://doi.org/10.1080/01431169308904411

Pohl, C., & Van Genderen, J. L. (1998). Multisensor image fusion in remote sensing: Concepts, methods and applications. *International Journal of Remote Sensing*, *19*(5), 823–854. https://doi.org/10.1080/014311698215748

Prakash, A., & Gupta, R. P. (1998). Land-use mapping and change detection in a coal mining area - A case study in the Jharia coalfield, India. *International Journal of Remote Sensing*, *19*(3), 391–410. https://doi.org/10.1080/014311698216053

Prakash, A., Gupta, R. P., & Saraf, A. K. (1997). A Landsat TM based comparative study of surface and subsurface fires in the Jharia coalfield, India. *International Journal of Remote Sensing*, *18*(11), 2463–2469. https://doi.org/10.1080/014311697217738

Prakash, A., Saraf, A. K., & Gupta, R. P. (1995). Surface thermal anomalies associated with underground fires in Jharia coal mines, India. *International Journal of Remote Sensing*, *16*(12), 2105–2109. https://doi.org/10.1080/01431169508954544

Raju, A., Gupta, R. P., & Prakash, A. (2013). Delineation of coalfield surface fires by thresholding Landsat TM-7 day-time image data. *Geocarto International*, *28*(4), 343–363. https://doi.org/10.1080/10106049.2012.710651

Rao, Y., Zhu, X., Chen, J., & Wang, J. (2015). An improved method for producing high spatial-resolution NDVI time series datasets with multi-temporal MODIS NDVI data and Landsat TM/ETM+ images. *Remote Sensing*, *7*(6), 7865–7891. https://doi.org/10.3390/rs70607865

Reddy, C. S. S., Srivastav, S. K., & Bhattacharya, A. (1993). Application of thematic mapper short wavelength infrared data for the detection and monitoring of high temperature related geoenvironmental features. *International Journal of Remote Sensing*, *14*(17), 3125–3132. https://doi.org/10.1080/01431169308904425

Rothery, D. A., Francis, P. W., & Wood, C. A. (1988). Volcano monitoring using short wavelength infrared data from satellites. *Journal of Geophysical Research*, *93*(B7), 7993–8008. https://doi.org/10.1029/JB093iB07p07993

Roy, D. P., Ju, J., Lewis, P., Schaaf, C., Gao, F., Hansen, M., & Lindquist, E. (2008). Multi-temporal MODIS–Landsat data fusion for relative radiometric normalization, gap filling, and prediction of Landsat data. *Remote Sensing of Environment*, *112*(6), 3112–3130. https://doi.org/10.1016/j.rse.2008.03.009

Roy, D. P., Wulder, M. A., Loveland, T. R., C.E., W., Allen, R. G., Anderson, M. C., … Zhu, Z. (2014). Landsat-8: Science and product vision for terrestrial global change research. *Remote Sensing of Environment*, *145*, 154–172. https://doi.org/10.1016/j.rse.2014.02.001

Roy, P., Guha, A., & Vinod Kumar, K. (2015). An approach of surface coal fire detection from ASTER and Landsat-8 thermal data: Jharia coal field, India. *International Journal of Applied Earth Observation and Geoinformation*, *39*, 120–127. https://doi.org/10.1016/j.jag.2015.03.009

Saraf, A. K., Prakash, A., Sengupta, S., & Gupta, R. P. (1995). Landsat-TM data for estimating ground temperature and depth of subsurface coal fire in the Jharia coalfield, India. *International Journal of Remote Sensing*, *16*(12), 2111–2124. https://doi.org/10.1080/01431169508954545

Schroeder, W., Oliva, P., Giglio, L., & Csiszar, I. A. (2014). The New VIIRS 375m active fire detection data product: Algorithm description and initial assessment. *Remote Sensing of Environment*, *143*, 85–96. https://doi.org/10.1016/j.rse.2013.12.008

Schroeder, W., Oliva, P., Giglio, L., Quayle, B., Lorenz, E., & Morelli, F. (2016). Active fire detection using Landsat-8/OLI data. *Remote Sensing of Environment*, *185*, 210–220. https://doi.org/10.1016/j.rse.2015.08.032

Schroeder, W., Prins, E., Giglio, L., Csiszar, I., Schmidt, C., Morisette, J., & Morton, D. (2008). Validation of GOES and MODIS active fire detection products using ASTER and ETM+ data. *Remote Sensing of Environment*, *112*(5), 2711–2726. https://doi.org/10.1016/j.rse.2008.01.005

Shen, H., Meng, X., & Zhang, L. (2016). An integrated framework for the spatio-temporal-spectral fusion of remote sensing images. *IEEE Transactions on Geoscience and Remote Sensing*, *54*(12), 7135–7148. https://doi.org/10.1109/TGRS.2016.2596290

Song, H., & Huang, B. (2013). Spatiotemporal satellite image fusion through one-pair image learning. *IEEE Transactions on Geoscience and Remote Sensing*, *51*(4), 1883–1896. https://doi.org/10.1109/TGRS.2012.2213095

Syed, T. H., Riyas, M. J., & Kuenzer, C. (2018). Remote sensing of coal fires in India: A review. *Earth-Science Reviews*, *187*, 338–355. https://doi.org/10.1016/j.earscirev.2018.10.009

Taaheri, A. (2018). HEG - HDF-EOS to GeoTIFF Conversion Tool. Retrieved February 2, 2019, from https://newsroom.gsfc.nasa.gov/sdptoolkit/HEG/HEGContact.html

U.S. Geological Survey. (2018). Landsat Surface Reflectance Level-2 Science Products. Retrieved November 14, 2018, from https://landsat.usgs.gov/landsat-surface-reflectance-data-products

Vadrevu, K., & Lasko, K. (2018). Intercomparison of MODIS AQUA and VIIRS I-Band fires and emissions in an agricultural landscape — Implications for air pollution research. *Remote Sensing*, *10*(7). https://doi.org/10.3390/rs10070978

Van De Griend, A. A., & Owe, M. (1993). On the relationship between thermal emissivity and the normalized difference vegetation index for natural surfaces. *International Journal of Remote Sensing*, *14*(6), 1119–1131. https://doi.org/10.1080/01431169308904400

Van Genderen, J. L., Cassells, C.J.S., Z. X. (1996). The synergisitic use of remotely sensed data for the detection of underground coal fires. *International Archives of Photogrammetry and Remote Sensing*, *XXXI*(B7), 722–727.

Weng, Q., Fu, P., & Gao, F. (2014). Generating daily land surface temperature at Landsat resolution by fusing Landsat and MODIS data. *Remote Sensing of Environment*, *145*, 55–67. https://doi.org/10.1016/j.rse.2014.02.003

Wu, P., Shen, H., Ai, T., & Liu, Y. (2013). Land-surface temperature retrieval at high spatial and temporal resolutions based on multi-sensor fusion. *International Journal of Digital Earth*, *6*, 113–133. https://doi.org/10.1080/17538947.2013.783131

Xue, J., Leung, Y., & Fung, T. (2017). A Bayesian data fusion approach to spatio-temporal fusion of remotely sensed images. *Remote Sensing*, *9*(12), 1310. https://doi.org/10.3390/rs9121310

Zhang, J. (2010). Multi-source remote sensing data fusion: Status and trends. *Internation Journal of Image and Data Fusion*, *1*(1), 5–24. https://doi.org/10.1080/19479830903561035

Zhang, W., Li, A., Jin, H., Bian, J., Zhang, Z., Lei, G., … Huang, C. (2013). An enhanced spatial and

temporal data fusion model for fusing Landsat and MODIS surface reflectance to generate high temporal Landsat-like data. *Remote Sensing*, *5*(10), 5346–5368. https://doi.org/10.3390/rs5105346

Zhang, Y. (2008). Methods for image fusion quality assessment - a review, comparison and analysis. *The International Archives of the Photogrammetry, Remote Sensing and Spatial Information Sciences*, *XXXVII*(B7), 1101–1109.

Zhou, L., Zhang, D., Wang, J., Huang, Z., & Pan, D. (2013). Mapping land subsidence related to underground coal fires in the wuda coalfield (Northern China) using a small stack of ALOS PALSAR differential interferograms. *Remote Sensing*, *5*(3), 1152–1176. https://doi.org/10.3390/rs5031152

Zhu, X., Cai, F., Tian, J., & Williams, T. K. A. (2018). Spatiotemporal fusion of multisource remote sensing data: Literature survey, taxonomy, principles, applications, and future directions. *Remote Sensing*, *10*(4). https://doi.org/10.3390/rs10040527

Zhu, X., Chen, J., Gao, F., Chen, X., & Masek, J. G. (2010). An enhanced spatial and temporal adaptive reflectance fusion model for complex heterogeneous regions. *Remote Sensing of Environment*, *114*(11), 2610–2623. https://doi.org/10.1016/j.rse.2010.05.032

Zhu, X., Helmer, E. H., Gao, F., Liu, D., Chen, J., & Lefsky, M. A. (2016). A flexible spatiotemporal method for fusing satellite images with different resolutions. *Remote Sensing of Environment*, *172*, 165–177. https://doi.org/10.1016/j.rse.2015.11.016

Zhukov, B., Oertel, D., Lanzl, F., & Reinhäckel, G. (1999). Unmixing-based multisensor multiresolution image fusion. *IEEE Transactions on Geoscience and Remote Sensing*, *37*(3 I), 1212–1226. https://doi.org/10.1109/36.763276

Zurita-Milla, R., Kaiser, G., Clevers, J. G. P. W., Schneider, W., & Schaepman, M. E. (2009). Downscaling time series of MERIS full resolution data to monitor vegetation seasonal dynamics. *Remote Sensing of Environment*, *113*(9), 1874–1885. https://doi.org/10.1016/j.rse.2009.04.011

APPENDIX-A

The Landsat 8 OLI scenes which were used as inputs for the novel reflectance-based active fire detection (NRAFD) method.

Table A-1: The table shows the Landsat 8 OLI scene ID with the corresponding acquisition date.

Sequence No	Landsat 8 OLI scene ID	Acquisition Date
1	"LC81400432014030LGN01"	2014-01-30
2	"LC81400432014078LGN01"	2014-03-19
3	"LC81400432014094LGN01"	2014-04-04
4	"LC81400432014270LGN01"	2014-09-27
5	"LC81400432015017LGN01"	2015-01-17
6	"LC81400432015033LGN02"	2015-02-02
7	"LC81400432015081LGN01"	2015-03-22
8	"LC81400432015145LGN01"	2015-05-25
9	"LC81400432015353LGN01"	2015-12-19
10	"LC81400432016004LGN02"	2016-01-04
12	"LC81400432016036LGN01"	2016-02-05
13	"LC81400432016084LGN01"	2016-03-24
14	"LC81400432016116LGN01"	2016-04-25
15	"LC81400432016164LGN01"	2016-06-12
16	"LC81400432016308LGN01"	2016-11-03
17	"LC81400432016356LGN02"	2016-12-21
18	"LC81400432017022LGN01"	2017-01-22
19	"LC81400432017054LGN00"	2017-02-23
20	"LC81400432017086LGN00"	2017-03-27
21	"LC81400432017118LGN00"	2017-04-28
22	"LC81400432017134LGN00"	2017-05-14
23	"LC81400432017326LGN00"	2017-11-22
24	"LC81400432017358LGN00"	2017-12-24

The coal fire maps which were generated after executing the NRAFD method over the Landsat scenes as depicted in Table A-1.

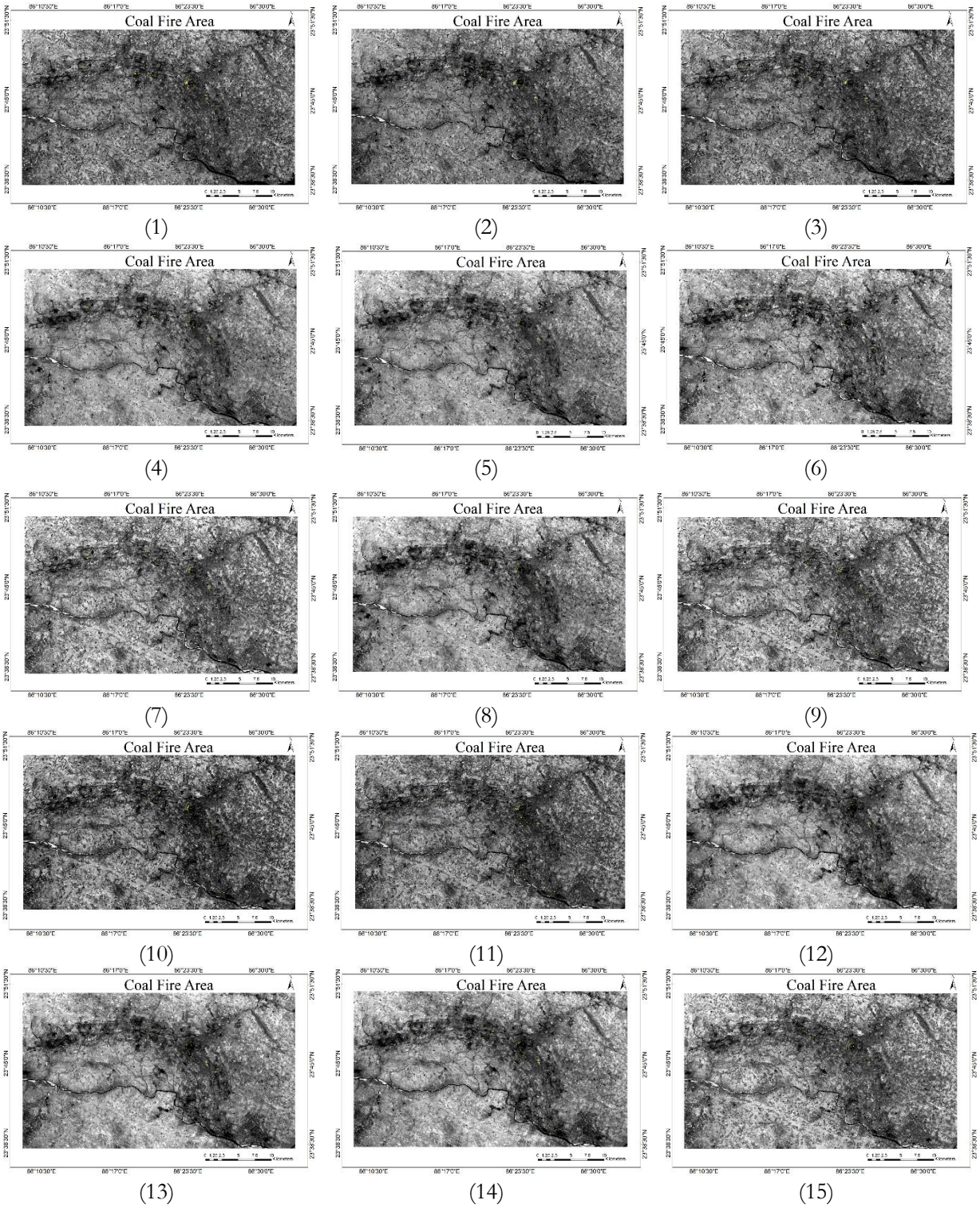

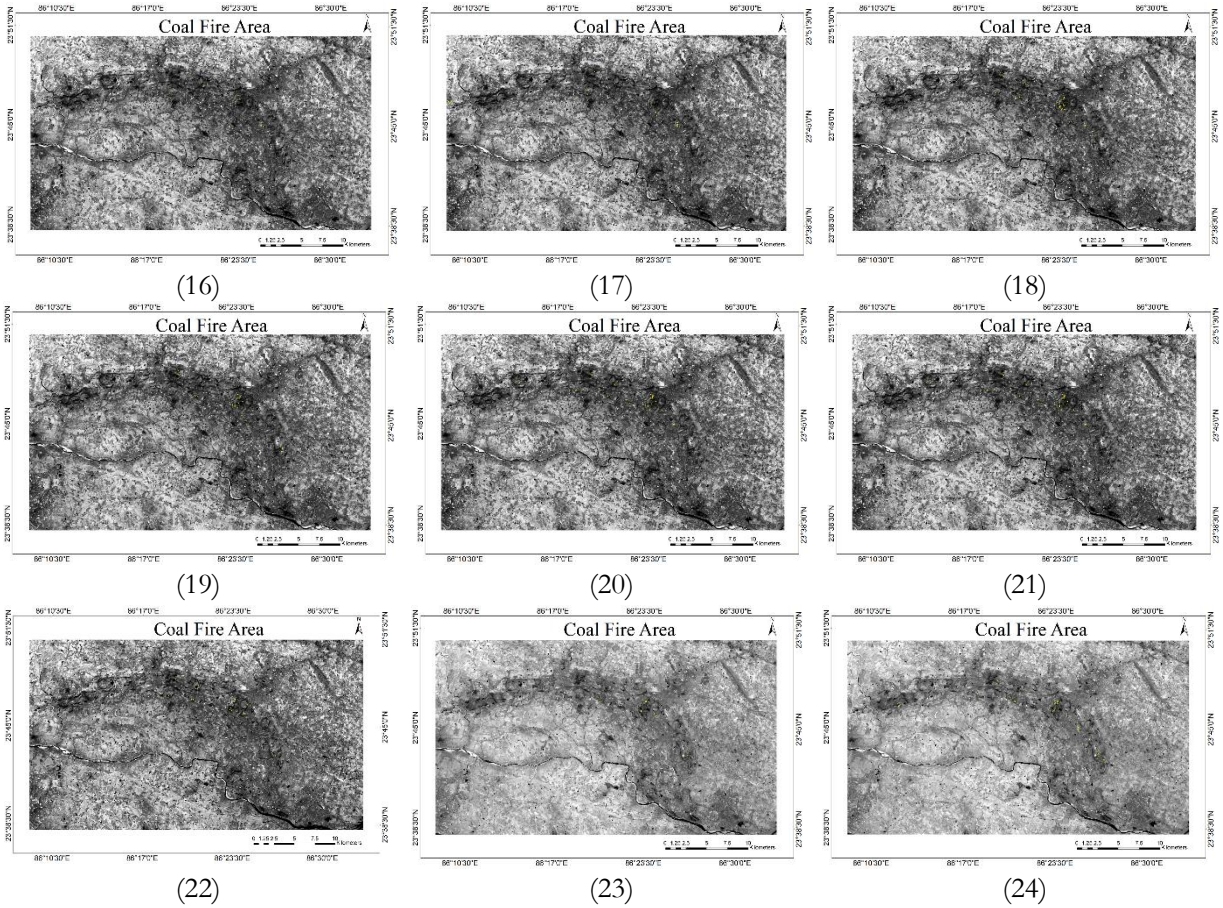

Figure A-1. The coal fire maps generated using the Landsat 8 OLI scenes depicted in Table A-1. The number in Table A-1 (Sequence No) corresponds to similar number in this figure.